SATELLITE-BASED REMOTE SENSING OF CIRRUS CLOUDS: HYPERSPECTRAL RADIATIVE TRANSFER MODELING, ANALYSIS OF UNCERTAINTIES IN IN-SITU CLOUD EXTINCTION MEASUREMENTS AND INTERCOMPARISON OF CIRRUS RETRIEVALS FROM A-TRAIN INSTRUMENTS

A Dissertation

by

ZHIBO ZHANG

Submitted to the Office of Graduate Studies of
Texas A&M University
in partial fulfillment of the requirements for the degree of

DOCTOR OF PHILOSOPHY

August 2008

Major Subject: Atmospheric Sciences

SATELLITE-BASED REMOTE SENSING OF CIRRUS CLOUDS: HYPERSPECTRAL RADIATIVE TRANSFER MODELING, ANALYSIS OF UNCERTAINTIES IN IN-SITU CLOUD EXTINCTION MEASUREMENTS AND INTERCOMPARISON OF CIRRUS RETRIEVALS FROM A-TRAIN INSTRUMENTS

A Dissertation

by

ZHIBO ZHANG

Submitted to the Office of Graduate Studies of
Texas A&M University
in partial fulfillment of the requirements for the degree of

DOCTOR OF PHILOSOPHY

Approved by:

Chair of Committee, Ping Yang
Committee Members, Kenneth Bowman
Andrew Dessler
Hung-Lung Huang
George Kattawar
Thomas Wilheit
Head of Department, Kenneth Bowman

August 2008

Major Subject: Atmospheric Sciences

ABSTRACT

Satellite-based Remote Sensing of Cirrus Clouds: Hyperspectral Radiative Transfer Modeling, Analysis of Uncertainties in In-situ Cloud Extinction Measurements and Intercomparison of Cirrus Retrievals from A-train Instruments. (August 2008)

Zhibo Zhang, B.S., Nanjing University, China;

M.S., Texas A&M University

Chair of Advisory Committee: Dr. Ping Yang

This dissertation consists of three parts, each devoted to a particular issue of significant importance for satellite-based remote sensing of cirrus clouds.

In the first part, we develop and present a fast infrared radiative transfer model on the basis of the adding-doubling principle. The model aims to facilitate the radiative transfer computations involved in hyperspectral remote sensing applications. The model is applicable to a variety of cloud conditions, including vertically inhomogeneous or multilayered clouds. It is shown that for hyperspectral applications the model is two order-of-magnitude faster than the well-known discrete ordinate transfer (DISORT) model, while maintains a similar accuracy.

The second part is devoted to the investigation of uncertainties in the FSSP (Forward Scattering Spectrometer Probe) measurement of cloud extinction by small ice particles. First, the single-scattering properties of small ice particles in cirrus clouds are derived and compared to those of equivalent spheres

according to various definitions. It is found that, although small ice particles in cirrus clouds are often “quasi-spherical”, their scattering phase functions and asymmetry factors are significant different from those of ice spheres. Such differences may lead to substantial underestimation of cloud extinction in FSSP measurement, if small ice particles are assumed to be spheres.

In the third part, we present a comparison of cirrus cloud optical thickness retrievals from two important instruments, MODIS (Moderate Resolution Imaging Spectrometer) and POLDER (Polarization and Directionality of Earth’s Reflection), on board NASA’s A-train satellite constellation. The comparison reveals a large difference. Several possible reasons are discussed. It is found that much of the difference is attributable to the difference between the MODIS and POLDER retrieval algorithm in the assumption of cirrus cloud bulk scattering properties. Potential implications of the difference for climate studies are investigated. An important finding is that the use of an unrealistic cirrus bulk scattering model might introduce artificial seasonal variation of cirrus optical thickness and shortwave radiative forcing into the retrieval.

ACKNOWLEDGEMENTS

I am deeply grateful to my advisor, Dr. Ping Yang, for his wise guidance and tremendous support during my Ph.D. study. He is not only a good advisor, inspiring and encouraging us to achieve at the highest levels of science, but also a true mentor and friend who cares about our lives and future. I would also like to thank my committee members, Dr. Allen Huang at CIMSS/SSEC and Drs. George Kattawar, Andrew Dessler, Kenneth, Bowman and Thomas Wilheit at Texas A&M University, for their interests in my research and constructive comments they have given to me.

I would especially like to thank Drs. Bryan Baum and Jerome Riedi, for the helpful discussions with them and for their generous support and help on data and software. I would also like to thank Drs. Steven Platnick, Gerald North, Shaima Nasiri, Fuqing Zhang, Yongxiang Hu, Bin Lin and many others for their advice and help on my career. I am grateful to my group members, especially Drs. Heli Wei, Jianguo Niu, Pengwang Zhai and Gang Hong, for all their help on both my research and my life.

This study was partially supported by two NASA grants (NNG04GL24G and NNL06AA01A) and a NSF Grant (ATM-0239605).

Lastly, I would like to thank my wife Caihong Wen, the love of my life, for the loving support and patience she has given me all these years. I would also like to thank my family and friends, especially my father, Fengjun Zhang and my mother, Xiufen Zhang, for all the unconditional help throughout the years.

TABLE OF CONTENTS

Page

ABSTRACT……. iii

ACKNOWLEDGEMENTS……. v

TABLE OF CONTENTS…… vi

LIST OF FIGURES…… viii

LIST OF TABLES……... xi

I. INTRODUCTION……. 1

1.1 Cirrus clouds and their role in climate…… 1
1.2 Satellite-based remote sensing of cirrus clouds……... 4
1.2.1 Modeling the microphysical properties of cirrus clouds…… 4
1.2.2 Modeling the single-scattering properties of ice particles…… 7
1.2.3 Modeling the bulk scattering properties of cirrus clouds…….. 8
1.2.4 Radiative transfer in cirrus clouds and remote sensing of cirrus cloud properties from satellite-based instruments……. 9
1.3 Issues, challenges and new opportunities……. 11
1.4 Organization of the dissertation…….. 15

II. A FAST INFRARED RADIATIVE TRANSFER MODEL BASED ON THE ADDING-DOUBLING METHOD FOR HYPERSPECTRAL REMOTE SENSING APPLICATIONS…….. 17

2.1 Background…… 17
2.2 Methodology of FIRTM-AD…….. 22
2.3 Cloud realization scheme in FIRTM-AD…… 26
2.4 Development of the pre-computed look-up table for FIRTM-AD….. 30
2.5 Accuracy estimation of FIRTM-AD……. 34
2.6 Discussion and summary…… 47

III. AN INVESTIGATION OF THE OPTICAL PROPERTIES OF QUASI-SPHERICAL ICE PARTICLES: IMPLICATIONS FOR MEASURING ICE PARTICLE SIZE WITH FSSP-TYPE INSTRUMENTS…… 53

3.1 Background……..…….. 53

Page

3.2 Optical properties of Platonic solids……... 57
3.2.1 Geometries of Platonic solids…… 57
3.2.2 Single-scattering properties of Platonic solids in geometrical optics regime…… 60
3.3 Implications for measuring ice particle sizes with FSSP-type probes……..…….. 71
3.4 Conclusions…… 76

IV. A COMPARISON OF MODIS AND POLDER CIRRUS CLOUD OPTICAL THICKNESS RETRIEVALS……. 78

4.1 Background…… 78
4.1.1 MODIS operational cloud optical thickness retrieval algorithm 81
4.1.2 POLDER operational cloud optical thickness retrieval algorithm ……... 87
4.2 Comparison of MODIS and POLDER cirrus cloud optical thickness retrievals…… 92
4.2.1 Case selection…….. 92
4.2.2 MODIS/POLDER collocation…….. 95
4.2.3 Results…….. 98
4.2.4 Discussion…… 102
4.3 Implications for climate studies……..…… 114
4.4 Implications for the development of future cirrus cloud retrieval algorithms…… 120
4.5 Conclusions and summary……. 129

V. SUMMARY…….. 132

REFERENCES…….…….. 136

APPENDIX A…….. 154

APPENDIX B…….. 160

APPENDIX C…….. 161

VITA……..…….. 173

LIST OF FIGURES

FIGURE Page

2.1 Vertically inhomogeneous, absorptive and scattering, multilayered, plane-parallel atmosphere..... 23

2.2 (a) Schematic illustration of the “coexisting scheme”, (b) and the “approximate scheme”, which is used in FIRTM-AD as an approximation to the “coexisting scheme”. …..... 27

2.3 Temperature profile and the optical depth profiles at 8.5-, 11- and 12 μμ of the background atmosphere used in the computations..... 37

2.4 Application of FIRTM-AD to hyperspectral BT computations at TOA for single-layered clouds..... 39

2.5 Application of FIRTM-AD to hyperspectral BT computations at the surface for single-layered cloud conditions..... 43

2.6 The errors of FIRTM-AD in hyperspectral BT computations for a two-layered cirrus cloud..... 44

2.7 The errors of FIRTM-AD for a case where there are three layers of cirrus cloud in the atmosphere shown in Fig. 2.3..... 46

2.8 A look-up table for the cloud property retrieval using 11- and 12 μm channels..... 50

3.1 Geometries of the Platonic solids, i.e. the tetrahedron, hexahedron (or cube), octahedron, dodecahedron and icosahedron..... 57

3.2 Comparison of the extinction cross-section (C_e) and asymmetry factor (g) between the Platonic solids and their spherical equivalences at a wavelength of $\lambda = 0.66\ \mu m$ 63

3.3 Comparison of the extinction cross-section (C_e), single-scattering albedo (ω), and asymmetry factor (g) between the Platonic solids and their spherical equivalences at a wavelength of $\lambda = 11\ \mu m$ 66

3.4 Comparison of the scattering phase functions between the Platonic solids and sphere at a wavelength of $0.66\ \mu m$ 67

FIGURE Page

3.5 Same as Fig. 3.4, except for a wavelength of $11\mu m$ 70

3.6 This figure shows the sensitivity of FSSP measurement, i.e., the relative response function, to the diameter of water droplets. The optical properties of water droplet at the FSSP working wavelength, 632.8nm, are computed using the Lorenz-Mie code..... 72

3.7 Responses of FSSP to Platonic solids and their equivalent spheres. 74

4.1 Schematic of sun-satellite viewing geometry. θ_0 is the solar zenith angle, ϕ_0 is the solar azimuthal angle, θ_v is the sensor viewing zenith angle, , and ϕ_v the sensor azimuthal angle..... 82

4.2 The ice particle habit distribution used in the Baum05 model (Baum et al. 2005a)……..…... 85

4.3 a) The scattering phase functions of cirrus clouds in MODIS 0.86-μm band based different ice particle microphysics. b) The look-up tables for MODIS cirrus cloud optical thickness retrieval corresponding to the scattering phase functions in a)…….. 86

4.4 Schematic of POLDER angular sampling pattern……. 91

4.5 The true-color image of the selected MODIS/Aqua granule over the Central America on July 22, 2007 (UTC time 18:45)..... 93

4.6 GOES-12 and GOES-10 merged infrared (11mm) color images over Central America for a) 10:45 b) 12:45 c) 14:28 d) 16:45 e) 18:45 and f) 20:28 UTC, on July 22, 2007..... 94

4.7 Cloud top thermodynamic phase retrieval from MODIS (left panel) and POLDER (right panel) cloud products for the granule in Fig. 4.5 97

4.8 The cloud optical thickness of ice clouds in the granule of Fig. 4.5 according to MODIS (left panel) and POLDER (right panel) cloud products. Note that only pixels labeled as “ice cloud” by both MODIS and POLDER are plotted..... 99

4.9 A scatter plot of POLDER (τ_c^{POLDER}) versus MODIS (τ_v^{MODIS}) cirrus optical thickness retrieval, along with a linear fit (blue line) of τ_c^{POLDER} by $0.6827\tau_v^{MODIS}$. Note that the logarithm scale is used in both axes..... 100

FIGURE Page

4.10 The histograms of the ratio $\tau_c^{POLDER} / \tau_c^{MODIS}$ 101

4.11 A schematic of the “plane-parallel albedo bias”..... 103

4.12 Histogram of the cloud effective radius (r_e) of cirrus clouds in the selected granule retrieved by MODIS. The density function has been normalized with respect to its maximum value..... 105

4.13 Asymmetry factors of cirrus cloud for the wavelength of 0.86 μμ as a function of cloud effective radius. The black line with asterisks denotes the Baum05 model and the diamond corresponds to the IHM model..... 106

4.14 Same as Fig. 4.10 for the ratio $\tau_c^{A} / \tau_c^{MODIS}$ 109

4.15 Same as Fig. 4.10 for the ratio τ_c^{B} / τ_c^{A} 111

4.16 Same as Fig. 4.10 for the ratio τ_c^{C} / τ_c^{A} 113

4.17 The left panel shows the zonal mean optical thickness of cirrus clouds in the region 30o N to 30o S as function of moth in the year 2006 retrieved by MODIS. The right panel shows the corresponding retrieval from **PODLER.**..... 117

4.18 This figure shows the shortwave cirrus radiative forcing calculated based on the MODIS optical thickness retrieval + Baum05 model (left panel) or POLDER retrieval + IHM model (right panel). 118

4.19 The ratio of $\tau_c^{\mathrm{IHM}} / \tau_c^{\mathrm{Baum05}}$ versus scattering angle..... 122

4.20 A schematic of seasonal variation of MODIS scattering angle. In the figure, θ_0 denotes the solar zenith angle and θ_s denotes the scattering angle..... 123

4.21 Zonal mean MODIS scattering angle as a function of month..... 124

4.22 This figure illustrates schematically an example of the uncertainty caused by the use of an incorrect cirrus bulk scattering properties in deriving the seasonal variations of cirrus optical thickness and shortwave radiative forcing from MODIS radiance observations..... 125

LIST OF TABLES

TABLE		Page
2.1	The quadrature points of 32-stream double-Gaussian quadrature over the upward hemisphere and the corresponding zenith angles.....	33
2.2	The RMS BT errors of FIRTM-AD with respect to DISORT under the single-layered cloud conditions in the scenarios shown in Fig. 2.4. and the major error sources present in each scenario....	41
2.3	The RMS BT errors of FIRTM-AD with respect to DISORT under the two-layered cloud condition in the scenarios shown in Fig. 2.6 and the corresponding major error sources.....	45
2.4	* The computational efficiencies (in seconds per 100 wavenumbers) of FIRTM-AD and DISORT under the same conditions on an Apple 1.8GHz G5 computer.....	47
3.1	Values of δ_V , δ_S and $\delta'_{V/S}$ of Platonic solids…….……	59
3.2	The volume, surface area, R_a , R_v and R_{eff} of Platonic solids in a case where the radii of the spheres circumscribing the solids are all unity…….	60
4.1	Configurations of three experiments……..……	108
4.2	Statistics of the ratios, $\tau_c^{POLDER} / \tau_c^{MODIS}$, $\tau_c^A / \tau_c^{MODIS}$, τ_c^B / τ_c^A and τ_c^C / τ_c^A	114
4.3	Annual area-averaged τ_c and corresponding F_{sw} according to different model set-ups.....	119

I. INTRODUCTION

1.1. Cirrus clouds and their role in climate

Cirrus clouds are white and wispy clouds consisting of ice particles and usually inhabiting in the upper troposphere (Lynch 2002). Cirrus clouds cover about 20~40% of the Earth's surface (Wang et al. 1996; Wylie et al. 1994; Wylie and Menzel 1999) and interact strongly with both solar and infrared radiation fields, and therefore play an important role in the planetary radiation energy budget (Liou 1986; Ackerman et al. 1988; Hartmann et al. 1992; McFarquhar et al. 2000). Cirrus clouds reduce the solar radiation reaching the surface by reflecting the incoming sunlight back to space, which results in a surface cooling effect. At the same time, cirrus clouds reduce the outgoing longwave radiation (OLR) because of their strong absorption in the infrared region, resulting in a heating effect in the upper troposphere that may in turn heat up the surface. It has been shown that the strengths of these two opposing radiative effects of cirrus clouds depend sensitively on many factors, including the cloud fraction, lifetime, cloud optical thickness (τ), cloud top temperature (T_{top}), cloud particle effective radius (r_e) and cloud particle habit, as well as the amount and distribution of water vapor, surface reflectance and properties of water clouds or

---

This dissertation follows the style of *Journal of Atmospheric Sciences*.

aerosols below cirrus clouds (Ackerman et al. 1988; Jensen et al. 1994; Hartmann et al. 2001). Generally, the net cloud radiative forcing (CRF) of high and thin cirrus clouds is positive at TOA (McFarquhar et al. 2000), while the net CRF of thick anvils, with visible τ larger about 10, could be negative (Jensen et al. 1994). However, the radiative effects of cirrus in between are less understood and the aforementioned factors all serve to complicate the problem.

Cirrus clouds also affect climate through their role in the atmospheric water vapor budget. While the formation and persistence of cirrus clouds depend on the abundance and distribution of water vapor (Newell et al. 1996; Jensen et al. 1996) as well as the dynamical state of atmosphere, the distribution of water vapor in turn is also sensitive to the presence of cirrus clouds. Stratospheric water vapor is a strong greenhouse gas and plays a critical role in the stratospheric chemistry (Houghton et al. 2001). In the tropics, thin cirrus clouds are frequently observed near tropical tropopause (see e.g., Prabhakara et al. 1988; Wang et al. 1994; Dessler and Yang 2003). It has been suggested that these cirrus clouds could exert a freeze-drying effect on the air entering stratosphere, and therefore may play a role in regulating the budget of stratospheric water vapor. (Hartmann et al. 2001; Holton and Gettelman 2001; Jensen and Pfister 2004). Overall, the effect of cirrus clouds on water vapor budget is still not completely understood. This has made it one of the key scientific objectives of major cirrus measurement campaigns, such as CRYSTAL-FACE (or, Cirrus Regional Study of Tropical Anvils and Cirrus Layers - Florida

Area Cirrus Experiment, Jensen et al. 2004) and recent TC^4 (or Tropical Composition, Cloud and Climate Coupling) experiments.

The feedback of cirrus clouds also has important impact on the climate system (Stephens 2002). A perturbation of the climate system, which could be due to either external or internal forcing, usually leads also to changes in cloudiness, which in turn may either amplify or diminish the original perturbation. The feedbacks of cirrus clouds as well as other clouds to the anthropogenic climate change (e.g., increasing CO_2 and aerosols) are still poorly understood (Stephens 2005; Randall et al. 2006), which makes cloud feedback the "single greatest source of uncertainty in the estimates of climate sensitivity" (Houghton et al. 2001).

The climatic importance of cirrus clouds has lead to several measurement campaigns, e.g., CEPEX (Central Pacific Experiment), MidCiX (Mid Latitude Cirrus Cloud Experiment), TWP-ICE (Tropical Warm Pool International Cloud Experiment), CRYSTAL-FACE and recent TC^4 experiments. The observational data from these campaigns have greatly improved our understanding of the formation and life cycle (e.g., Heymsfield and Miloshevich 1995, 1993; DeMott et al. 1998; Cziczo et al. 2004), microphysical and optical properties of cirrus clouds (e.g., Dowling and Radke 1990; McFarquhar and Heymsfield 1996; Heymsfield et al. 1998; Garrett et al. 2003), their role in the climate system (e.g., McFarquhar et al. 2000). These in-situ measurement data have become the foundation of cirrus cloud modeling for GCMs and satellite remote sensing. However, *in situ* observations are expensive and limited by their small spatial and temporal

sampling scales. To improve our understanding of cirrus clouds, continuous global observations of cirrus clouds from satellite-based instruments are indispensable.

1.2. Satellite-based remote sensing of cirrus clouds

Despite the substantial efforts and significant progress made over the last decade, reliable retrieval of cirrus properties from satellite measurements still remains a challenge. Not only does it require good understanding of the characteristics and capabilities of the instruments, but it also requires good understanding of several different aspects of cirrus clouds. First of all, remote sensing of cirrus clouds requires a good understanding of the microphysical and single-scattering properties of the ice particles in cirrus clouds. Secondly, the interpretation of satellite measurements demands knowledge of the radiative transfer process in cirrus clouds as well as in their surrounding environments. Finally, cirrus remote sensing requires, of course, reliable retrieval algorithms

1.2.1. Modeling the microphysical properties of cirrus clouds

Cirrus clouds almost exclusively consist of nonspherical ice particles. Thus, modeling cirrus clouds for climate models and satellite remote sensing must begin with understanding of the microphysical properties of these ice particles. As a matter of fact, cirrus clouds are modeled as plane-parallel and homogeneous (in terms of ice particle microphysics) cloud layers in most current

satellite remote sensing algorithms. Within this context, two microphysical factors, namely, ice particle size and shape distributions, are of paramount importance and largely determine the radiative properties of a cirrus cloud (Takano and Liou 1989b, a; Slingo 1989; Ebert and Curry 1992).

In situ measurements show that the size of ice particles within the same cirrus cloud can range from a few micrometers to a few millimeters (Auer and Veal 1970). However, it is found that the radiative properties of cirrus clouds, such as their reflection function, are not dependent on the exact nature of the cloud particle size distribution (Hansen and Travis 1974). Instead, they depend primarily on the effective radius, r_e, and the shapes of ice particles in cirrus clouds. A most widely used definition of the effective radius is as follows (Foot 1988):

$$r_e = \frac{3}{4}\frac{V_{total}}{P_{total}}, \tag{1.1}$$

where V_{total} and P_{total} are the total volume and projected area of ice particles within a unit volume of cirrus cloud. The importance of r_e can be immediately appreciated from Eq. (1.1). It is defined so that r_e describes the relationship between two most fundamental and important aspects of cirrus clouds, ice water content (IWC) and extinction coefficient (β_e). A different form of Eq. (1.1) is

$$r_e = \frac{3}{4}\frac{IWC\langle Q_e \rangle}{\rho_{ice}\beta_e}, \tag{1.2}$$

where $\langle Q_e \rangle$ is the averaged extinction efficiency of ice particles and ρ_{ice} is the density of ice. The above equation reveals that the optical thickness ($\tau = \beta_e \Delta z$) of cirrus is inversely proportional to r_e in the visible region where $\langle Q_e \rangle$ is approximately a constant of 2. r_e also plays an important role in the lifetime of cirrus clouds and precipitations associated with them. The terminal velocity of ice particles depends primarily on their sizes and also on their shapes and density (Heymsfield 1972). This dependence is the reason that the sedimentation of cirrus cloud is usually parameterized as a function of r_e in climate models (Boville et al. 2006).

The shape of ice particles is a crucial factor, firstly, because it plays a role in determining the effective size of cirrus clouds. Different shapes have different volume-to-surface area ratios, and therefore different effective radii according to Eq. (1.1). The shapes of natural ice particles can vary from simple pristine hexagonal prisms to complex aggregates and fractal polycrystals (Pruppacher and Klett 1997; Heymsfield 2003). Theoretical modeling of the light scattering by nonspherical particles show that the single-scattering properties of ice particles with different shapes but same size may differ dramatically, especially in the shortwave region (see e.g., Yang and Liou 1998; Zhang et al. 2007). Therefore, an unrealistic representations of ice particle shapes in the retrieval algorithms of these instruments may lead to substantial errors in retrieved cirrus cloud properties (see e.g., Rolland et al. 2000; Yang et al. 2007).

Given the importance of the effective particle radius and ice particle shapes, it is not surprising that a large panel of *in-situ* instruments has been developed to measure these properties. For example, one of the most widely used aircraft-based instruments for the measurement of ice particle size and number concentration is the forward scattering spectrometer probe (FSSP Knollenberg 1981). The *in-situ* measurements of cirrus cloud obtained from these instruments during the past few field campaign have dramatically expanded our knowledge of cirrus clouds, especially their microphysics (e.g., Dowling and Radke 1990; McFarquhar and Heymsfield 1996; Heymsfield et al. 1998; Garrett et al. 2003). However, as will be discussed later in section 3, the *in-situ* measurements are still subject to interpretation and some debate regarding their ability to provide radiatively relevant ice particle microphysical properties.

1.2.2. Modeling the single-scattering properties of ice particles

The interaction of an individual ice particle and radiation is controlled by the single-scattering properties of the ice particle. Among many others, important single-scattering properties include the extinction cross-section, C_e, single-scattering albedo, ω, and scattering phase function, P_{11}. The extinction cross-section is analogous to the geometrical cross-section of a particle, except that it denotes the cross-section in terms of removing energy from the original beam by the particle (Liou 2002). The single-scattering albedo specifies the ratio between absorbed and scattered energy during the scattering process (Liou 2002). The

scattering phase function determines the spatial distribution of the scattered radiation (Liou 2002).

Substantial advances in modeling the single-scattering properties of nonspherical particles have been made over the last decade along with the growth of computer capabilities. Many numerical models have been developed based on various methods. Some popular methods include the finite-difference time-domain (FDTD) method (e.g., Taflove and Hagness 2000; Yang and Liou 1996a), the discrete dipole approximation (DDA) method (e.g.,Draine and Flatau 1994), the T-matrix method (e.g., Mishchenko et al. 1996) and the geometrical-optics method Salomonson et al. a.k.a. the ray-tracing method (e.g., Macke et al. 1995; Takano and Liou 1989b; Yang and Liou 1996b). The advantages and limitations of these methods have been reviewed by Wriedt (Wriedt 1998), Mishchenko et al. (Mishchenko et al. 2000), and Kahnert (Kahnert 2003).

1.2.3. Modeling the bulk scattering properties of cirrus clouds

The difference between single-scattering and bulk scattering property is that the former specifies how individual ice particles interact with radiation, while, in some sense, the latter determines how a unit volume of cirrus clouds interacts with the radiation. In practice, the bulk scattering properties are obtained by averaging the single-scattering properties of ice particle over both particle size and habit distribution (Baum et al. 2005b). For example, the bulk scattering phase function, $\langle P_{11} \rangle$, of cirrus clouds is derived from the following equation (Baum et al. 2005b):

$$\langle P_{11} \rangle = \frac{\int_{D_{\min}}^{D^{\max}} \left[\sum_{h=1}^{M} P_{11,h}(D) C_{s,h}(D) f_h(D) \right] \times n(D) dD}{\int_{D_{\min}}^{D^{\max}} \left[\sum_{h=1}^{M} C_{s,h}(D) f_h(D) \right] \times n(D) dD}, \quad (1.3)$$

where D is the ice particle size, $n(D)$ denotes number density of ice particles with size from D to $D + dD$. The value of $n(D)$ is specified by the particle size distribution (PSD). f_h is the ice particle habit fraction for habit h, M is the number of habits. $C_{s,h}(D)$ and $P_{11,h}(D)$ are, respectively, the scattering cross-section and single-scattering phase function of an ice particle with habit of h (i.e., hexagonal column or bullet rosette) and size of D.

1.2.4. Radiative transfer in cirrus clouds and remote sensing of cirrus cloud properties from satellite-based instruments

In the context of satellite-based remote sensing of cirrus clouds, radiative transfer solves the "forward problem":

$$\mathbf{Y} = F(\mathbf{X}). \quad (1.4)$$

That is, what are the expected satellite observations, given the microphysical, and corresponding bulk scattering properties of cirrus clouds? In Eq. (1.4), $\mathbf{X}$ represents the above-described bulk scattering properties of cirrus clouds and the radiative properties of their surrounding environments, such as the reflectance of surface and transmissivity of atmosphere. $\mathbf{Y}$ represents the radiances observed by satellite-based instruments. F represents the radiative transfer process.

In contrast, remote sensing solves the “inverse problem”:

$$\mathbf{X} = F^{-1}(\mathbf{Y}). \tag{1.5}$$

That is, for given satellite measurements, what is the most likely state of the cirrus clouds? From this perspective, radiative transfer is the foundation of remote sensing and remote sensing is one of the most important applications of radiative transfer.

Many theoretical and numerical radiative transfer models have been developed based on various methods, such as the discrete-ordinate method (Chandrasekhar 1960; Stamnes et al. 1988; Liou 1973), the spherical harmonics method (Evans 1998), the Monte Carlo method (Collins et al. 1972; Plass and Kattawar 1968) and the adding-doubling method (Hansen and Hovenier 1971; Irvine 1968; Lacis and Hansen 1974; Twomey et al. 1966; van de Hulst 1980; Hansen 1971; de Haan et al. 1987; Hovenier et al. 2004). Most of these models, if not all, have been employed in remote sensing applications, such as the satellite-based remote sensing of cirrus cloud properties.

A large panel of satellite-based instruments, such as the Moderate-resolution Imaging Spectroradiometer (MODIS) and the Polarization and Directionality of the Earth's Reflectances (POLDER), has been launched to study the global distribution and properties of clouds. To retrieve these cloud properties from satellite measurements, more or less radiative transfer computations are required. For example, the bi-spectral look-up table method developed by Nakajima and King (Nakajima and King 1990) is employed in the current MODIS operational algorithm to retrieve the optical thickness and effective radius of

cirrus clouds from MODIS observations (Platnick et al. 2003). In this method, the key component is an extensive look-up table containing cloud reflection functions corresponding to various cloud microphysical properties and sun-satellite viewing geometries. With this look-up table, cloud optical thickness and effective radius can be retrieved simultaneously from cloud reflection observations from two MODIS bands (Nakajima and King 1990). To generate such look-up table, single-scattering properties of various ice particles habits with sizes ranging from a few microns to a few millimeters at the wavelengths of interest, i.e., MODIS bands, are first computed using the aforementioned scattering models (Yang et al. 2000; Yang et al. 2005). In the second step, single-scattering properties are averaged into bulk scattering properties of cirrus clouds on basis of *in-situ* measurements of ice particle size and habit distributions (Baum et al. 2005a; Baum et al. 2005b). Finally, the bulk scattering properties of cirrus clouds from the previous step are used as inputs for radiative transfer model to simulate the reflection functions of clouds under various conditions (i.e., the look-up table) (Platnick et al. 2003).

1.3. Issues, challenges and new opportunities

As described in the previous section, satellite-based remote sensing of cirrus clouds requires good understanding of several different aspects of these clouds as well as the knowledge of radiative transfer process and retrieval methods.

Unfortunately, there still exist many controversial issues that hamper the interpretation of satellite observations of cirrus clouds and obscure our

understanding the role of cirrus clouds in climate. For example, one of the biggest uncertainties in modeling the effective radius of cirrus clouds is associated with the small ice particles (sizes smaller than about 50 μm) in cirrus clouds. Due to our inadequate understanding of these ice particles, their concentration, microphysical and optical properties and consequently their role in determining the radiative properties of cirrus clouds have long been controversial issues. An important reason for this situation is related to the dubious reliability of conventional cloud particle probes, such as the aforementioned FSSP (Knollenberg 1981) on the measurements of small ice particles. It is known that FSSP tends to overestimate the number concentration of small ice particles because of shattering of large ice particles at the inlet of FSSP (Gayet et al. 1996a; Field et al. 2003). Additional uncertainties come from the shapes of small ice particles. To derive cloud properties, such as cloud extinction coefficient, from measurements of FSSP-type probes, some empirical assumptions on ice particle shapes must be made and, quite often, small ice particles are assumed to be spheres. It is still under debate whether such assumption may lead to serious errors in FSSP ice particle measurements (e.g., Heymsfield et al. 2006; Garrett 2007).

Recent advances in remote sensing technologies, such as NASA's "A-Train" satellite constellation, have provided unprecedented opportunities to improve our understanding of cirrus clouds. The Afternoon or "A-Train" satellite constellation consisting of six polar-orbiting satellites flying one after another in close proximity will be completely formed in the near future (Stephens et al.

2002). The near simultaneous data from these satellites will provide comprehensive information about aerosols, clouds, temperature, relative humidity, radiative fields, and other important atmospheric components, and therefore an unprecedented opportunity to gain better understanding of some important issues such as climate change, cloud feedbacks (Stephens 2005) and effects of aerosols in the climate (Anderson et al. 2005). Some key instruments for cirrus cloud retrievals on board of “A-Train” include the aforementioned MODIS and POLDER on board of Aqua and Parasol, respectively, the Advance Infrared Sounder (AIRS, Aumann et al. 2003) on Aqua, the Cloud-Aerosol Lidar with Orthogonal Polarization (CALIOP, Winker et al. 2003) on Calipso, and the Cloud Profiling Radar (CPR, Stephens et al. 2002) on CloudSat. Each of these instruments has unique measurement capabilities that greatly complement each other. Comparison and combination of their retrievals have the potential to significantly improve our knowledge of the microphysical and radiative properties of cirrus clouds.

Along with the opportunities also come new challenges. For example, with more than 2000 spectral channels, AIRS has an unprecedented spectral resolution and therefore provides more accurate information on the vertical profiles of atmospheric temperature, moisture and minor gases (e.g., McMillan et al. 2005; Aumann et al. 2003; Tian et al. 2006). However, the other side of the coin is that the volume of AIRS data is enormous because of its high-spectral resolution nature. This makes the interpretation of AIRS observations a challenging task and necessitates the development of highly efficient radiative

transfer models. A number of clear-sky fast radiative transfer models have been developed and proved to be very useful for interpreting AIRS observations under clear-sky conditions (e.g., McMillin et al. 1995; Strow et al. 2003; Moncet et al. 2004; Liu et al. 2006). In comparison, fast cloudy-sky radiative transfer models, which can account for both absorption by atmospheric gases and scattering and absorption by cloud particles, are still at the preliminary stage. At present, there are only a couple of such models available (e.g., Niu et al. 2007; Wei et al. 2004) and there still remains potential space to improve these models. Nevertheless, the usefulness of these models in cloud property retrieval using AIRS data has been demonstrated in several recent studies (e.g., Huang et al. 2004; Li et al. 2005a; Wei et al. 2004). Moreover, Zhou et. al. (Zhou et al. 2007) has showed the possibility to retrieve atmospheric profiles simultaneously with cloud properties on the basis of fast cloudy-sky radiative transfer models. Thus, the improvement of currently existing and development of new cloudy-sky radiative transfer models for hyperspectral applications are challenging and yet rewarding tasks.

The “A-Train” satellite constellation also provides an excellent opportunity to compare nearly simultaneous cloud retrievals from difference satellite instruments. Both MODIS and POLDER retrieve the optical thickness of cirrus clouds. Because optical thickness plays an important role in determining cloud radiative forcing (Jensen et al. 1994), it is of interest to compare this important cloud parameter retrieved from MODIS and POLDER. Such comparison will not only reveal differences between MODIS and POLDER cloud products, but may

also help answer some crucial questions in satellite-based remote sensing of cirrus clouds. For instance, there currently exists divergent view of radiatively representative shape of ice particles. In the current MODIS operation retrieval algorithm (Collection 5), an ice particle ensemble model consisting of six ice particle habits is used (Yang et al. 2000; Yang et al. 2005; Baum et al. 2005b). In current POLDER cirrus retrieval algorithm, all ice particles are assumed to be "inhomogeneous hexagonal monocrystal" (IHM, Laurent et al. 2000; Buriez et al. 2005). An important question, which may be answered through comparison, is that whether such divergent understanding of the bulk scattering properties of cirrus ice particles has led to substantially different cirrus retrievals and, more importantly, cirrus radiative forcing estimations.

1.4. Organization of the dissertation

The rest of this dissertation is organized into three major sections, each devoted to a particular issue that has been briefly introduced in the previous section.

In section II, we present a fast cloudy-sky infrared radiative transfer model based on the adding-doubling method for hyperspectral applications. In section III, we will first study the optical properties of small quasi-spherical ice particles in cirrus clouds and then investigate the uncertainty in FSSP measurement of ice particle extinction measurements. In section IV, we first present a comparison of cirrus optical thickness retrievals from MODIS and PODLER. Then, several factors potentially responsible for the differences between the two retrievals are

investigated and the potential implications of the differences for climate studies are discussed.

II. A FAST INFRARED RADIATIVE TRANSFER MODEL BASED ON THE ADDING-DOUBLING METHOD FOR HYPERSPECTRAL REMOTE SENSING APPLICATIONS*

2.1. Background

The high-spectral-resolution or hyperspectral sensors in the infrared, e.g., the Atmospheric Infrared Sounder (AIRS) (Aumann et al. 2003), the Cross-Track Infrared Sounder (Bloom 2001), the Infrared Atmospheric Sounding Interferometer (IASI) (Siméoni et al. 1997; Blumstein et al. 2004), and the Atmospheric Emitted Radiance Interferometer (AERI) (Knuteson et al. 2004b; Knuteson et al. 2004a), provide a wealth of information about the atmosphere, land and oceans, and therefore offer an unprecedented opportunity for the study of the earth-atmosphere system. At the same time, the analysis of the resulting hyperspectral data poses new challenges to the efficiency and accuracy of the current RT modeling capabilities. As an essential component in the implementation of the retrieval and data assimilation algorithms based on hyperspectral measurements, a RT model must be computationally efficient, and

*Reprinted with permission from "A fast infrared radiative transfer model based on the adding-doubling method for hyperspectral remote-sensing applications" by Z. Zhang, P. Yang, G. Kattawar, H. L. Huang, T. Greenwald, J. Li, B. A. Baum, D. K. Zhou, and Y. Hu, 2007. *Journal of Quantitative Spectroscopy & Radiative Transfer*, 105, 243-263, Copyright by Elsevier

yet have appropriate accuracy and general applicability under all conditions. For clear-sky atmospheres, a number of fast RT models have been developed, e.g., the optical path transmittance (OPTRAN) (McMillin et al. 1995), the stand-alone radiative transfer algorithm (SARTA) (Strow et al. 2003), the optimal spectral sampling model (OSS) (Moncet et al. 2004), and the principal component based radiative transfer model (PCRTM) (Liu et al. 2006).

Global analysis of data from the High Resolution Infrared Radiometer Sounder indicates that approximately 65-70% of the Earth's surface is generally covered by clouds. The HIRS field of view (FOV) is approximately 18 km at nadir. It is estimated that only 6.5% of the HIRS footprints are "clear-sky" (Saunders 2000). For AIRS, which has a slightly smaller FOV than HIRS with a spatial resolution of approximately 15 km at nadir, only 4.5% of the data over ocean have mean residual cloud fraction less than 0.6% (Goldberg et al. 2003). Therefore, RT models for cloudy conditions, which can account for both the absorption of the atmospheric gases and the scattering and absorption of cloud particles, are required for cloud clearing (Li et al. 2005b), cloud property retrieval (Li et al. 2005a; Wei et al. 2004) and satellite data assimilation (Saunders et al. 1999) from hyperspectral measurements. In previous research, a simplified cloudy RT model coupled with the OSS model has been employed in a newly developed inversion algorithm for dealing with both clear and cloudy radiances in retrieving atmospheric and cloud parameters (Zhou et al. 2007). The primary objective of this work is to develop an accurate, flexible and efficient radiative transfer equation (RTE) solver that can be easily coupled with a clear-sky model

to provide a complete and efficient RT computational package for applications to hyperspectral remote sensing.

The multiple-scattering term in the RTE is responsible for the difficulty associated with the development of an efficient RTE solver. The numerical computation of this term not only determines the complexity and accuracy of a RT model but also has a direct impact on its computational efficiency. Because multiple-scattering in the IR spectral region is not as strong as in the shortwave spectral region, this complex process is largely simplified, if not ignored altogether, in most IR remote sensing applications. For example, the upwelling radiances at the top of the atmosphere (TOA) in the IR region for a completely overcast field-of-view have been approximated in the literature as follows (e.g., Inoue 1985, 1987; Ou et al. 1993; Parol et al. 1991; Wu 1987):

$$I_{TOA} = \varepsilon B(T_c) + (1-\varepsilon) I_0 \tag{2.1}$$

where I_{TOA} is the radiance at the TOA, B is the Planck function, T_c is the cloud temperature, I_0 is the radiance reaching the cloud base, and ε is cloud emissivity that is usually assumed to be $1-\exp(-\tau_a / \mu)$ where τ_a is the optical thickness of the cloud due to the absorption and μ is the cosine of the viewing angle. Due to the neglect of cloud reflection in Eq.(2.1), some thermal energy that should have been reflected back to the surface penetrates through the cloud as an artifact in the simulation, resulting in an overestimation of the radiances at TOA.

For inferring cloud height and optical thickness from satellite observations, Minnis et al. (Minnis et al. 1998; Minnis et al. 1993) developed an efficient RT

model by parameterizing the TOA visible reflectance and IR emittance using the LUTs of cloud reflectances and emittances under various cloud microphysical and optical conditions. To facilitate the retrieval of ice cloud optical thickness and effective particle size from AIRS data, Wei et al. (Wei et al. 2004) developed a fast infrared RT model (hereafter, FIRTM1) to compute the TOA radiances for a cloudy atmosphere containing a single-layered, homogenous and isothermal cloud. With a pre-computed LUT for cloud reflectance and transmittance, FIRTM1 is approximately three orders of magnitude faster than the well-known DISORT model developed by Stamnes et al. (Stamnes et al. 1988). FIRTM1 is based essentially on an extension of Eq.(2.1). In addition to the two terms on the right hand side of Eq.(2.1), two additional terms representing the thermal emission by the atmosphere above the cloud and the corresponding reflection by the cloud are also taken into account in FIRTM1. Most recently, Niu et al. (Niu et al. 2007) extended the FIRTM1 to two-layered cloudy atmospheres (FIRTM2) by adding several more terms to Eq. (2.1). The above models are computationally efficient and also more accurate than the simple approximation in Eq. (2.1)due to the consideration of multiple-scattering. However, the flexibility of these models is limited because the radiative transfer equations were simplified to obtain optimal efficiency for a particular type of application, specifically computations of TOA radiances for which there are only one or at most two homogenous and isothermal cloud layers. Therefore, these models cannot be applied to retrieval implementations involving multilayered clouds or ground-based measurements.

Many robust and rigorous RT models have been developed that can fully account for multiple scattering, such as the discrete-ordinate method (Chandrasekhar 1960; Stamnes et al. 1988; Liou 1973), the spherical harmonics method (Evans 1998), the Monte Carlo method (Collins et al. 1972; Plass and Kattawar 1968) and the adding-doubling method (Hansen and Hovenier 1971; Irvine 1968; Lacis and Hansen 1974; Twomey et al. 1966; van de Hulst 1980; Hansen 1971; de Haan et al. 1987; Hovenier et al. 2004). Although these models have been widely used in narrowband remote sensing applications, the computational burden of applying them directly to a broader spectral range with a fine resolution is unlikely to be computationally affordable in practice. However, with some modification of the algorithms to account for the computational requirements of hyperspectral computations, the efficiency of these models can be improved substantially. For example, Moncet and Clough (Moncet and Clough 1997) developed a fast RT model using the adding-doubling method, referred to as CHARTS (Code for High-resolution Accelerated Radiative Transfer with Scattering), to interpret observations of water clouds for a high spectral resolution atmospheric emitted radiance interferometer (AERI). The advantage of CHARTS is that the time-consuming doubling step is performed only at selected wavelengths in a given spectral region of interest. The bulk radiative properties of the cloud layer for other wavelengths are interpolated from the computed ones. This modification of the adding-doubling algorithm is feasible due to the fact that the scattering properties of water droplets vary with the wavelength much more smoothly than the absorption of atmospheric gases. Although CHARTS is much

faster than DISORT, the doubling and interpolation step still uses more than half of the total CPU time. This computational burden is expected to increase for ice cloud applications because the strong forward scattering of ice particles requires the use of more Legendre terms in the expansion of the phase function and consequently more streams for the adding-doubling operations.

High-level ice clouds comprise as much as 30% of the cloud cover (Wylie and Menzel 1999; Wylie et al. 1994) and play an important and yet not well-understood role in the climate system (Liou 1986; Lynch 2002). A fast and yet robust RT model with general applicability can be quite useful not only for hyperspectral remote sensing applications but also for satellite data assimilation and climate study. Inspired by the virtues of FIRTM1/FIRTM2 and CHARTS, we develop a new fast infrared radiative transfer model based on the adding-doubling principle (FIRTM-AD) with an emphasis on applications to ice clouds. The methodology of FIRTM-AD is described in Section 2.2. The cloud realization scheme used in FIRTM-AD is discussed in Section 2.3. The development of a LUT for ice cloud radiative properties for FIRTM-AD is given in Section 2.4. In Section 2.5, we show the accuracy of FIRTM-AD in some typical applications. Finally, a brief summary of the present study is given in Section 2.6.

2.2. Methodology of FIRTM-AD

For a vertically inhomogeneous, multilayered, plane-parallel atmosphere as shown in Fig. 2.1, we need both a clear-sky RT model that accounts for the molecular absorption and a numerical RTE solver that accounts for the multiple-

scattering in cloud and aerosol layers. The adding-doubling method is a rigorous method that has been used extensively in the development of numerical RTE solvers for plane-parallel atmospheres (e.g.,Hansen and Hovenier 1971; Irvine 1968; Lacis and Hansen 1974; Twomey et al. 1966; van de Hulst 1980; Hansen 1971; de Haan et al. 1987; Hovenier et al. 2004). The basics of the adding-doubling method and its application to radiative transfer in the thermal infrared region are outlined in Appendix A. As discussed in the Appendix, for the spectral region considered in the present study, i.e. 800- to 1300 cm^{-1}, the azimuthally-dependent solar contribution to the sensor observations is insignificant, so that

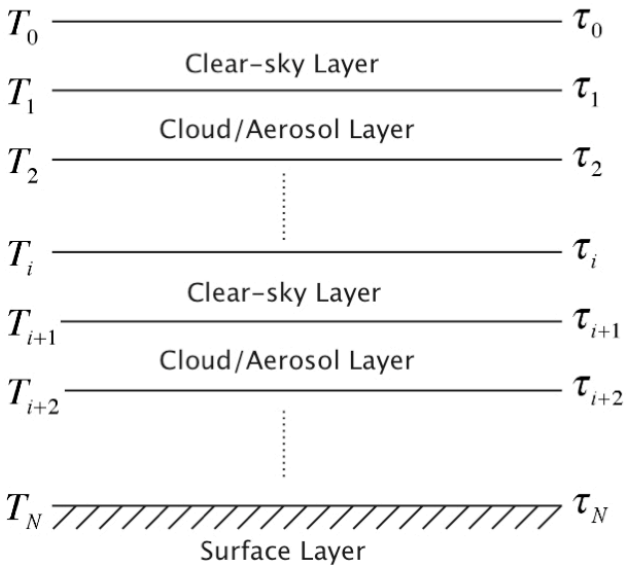

Figure 2.1 Vertically inhomogeneous, absorptive and scattering, multilayered, plane-parallel atmosphere.

only the azimuthally averaged bidirectional reflection ($\bar{\mathbf{R}}$) and transmission ($\bar{\mathbf{T}}$) matrices and the thermal emission vector ($\mathbf{E}$) (see Appendix A for their definitions) are required for the adding-doubling method. To obtain these

properties for cloud/aerosol layers (note that the clear-sky layers have an analytical solution), the doubling method can be used. In this method, a cloud/aerosol layer in Fig. 2.1 is first divided into a number of identical sub-layers. The optical thicknesses of the sub-layers are very small ($\tau_k \sim 2^{-10}$) (Wiscombe 1976a, b, 1977a), so that their $\bar{\mathbf{R}}_k$, $\bar{\mathbf{T}}_k$, and emissivity vector, $\boldsymbol{\varepsilon}_k$, (the subscript k indicates that the property is associated with the k^{th} sub-layer) may be obtained analytically from the cloud bulk scattering properties, i.e., the extinction efficiency ($\langle Q_e \rangle$), scattering albedo ($\langle \varpi \rangle$) and phase function ($\langle P \rangle$), under the single-scattering approximation. Because each sub-layer is isothermal, its thermal emission $\mathbf{E}_k$ is simply $\boldsymbol{\varepsilon}_k \mathrm{B}(T_k)$, where T_k is the temperature of the sub-layer. Finally, the $\bar{\mathbf{R}}$, $\bar{\mathbf{T}}$ and $\mathbf{E}$ of entire cloud/aerosol layer is obtained by adding at each step two identical layers, i.e., the doubling process (see Appendix A for details). Although the computational efficiency of the doubling method is sufficient for computations at a small number of spectral wavelengths, the computational burden increases greatly if a few hundred or even thousands of wavelengths are involved such as in the case of hyperspectral remote sensing.

The intent of FIRTM-AD is to reduce the computational burden associated with the doubling process, whereas the model still retains the robustness and high accuracy that the adding-doubling method offers. This is achieved through the use of an extensive pre-computed LUT of $\bar{\mathbf{R}}$, $\bar{\mathbf{T}}$ and $\boldsymbol{\varepsilon}$ for various ice clouds in conjunction with efficient interpolation schemes in the model. Following CHARTS (Moncet and Clough 1997), FIRTM-AD computes the $\bar{\mathbf{R}}$, $\bar{\mathbf{T}}$ and $\boldsymbol{\varepsilon}$ of clouds only at a few dozens of selected spectral points in the LUT. The $\bar{\mathbf{R}}$, $\bar{\mathbf{T}}$

and $\boldsymbol{\varepsilon}$ at other wavelengths (wavenumbers) in the interested spectral region are efficiently interpolated from the computed ones. At the selected spectral points, the burden associated with the computations of cloud $\bar{\mathbf{R}}$, $\bar{\mathbf{T}}$ and $\boldsymbol{\varepsilon}$ is also alleviated by the use of the pre-computed LUT. In FIRTM-AD, if a cloud is homogenous in terms of bulk scattering properties, the its $\bar{\mathbf{R}}$ and $\bar{\mathbf{T}}$ are either directly obtained or interpolated from the pre-computed LUT, and therefore the doubling process may be avoided. An inhomogeneous cloud is implemented in FIRTM-AD by superposition of homogenous sub-layers. For the computation of thermal emission by non-isothermal clouds, the doubling method described above is also used in FIRTM-AD. However, due to the use of the pre-computed LUT, the non-isothermal cloud can be divided into much thicker and therefore fewer sub-layers, leading to a much faster doubling process in FIRTM-AD than in the conventional adding-doubling method. The implementation of non-isothermal clouds in FIRTM-AD and the computation of their thermal emission will be discussed in the next section.

The applicability of the pre-computed LUT in RT models is a consequence of the fact that only three parameters, namely the incident wavelength (λ) or wavenumber (v), cloud optical thickness (τ) and effective particle size (D_e) are sufficient to determine the $\bar{\mathbf{R}}$, $\bar{\mathbf{T}}$ and $\boldsymbol{\varepsilon}$ of a cloud layer in most remote sensing implementations and radiative transfer simulations (Ebert and Curry 1992; Slingo 1989). A limitation of the LUT-based RT models such as FIRTM-AD and FIRTM1/FIRTM2, is that, while they may be computationally efficient, the applicability of these models is confined by the scope of the cloud conditions built

into the LUT. Use of a pre-computed LUT also raises the issue pertaining to the accuracy of the models, because interpolation is required to obtain the cloud properties that are not explicitly specified at the LUT grid points. The development of the pre-computed LUT for FIRTM-AD and the accuracy of FIRTM-AD will be discussed later.

2.3. Cloud realization scheme in FIRTM-AD

FIRTM-AD is a numerical RTE solver developed to account for the multiple-scattering process in cloud layers. Similar to other RTE solvers such as DISORT (Stamnes et al. 1988), FIRTM-AD depends on the availability of an accurate clear-sky RT model to account for the molecular absorption and provide an optical thickness profile of the background atmosphere. This directly leads to the issue of cloud realization, or more broadly, how to insert the cloud/aerosol layers into the background atmosphere. As illustrated in Fig. 2.2a, a physically sound scheme is to assume that the cloud and atmospheric gases coexist in a model layer (hereafter, referred to as “coexisting scheme”). In the RTE, the

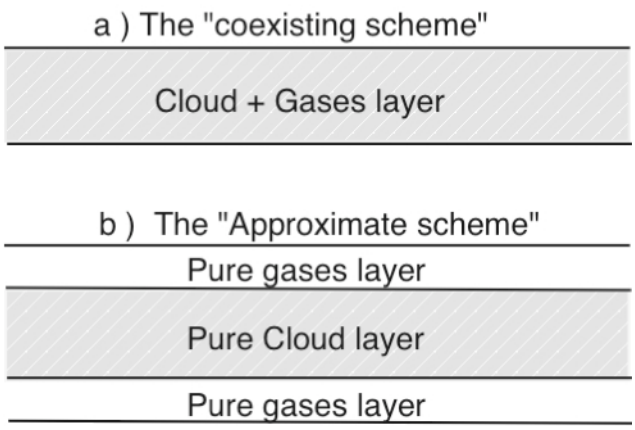

Figure 2.2. (a) Schematic illustration of the “coexisting scheme”, (b) and the “approximate scheme”, which is used in FIRTM-AD as an approximation to the “coexisting scheme”.

coexistence results in the increase of the optical thickness and the decrease of the single scattering albedo of a cloud-gas coexisting model layer in comparison with a layer consisting solely of cloud particles, due to the absorption of the atmospheric gases. The total optical thickness, τ_{layer}, and the albedo, ϖ_{layer}, of cloud-gases coexisting model layer in Fig. 2.2a can be expressed as:

$$\tau_{layer} = \tau_{gas} + \tau_{cloud}, \tag{2.2}$$

$$\varpi_{layer} = \frac{\varpi_{cloud}}{1 + \tau_{gas} / \tau_{cloud}}, \tag{2.3}$$

where τ_{cloud} and ϖ_{cloud} are the optical thickness and albedo of a layer consisting solely of cloud particles, respectively. The variable τ_{gas} is the optical thickness of the background atmosphere. It is straightforward to implement the “coexisting scheme” by redefining optical thickness and albedo of the layer according to Eq. (2.2) in a RT model that explicitly computes the cloud bulk radiative properties,

such as DISORT. However, it is difficult to implement the “coexisting scheme” in FIRTM-AD, because it is impractical to develop a LUT of $\bar{\mathbf{R}}$, $\bar{\mathbf{T}}$ and $\boldsymbol{\varepsilon}$ for cloud-gas coexisting layers due to a wide range of variations of the τ_{gas} in Eqs. (2.2) and (2.3). Instead, the LUT in FIRTM-AD is for pure cloud layers only and the approach (hereafter referred to as the “approximate scheme”) illustrated in Fig. 2.2b is used to derive the $\bar{\mathbf{R}}$, $\bar{\mathbf{T}}$ and $\boldsymbol{\varepsilon}$ of a cloud-gas coexisting layer from the LUT for pure clouds and a given value of τ_{gas}. In this approach, the cloud layer is specified at the middle level of a background atmosphere layer. In the current version of FIRTM-AD, the optical thicknesses of the upper and lower pure gas layers are specified as $\tau_{gas}/2$.

Another important cloud realization issue in FIRTM-AD as well as in other infrared (IR) RT models is how to implement a non-isothermal cloud. Observations show that even cirrus clouds can have a non-negligible physical thickness (Sassen and Campbell 2001). As a result, there may be a considerable temperature difference between the cloud top and cloud base. An IR-based RT model should be able to simulate this temperature variation within the cloud to account for its effect on the thermal emission of the cloud. In the conventional adding-doubling model, because a cloud layer is divided into a large number of thin sub-layers to initialize the doubling process, the cloud temperature structure can be easily implemented by assigning a different temperature to each sub-layer. The thermal emission of the entire cloud layer can be obtained through the doubling process. However, the computational cost of the conventional doubling method is usually unaffordable for hyperspectral computations. To alleviate the

computational burden associated the doubling process, we assume that when the cloud optical thickness is smaller than some threshold value τ^* (by default set to 2^0 in FIRTM-AD) the effect of internal cloud temperature structure on the cloud thermal emission is insignificant. Under this assumption, the thermal emission of a cloud with optical thickness smaller than τ^* can be decomposed into two parts as follows:

$$\mathbf{E}(\tau,\langle\varpi\rangle,\langle P\rangle,T_{top},T_{bot}) \approx \boldsymbol{\varepsilon}[\tau,\langle\varpi\rangle,\langle P\rangle]B[(T_{top}+T_{bot})/2), \tag{2.4}$$

where T_{top} and T_{bot} are the cloud top and cloud bottom temperature, respectively. Based on the above assumption, a cloud with τ smaller than τ^* is treated as isothermal in FIRTM-AD and the corresponding thermal emission is obtained from Eq. (2.4) with a cloud emissivity of $\boldsymbol{\varepsilon}$ obtained from the LUT. If not explicitly specified otherwise by the user, a cloud with τ larger than τ^* is treated as non-isothermal in FIRTM-AD. To obtain the thermal emission, the cloud is first divided into sub-layers so that each sub-layer has an optical thickness of τ^* and only one sub-layer carries the residual. Note that all sub-layers are actually isothermal, but their temperatures are different from each other for simulating the temperature variation within the cloud. The temperature of each sub-layer is obtained from the user-specified temperature-optical thickness ($T(\tau)$) relationship for the cloud (by default a linear $T(\tau)$ is assumed). The emissivity $\boldsymbol{\varepsilon}_k$ of each sub-layer is obtained from the LUT and then the emission is obtained using Eq. (2.4). Finally, the thermal emission of the entire cloud layer is computed by doubling and adding the sub-layers. The threshold value, τ^*, determines the number of sub-

layers into which a given non-isothermal cloud is divided in FIRTM-AD, and therefore the efficiency and accuracy of FIRTM-AD in the computation of thermal emission from non-isothermal clouds. A large value of τ^* allows FIRTM-AD to avoid most of the doubling process and therefore makes the model computationally efficient, but on the other hand limits the ability of FIRTM-AD to describe the cloud temperature variation for a cloud layer having an optical thickness smaller than τ^*. In FIRTM-AD, τ^* is a user-definable parameter that can be changed to meet different requirements. Note that τ^* is set to 2^0 in the results shown later. As approximations to general and realistic conditions, both the "approximate scheme" for the cloud insertion and the treatment of the non-isothermal clouds are error sources in FIRTM-AD. The errors associated with these approximations will be assessed later in Section 2.5.

2.4. Development of the pre-computed look-up table for FIRTM-AD

As an essential part of FIRTM-AD, the pre-computed LUT is a set of databases containing the $\bar{\mathbf{R}}$, $\bar{\mathbf{T}}$ and $\boldsymbol{\varepsilon}$ of the retrieval object, such as ice clouds, water clouds and aerosol layers, in a discretized space of wavenumber (v), optical thickness (τ) and effective particle size (D_e). The coverage and the resolution of the LUT are highly application-oriented and should be determined according to the retrieval object, retrieval algorithm and required accuracy.

The FIRTM-AD presented in this study is developed primarily for the inference of ice cloud properties from hyperspectral IR observations. The

corresponding spectral coverage of the current LUT is from 800- to 1300 cm^{-1}. This atmospheric window region is chosen because of its importance in ice cloud property retrieval (Huang et al. 2004). A hyperspectral sensor may have hundreds of channels over this region. However, because cloud bulk scattering properties vary slowly with wavenumber compared with the absorption of the atmospheric gases, it is unnecessary to build a LUT at the spectral resolution of the sensor (Moncet and Clough 1997). Currently, only 39 spectral grid points from 800- to 1300 cm^{-1} are specified in the LUT.

The coverage over τ is currently chosen from 0.01 to 10, which corresponds to the sensitivity range of the IR sensors to the cloud optical thickness (Luo and Rossow 2004). Thirty values within this region are specified in the LUT. An important point to note is that the optical thickness in the database of FIRTM-AD, i.e., from 0.01 to 10, is referenced to the optical thickness of a cloud at a visible wavelength of 0.55 μm. The IR optical thickness of cloud, τ_v at a given wavenumber, v, can be written in terms of visible optical thickness, τ_{vis}, as follows:

$$\tau_v = \frac{\langle Q_e(v) \rangle}{\langle Q_e(0.55\mu m) \rangle} \tau_{vis}, \tag{2.5}$$

where $\langle Q_e \rangle$ is the bulk extinction efficiency (Baum et al. 2005a). In the current version of FIRTM-AD we assume that $\langle Q_e(0.55\mu m) \rangle$ is approximately 2.

The effective particle size, D_e, of an ice cloud is defined as follows (Baum et al. 2005a):

$$D_e = \frac{3}{2}\frac{\int_0^\infty \left(\sum_i V_i(D)w_i(D)\right)n(D)dD}{\int_0^\infty \left(\sum_i A_i(D)w_i(D)\right)n(D)dD}, \quad (2.6)$$

where D is the maximum dimension of an ice particle, V_i is the volume of the ice particle with a given shape (i.e., habit) indicated by the index *i*, A_i is the projected area of randomly oriented ice particle with the *i*th habit, w_i is the habit distribution and $n(D)$ is the particle size distribution (PSD). Based on the analysis of *in situ* observations of ice cloud PSDs obtained in focused field campaigns over past few decades, an extensive database for ice cloud bulk scattering properties has been developed by Baum et al. (Baum et al. 2007). This database contains the $\langle Q_e \rangle$, $\langle \varpi \rangle$ and $\langle P \rangle$ of various ice clouds with D_e from 10- to 180 μm over the spectral region from 100- to 3250 cm^{-1} with a resolution of 1 cm^{-1}. A similar approach was used to develop narrowband models that are currently being used for the moderate resolution imaging spectroradiometer (MODIS) operational ice cloud property retrieval. The D_e coverage of the LUT for FIRTM-AD is consistent with the above database, i.e. from 10- to 180μm with a resolution of 10μm.

Table 2.1 The quadrature points of 32-stream double-Gaussian quadrature over the upward hemisphere and the corresponding zenith angles**.**

#	Quadrature point	Zenith angle (degree)	#	Quadrature point	Zenith angle (degree)
1	0.0053	89.6964	9	0.5475	56.8039
2	0.0277	88.4120	10	0.6408	50.1484
3	0.0672	86.1477	11	0.7290	43.1967
4	0.1223	82.9753	12	0.8089	36.0077
5	0.1911	78.9852	13	0.8777	28.6336
6	0.2710	74.2767	14	0.9328	21.1219
7	0.3592	68.9490	15	0.9723	13.5202
8	0.4525	63.0962	16	0.9947	5.9013

At each grid point of the LUT, the dimension and nature of $\bar{\mathbf{R}}$, $\bar{\mathbf{T}}$ matrices and $\boldsymbol{\varepsilon}$ vectors are determined by the angular coordinate discretization scheme used for the adding-doubling implementation. In the current version of FIRTM-AD, the double-Gaussian quadrature described by Stamnes et al. (Stamnes et al. 1988) with 32 quadrature points, i.e. 32-stream (16 for the upward hemisphere and 16 for the downward hemisphere) is used for the coordinate discretization. The values of the quadrature points and corresponding zenith angles are listed in Table 2.1. Correspondingly, $\bar{\mathbf{R}}$ and $\bar{\mathbf{T}}$ are 16×16 matrices, whereas $\boldsymbol{\varepsilon}$ is a 16-element vector in the LUT. Note that the use of 8 or 16 streams would be accurate enough for most computations in the region from 800- to 1300 cm^{-1}. A relatively high order of the discrete ordinate approximation is used in the present study. It ensures the accuracy of the model in some extreme cases and, in addition, this 32-stream LUT can be used to generate the libraries where fewer streams are needed.

After the gird points specified and the angular discretization scheme chosen, the $\bar{\mathbf{R}}$, $\bar{\mathbf{T}}$ and $\boldsymbol{\varepsilon}$ on the grids of the LUT are computed using DISORT (Stamnes et al. 1988) with delta-M scaling (Wiscombe 1977b).The bulk scattering properties of ice clouds, i.e. $\langle Q_e \rangle$, $\langle \varpi \rangle$ and $\langle P \rangle$, are from Baum et al.'s database (Baum et al. 2007). Then, the $\bar{\mathbf{R}}$, $\bar{\mathbf{T}}$ and $\boldsymbol{\varepsilon}$ are organized into three binary databases that together form the LUT used in FIRTM-AD. To obtain the $\bar{\mathbf{R}}$, $\bar{\mathbf{T}}$ and $\boldsymbol{\varepsilon}$ of clouds that are not specified in the LUT, interpolation is required. For simplicity and computational efficiency, a linear interpolation scheme is used in FIRTM-AD for all cloud radiative properties.

2.5. Accuracy estimation of FIRTM-AD

In this section, we assess the accuracy of FIRTM-AD in the computation of high-spectral-resolution (0.1 cm^{-1}) BT spectra at both the surface and TOA for various cloud and viewing geometry conditions. The accuracy is estimated by comparing the simulations from FIRTM-AD with those from the DISORT model under the same conditions.

Before proceeding to detailed error analyses, it is helpful to first have an overview of the differences between DISORT and FIRTM-AD in the model configurations for the following simulations. For the cloud realization, the "coexisting scheme" is used in DISORT whereas the "approximate scheme" is used in FIRTM-AD. As discussed in Section 2.3, the ability of FIRTM-AD in the implementation of non-isothermal clouds is limited by the threshold value τ^*. In

DISORT, cloud bulk radiative properties, i.e. eigenvalues and eigenvectors (Stamnes et al. 1988), are computed at every spectral point specified by the given spectral (800- to 1300 cm^{-1}) region and resolution (0.1 cm^{-1}). In FIRTM-AD, cloud bulk radiative properties, i.e. $\bar{\mathbf{R}}$, $\bar{\mathbf{T}}$ and $\boldsymbol{\varepsilon}$, are computed only at 39 selected spectral points in the LUT. The properties at other points are interpolated from the computed ones. In both DISORT and FIRTM-AD, the 32-stream double-Gaussian quadrature is used for the discretization of angular coordinate. Note that the errors of DISORT in the interpolation of radiances from the model angles to the user-specified angles are negligible due to the use of a relatively high order of the discrete-ordinate approximation (32-stream). Therefore, based on the above comparisons, if DISORT is taken as the benchmark model, the errors in FIRTM-AD arise primarily from four major sources: 1) the error caused by using the cloud realization scheme discussed in Section 2.2 to approximate the non-isothermal and gas-cloud coexisting layer (hereafter referred to as the "cloud-realization error"); 2) the error caused by the interpolation of $\bar{\mathbf{R}}$, $\bar{\mathbf{T}}$ and $\boldsymbol{\varepsilon}$ over wavenumber v (hereafter referred to as the "v-interpolation error"); 3) the error caused by the interpolation of $\bar{\mathbf{R}}$, $\bar{\mathbf{T}}$ and $\boldsymbol{\varepsilon}$ over τ (hereafter referred to as the "τ-interpolation error"); 4) the error caused by the interpolation of radiances from the model angles specified by the angular discretization scheme to the user-specified angles (hereafter referred to as the "μ-interpolation error"). As a reminder, the scheme currently used in FIRTM-AD for the interpolation of radiances from model angles to the user-specified angle is described in Appendix B. Note that the relative importance of above four error

sources is different under different cloud and viewing conditions. As a result, the accuracy of FIRTM-AD is sensitive to both the cloud conditions and the sensor viewing angles. Because of the endless possibilities of these conditions in addition to the high computational cost of using DISORT to simulate the hyperspectral BT spectrum, a “complete” error analysis for FIRTM-AD is not provided. The strategy for the present accuracy estimation is to set up both “good” and “bad” scenarios, in terms of the number of error sources involving in FIRTM-AD, so that the relative importance of error sources can be estimated through comparisons between scenarios. In this fashion, the overall error level of FIRTM-AD can be estimated from the “bad” scenarios in which all error sources are considered.

In the present accuracy estimation the following two standards are used. The errors of FIRTM1 and FIRTM2, in terms of the root-mean-square (RMS) BT errors, for BT spectrum computations at TOA are on the order of 0.5 K over the spectral region 800- to 1300 cm^{-1} (Niu et al. 2007; Wei et al. 2004). As a more comprehensive and rigorous model, FIRTM-AD should have an error level lower than 0.5 K. The sensitivity of the hyperspectral sensors, to which the FIRTM-AD could be potentially applied, can also be used as the standard for accuracy estimation. The NEdT (Noise Equivalent Differential Temperature) of current hyperspectral sounders, such as AIRS and IASI, are at the level of 0.2 K (Blumstein et al. 2004; Gaiser et al. 2003). In our view, an acceptable error level for FIRTM-AD would be a value at or lower than the NEdT of above sensors (i.e., 0.2 K).

A tropical atmosphere is used in the present simulations with FIRTM-AD and DISORT. The atmosphere column from the surface to a height of 100 km above the surface is divided into 100 layers. The physical thickness of each layer varies from 0.5 to 2.5 km. The optical thickness of each layer due to the absorption of the atmospheric gases is obtained from the line-by-line radiative

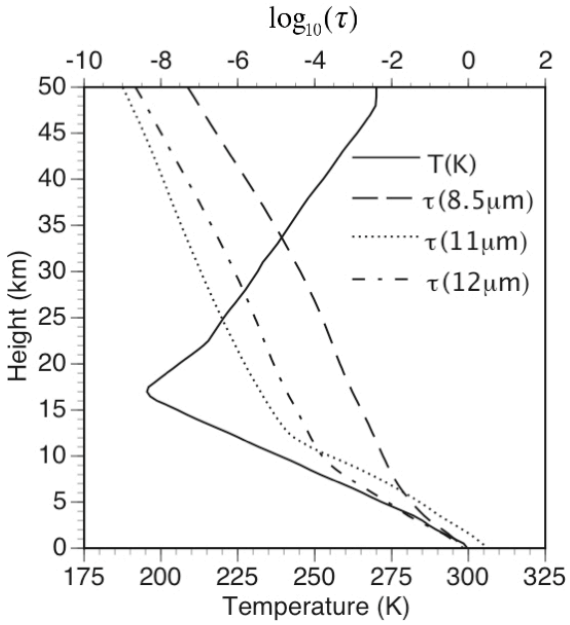

Figure 2.3 Temperature profile and the optical depth profiles at 8.5-, 11- and 12 μm of the background atmosphere used in the computations.

transfer model (LBLRTM) (Clough et al. 1992) with a resolution of 0.1 cm^{-1}. The temperature profile and optical depth profile at 1176.5 cm^{-1} (8.5 μm), 909.1 cm^{-1} (11 μm) and 833.3 cm^{-1} (12 μm) of this atmosphere are shown in Fig. 2.3. The planetary surface is assumed to be Lambertian. The surface temperature T_s is assumed as 299.7 K. Additionally, a surface albedo of $\alpha_s = 0.03$ is assumed regardless of wavenumber.

Figure 2.4 shows the results from application of FIRTM-AD to the computation of high-spectral-resolution (0.1 cm^{-1}) BT spectra at TOA under single-layered cloud conditions. In this case, a cirrus cloud is located between 13.5 and 14.0 km above the surface. The cloud top and base temperatures are, respectively, 211.75 and 215.25 K. Figure 2.4a shows BT spectra simulated from FIRTM-AD for various combinations of cloud visible optical thicknesses, τ_{vis}, (0.10, 0.55 and 0.95) and satellite viewing angles, θ_v, (5.9^0 and 45^0) while the effective particle size, D_e, is assumed as 30 μm in all simulations. Figure 2.4c shows the BT spectra from FIRTM-AD for various combinations of D_e (20-, 40-

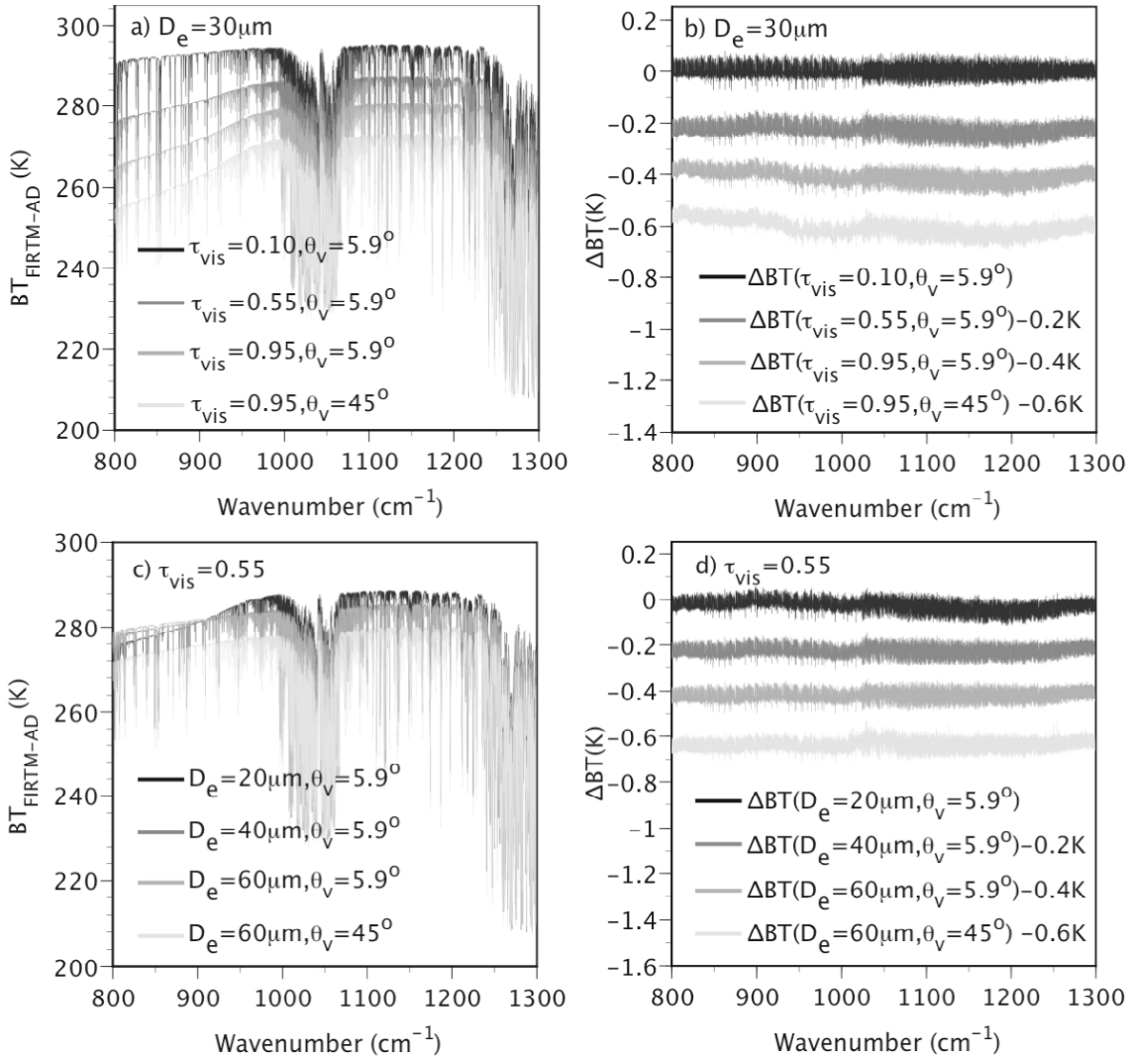

Figure 2.4. Application of FIRTM-AD to hyperspectral BT computations at TOA for single-layered clouds. (a) BT spectra at TOA from FIRTM-AD for various combinations of cloud visible optical thicknesses, τ_{vis}, and viewing angles, θ_v, while the cloud particle effective size, D_e, is 30 μm in all scenarios. (b) The differences in BT spectra between FIRTM-AD and DISORT ($\Delta BT = BT_{FIRTM-AD} - BT_{DISORT}$) in the scenarios shown in (a). (c) BT spectra at TOA from FIRTM-AD for various combinations of D_e and θ_v, while $\tau_{vis} = 0.55$ in all scenarios. (d) ΔBT spectra corresponding to the scenarios shown in (c). The RMS values of the ΔBT spectra in (b) and (d) are listed in Table 2.2.

and 60 μm) and θ_v (5.9^0 and 45^0) while τ_{vis} is assumed as 0.55 in all simulations. The above combinations of τ_{vis}, D_e and θ_v are chosen so that both "good" and "bad" scenarios are included in Fig. 2.4. For example, the scenario where $\tau_{vis} = 0.1$ and $\theta_v = 5.9^0$ is a "good" scenario in comparison with the one where $\tau_{vis} = 0.55$ and $\theta_v = 45^0$. This is because $\tau_{vis} = 0.1$ is on the grid of τ_{vis}-space of the LUT, while $\tau_{vis} = 0.55$ is not, and $\theta_v = 5.9^0$ is a model angle, while $\theta_v = 45^0$ is not (see Table 2.1). As a result, no interpolation over τ_{vis} or θ_v is needed in FIRTM-AD for the former scenario but both are necessary for the latter. The BT spectra in Fig. 2.4a and 2.4c show considerable sensitivity to both τ_{vis} and D_e. These sensitivities have been used to infer the optical properties of thin cirrus clouds using the hyperspectral observations from AIRS (Li et al. 2005a; Wei et al. 2004). The differences in the BT spectra ($\Delta\mathrm{BT}$ spectra) between FIRTM-AD and DISORT in the scenarios in Figs. 2.4a and 2.4c are shown, respectively, in Figs. 2.4b and 2.4d. $\Delta\mathrm{BT}$ is defined as follows:

$$\Delta\mathrm{BT}=\mathrm{BT}_{\mathrm{FIRTM\text{-}AD}} - \mathrm{BT}_{\mathrm{DISORT}}. \tag{2.7}$$

The RMS value of the $\Delta\mathrm{BT}$ spectrum is used as an index for the overall error level of FIRTM-AD following previous studies (Li et al. 2005a; Wei et al. 2004). The RMS value is defined as:

$$\mathrm{RMS}(\Delta\mathrm{BT})=\sqrt{\frac{\sum_{i}^{N_p}\left(\Delta\mathrm{BT}_i\right)^2}{N_p}}, \tag{2.8}$$

where N_p is the number of spectral points in the spectrum and $\Delta \mathrm{BT}_i$ is the difference of BT between FIRTM-AD and DISORT at the i^{th} spectral point. The RMS values of each $\Delta \mathrm{BT}$ spectrum in Figs. 2.4b and 2.4d are listed in Table 2.2.

Table 2.2 The RMS BT errors of FIRTM-AD with respect to DISORT under the single-layered cloud conditions in the scenarios shown in Fig. 2.4. and the major error sources present in each scenario.

Scenario #	τ_{vis}	D_e (μm)	θ_v (degree)	Error sources*	RMS of $\Delta \mathrm{BT}$ (K)
1	0.10	30	5.9	1), 2)	0.0306
2	0.55	30	5.9	1), 2), 3)	0.0426
3	0.95	30	5.9	1), 2), 3)	0.0334
4	0.95	30	45.0	1), 2), 3), 4)	0.0365
5	0.55	20	5.9	1), 2), 3)	0.0448
6	0.55	40	5.9	1), 2), 3)	0.0422
7	0.55	60	5.9	1), 2), 3)	0.0372
8	0.55	60	45.0	1), 2), 3), 4)	0.0498

* 1) cloud realization error; 2) v-interpolation error; 3) τ-interpolation error ; 4) μ-interpolation error

The featureless $\Delta \mathrm{BT}$ spectra in Fig. 2.4b and 2.4d indicate that the errors of FIRTM-AD are spectrally uncorrelated. The $\Delta \mathrm{BT}$ spectra in Fig. 2.4d are almost identical to each other, revealing that the errors are independent of D_e. As shown in Table 2.2, the largest error, 0.0498 K, occurs in a “bad” scenario (scenario #8 in Table 2.2) where $\tau_{vis} = 0.55$, $D_e = 60$ μm and $\theta_v = 45^0$. It is interesting to note that the error in the other “bad” scenario (scenario #4 in Table 2.2) where $\tau_{vis} = 0.95$, $D_e = 30$ μm and $\theta_v = 45^0$, is only 0.0334 K. This is reasonable and can be explained as follows: because the τ_{vis}-interpolation uses

the adjacent points in the LUT, the relative errors of interpolation are similar at $\tau_{vis} = 0.55$ and $\tau_{vis} = 0.95$. However, because the absolute value of the transmissivity of the former is larger than the latter, the absolute error of τ_{vis}-interpolation in the former scenario is larger than the latter leading to the results in Table 2.2. Overall, it is evident from Fig. 2.4 and Table 2.2 that the accuracy of FIRTM-AD in the computations of BT spectra for optically thin single-layered cirrus cloud is very good. The error of FIRTM-AD in this type of application is an order of magnitude smaller than that of FIRTM1 and FIRTM2, and also well below the NEdT of the current advanced hyperspectral sensors.

In addition to the satellite-based hyperspectral sensors, the ground-based hyperspectral sensors, such as the AERI, are also important application areas for FIRTM-AD. Figure 2.5 shows the application of FIRTM-AD to the computations of BT spectra corresponding to the downwelling radiances at the surface. The cloud configurations for the results shown in Fig. 2.5 are the same as those in Fig.2.4. Figure. 2.5a shows the BT spectra computed from FIRTM-AD for various combinations of τ_{vis} and θ_v. The corresponding $\Delta\mathrm{BT}$ spectra are shown in Fig. 2.5b. The BT spectra for various combinations of D_e and θ_v are shown in Fig. 2.5c with corresponding $\Delta\mathrm{BT}$ spectra shown in Fig. 2.5d. Note that a negative viewing angle indicates the viewing direction is upward at the surface; the absolute value of the angle corresponds to the angle between the nadir and viewing direction. The RMS BT errors of FIRTM-AD in all scenarios, as shown in Fig. 2.5b and 2.5d, are quite featureless. The RMS values of $\Delta\mathrm{BT}$ in all scenarios are smaller than 0.03K.

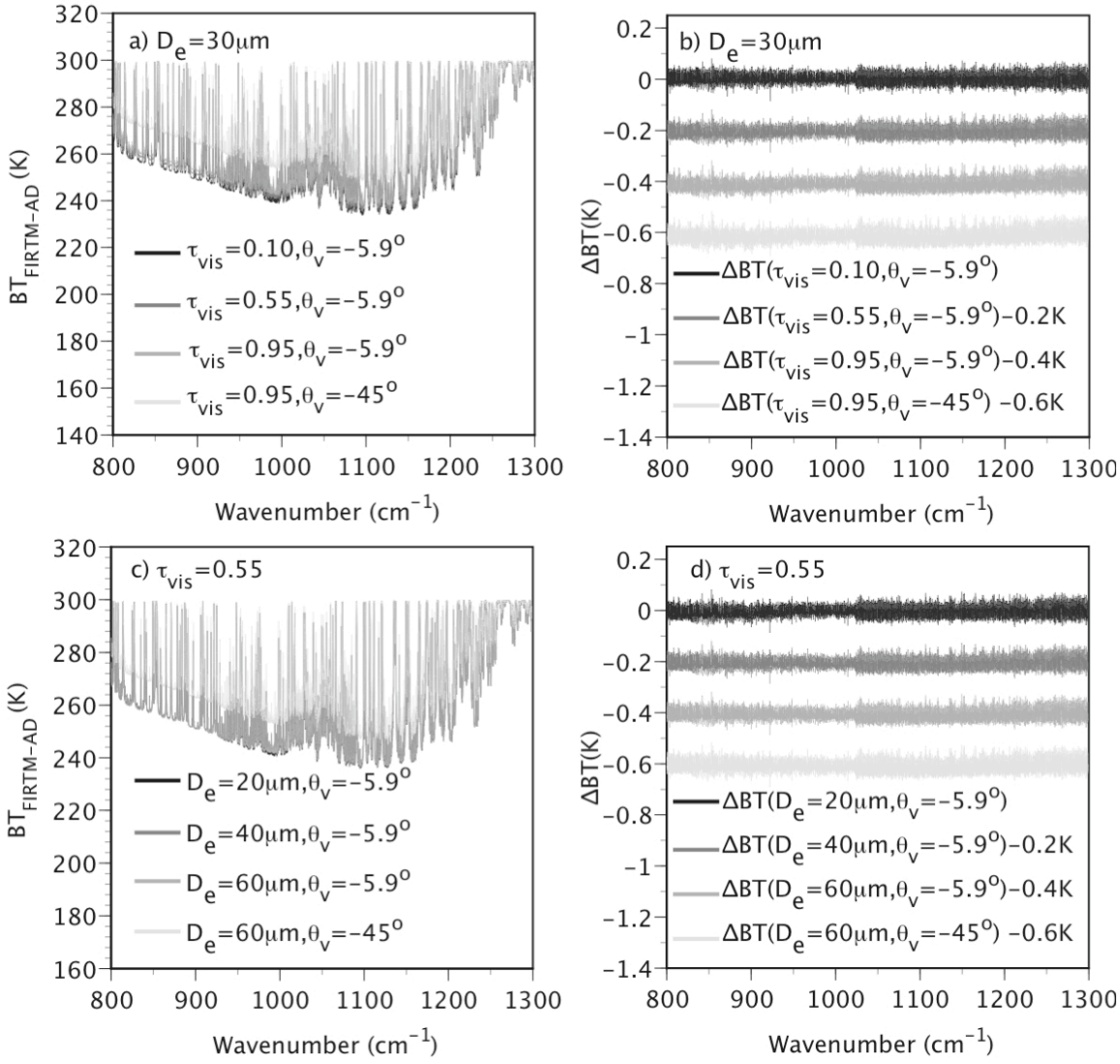

Figure 2.5 Application of FIRTM-AD to hyperspectral BT computations at the surface for single-layered cloud conditions. (a) BT spectra at the surface from FIRTM-AD for various combinations of τ_{vis} and θ_v, while $D_e = 30\ \mu m$. (b) $\Delta\mathrm{BT}$ spectra corresponding to the scenarios shown in (a). (c) BT spectra at the surface from FIRTM-AD for various combinations of D_e and θ_v, while $\tau_{vis} = 0.55$ in all scenarios. (d) $\Delta\mathrm{BT}$ spectra corresponding to the scenarios shown in (c).

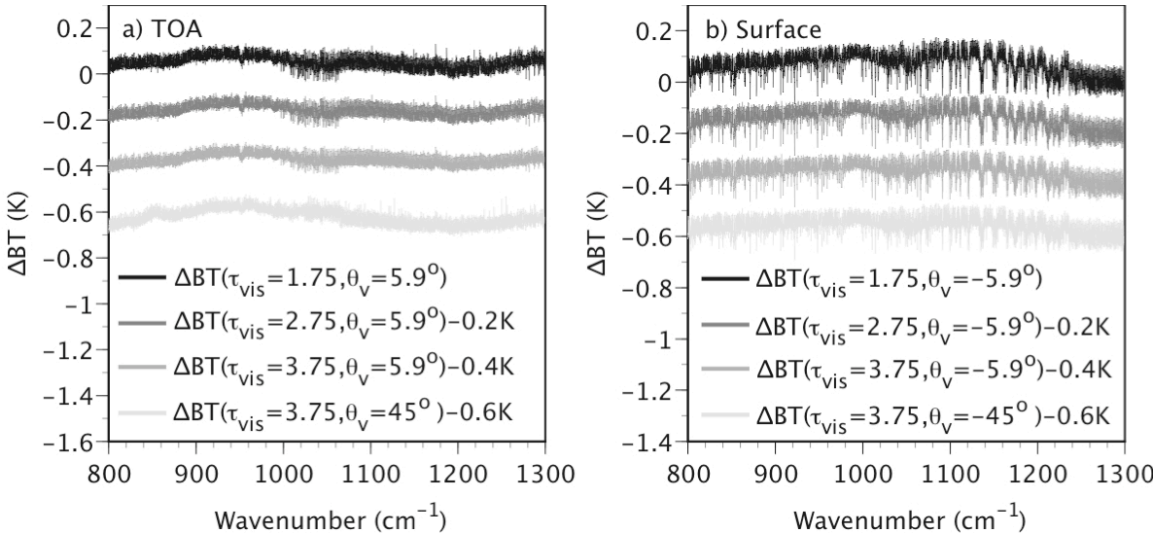

Figure 2.6 The errors of FIRTM-AD in hyperspectral BT computations for a two-layered cirrus cloud. The τ_{vis} and D_e of the upper cirrus layer are, respectively, 1.25 and 30 μm. The D_e of the lower cirrus layer is 100 μm. (a) $\Delta\mathrm{BT}$ spectra at TOA for various combinations of lower cirrus layer τ_{vis} and θ_v values. (b) $\Delta\mathrm{BT}$ spectra for various combinations of lower cirrus layer τ_{vis} and θ_v. The RMS values of $\Delta\mathrm{BT}$ are listed in Table 2.3.

Figure 2.6 shows the errors of FIRTM-AD for a two-layered cirrus cloud case. The upper layer is located in a layer from 11.5 to 12 km above the surface with a cloud top and base temperature of 225.5 and 228.5 K, respectively. The τ_{vis} and D_e of the upper layer are assumed as 1.25 and 30 μm, respectively. The lower cirrus layer is located at 11 to 11.5 km with a top and base temperature of 228.5 and 231.75 K, respectively. Because Figs. 2.4 and 2.5 reveal that the accuracy of FIRTM-AD has little dependence on D_e, only a single effective particle size, D_e=100 μm, is assumed for the lower layer. Figure 2.6a shows the

differences between FIRTM-AD and DISORT in simulating the BT spectra at TOA, i.e. the ΔBT spectra at TOA, under various combinations of lower layer τ_{vis} (1.75, 2.75, 3.75) and downward viewing angles, θ_v (5.9^0 and 45^0). The ΔBT spectra at the surface under various combinations of lower layer τ_{vis} and upward viewing angles (-5.9^0 and -45^0) are shown in Fig 2.6b.The RMS values of each ΔBT spectrum in Fig. 2.6 and the major error sources in each scenario are listed in Table 2.3. In comparison with the single-layered cloud case, the errors of FIRTM-AD applied to two-layered cloud are slightly larger (the largest error is about 0.06 K in the scenario #1 in Table 2.3). A small warm bias, which is caused by the use of the approximate cloud realization scheme described in Section 2.3

Table 2.3 The RMS BT errors of FIRTM-AD with respect to DISORT under the two-layered cloud condition in the scenarios shown in Fig. 2.6 and the corresponding major error sources.

Scenario #	τ_{vis}	D_e (μm)	θ_v (degree)	Error sources	RMS of ΔBT (K)
1	1.75	100	5.9	1), 2), 3)	0.0583
2	2.75	100	5.9	1), 2), 3)	0.0490
3	3.75	100	5.9	1), 2), 3)	0.0379
4	3.75	100	45.0	1), 2), 3), 4)	0.0419
5	1.75	100	-5.9	1), 2), 3)	0.0530
6	2.75	100	-5.9	1), 2), 3)	0.0627
7	3.75	100	-5.9	1), 2), 3)	0.0716
8	3.75	100	-45.0	1), 2), 3), 4)	0.0812

to treat the non-isothermal clouds, is observed in Fig. 2.6b indicating that that FIRTM-AD tends to slightly overestimate the downwelling radiances at the

surface. However, despite the bias, the largest error of FIRTM-AD in Fig. 2.6b (scenario #8 in Table 2.3) is still substantially smaller than 0.2 K.

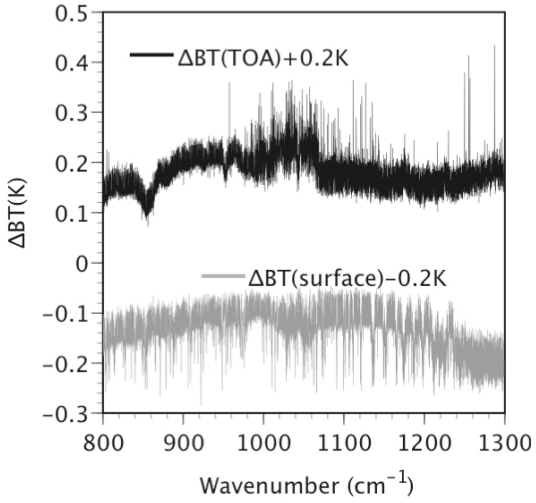

Figure 2.7 The errors of FIRTM-AD for a case where there are three layers of cirrus cloud in the atmosphere shown in Fig. 2.3. The black line corresponds to the $\Delta\mathrm{BT}$ spectrum at TOA (downward nadir-viewing) with the values shifted upward by 0.2 K. The gray line corresponds to the $\Delta\mathrm{BT}$ spectrum at the surface (upward nadir-viewing) with the values shifted downward by 0.2 K.

Figure 2.7 shows the errors of FIRTM-AD in the computation of nadir-viewing BT spectra for a case where there is a multilayered (three-layered) cirrus cloud in a tropical atmosphere. The uppermost cirrus layer is located between 13.5 to 14.0 km with τ_{vis} and D_e of 0.25 and 30 μm, respectively. The middle and lower layers are located, respectively, at 11.5 to 12 km and 11.0 to 11.5 km. The τ_{vis} and D_e of the middle layer are 1.25 and 60 μm, respectively. The corresponding values for the lower layer are 1.75 and 100 μm, respectively. The

RMS values of ΔBT spectra at TOA and surface are 0.0439 K and 0.072 K, respectively.

2.6. Discussion and summary

The computational efficiency of FIRTM-AD depends on the optical thickness and extent of inhomogeneity of cloud layers. As mentioned in Section 3, the efficiency of FIRTM-AD is also affected by the value of τ^*. Based on the timing of the computations in above error analyses, the computational efficiency of FIRTM-AD when τ^* is set to 2^0 under the single, double and multilayered cloud conditions is listed in Table 2.4 along with that of DISORT under the same conditions. For the type of computations in Figs. 2.4 and 2.5, the FIRTM-AD is approximately 250 times faster than DISORT. Under three-layered cloud

Table 2.4[*] The computational efficiencies (in seconds per 100 wavenumbers) of FIRTM-AD and DISORT under the same conditions on an Apple 1.8GHz G5 computer**.**

Cloud conditions	DISORT (32-stream)	FIRTM-AD (32-stream)
Single-layered (Figs. 2.4 and 2.5)	53.775	0.231
Two-layered[**] (Fig. 2.6)	56.342	0.434
Three-layered (Fig. 2.7)	57.012	0.526

* In FIRTM-AD, τ^* is set to 2^0 in all simulations.
** τ_{vis} of the lower layer is 3.75.

conditions as in Fig. 2.6, FIRTM-AD is still more than two orders of magnitude faster than DISORT. Given that the instrument noise level of current hyperspectral sensors, such as AIRS and IASI, is about 0.2 K, the RMS errors of FIRTM-AD for the cases shown in the previous section are quite acceptable. However, there are endless combinations of potential cloud and viewing conditions and therefore it is almost certain that the errors of FIRTM-AD will exceed 0.1 K in some extreme cases. Given the algorithms used in the formulation of FIRTM-AD, it is unlikely that the accuracy of FIRTM-AD will substantially degrade in those cases. We believe that the errors of the FIRTM-AD in those cases are unlikely to exceed those of FIRTM1 and FIRTM2. Also, it is necessary to point out that in above simulations the solar contribution has been ignored in both FIRTM-AD and DISORT. Future work is planed to investigate the impact of this omission under different cloud conditions and sun-satellite angles.

It is worth noting that FIRTM-AD is applicable not only to the hyperspectral sensors, but also to the narrowband sensors in the thermal IR spectral region. For the remote sensing of cloud properties using bispectral narrowband satellite measurements in the thermal IR region (e.g., 8~12 μm), which is independent of solar illumination, the cloud signatures in the atmospheric window region are often used to derive their properties. Figure 2.8 shows an example of the LUT generated using one channel at 11 μm (a bandwidth, 10.78~11.28 μm, corresponding to MODIS channel #31 is assumed) and the other channel at 12 μm (a bandwidth, 11.77~12.27 μm, corresponding to MODIS channel #32 is assumed). This kind of LUT has been used to retrieve the cloud thermodynamic

phase (Baum et al. 2000) and is also potentially useful for the inference of τ_{vis} and D_e of ice clouds at night. As shown in Fig. 2.8, one dimension of the table is the BT at 11 μm and the other is the difference in BT between 11 and 12 μm. Each point in the table corresponds to an ice cloud with a unique combination of τ_{vis} and D_e. Along each solid line, from right to left, the D_e of the cloud remains constant while τ_{vis} increases. Along each dashed line, from top to bottom, the τ_{vis} remains constant while the D_e increases. This feature of the table has made it possible to infer τ_{vis} and D_e by projecting the instrument measurements onto the table.

An important point to note is that this kind of LUT depends on the atmospheric profile and therefore must be renewed often because the temperature and water vapor profiles can change from one footprint to another. Moreover, for each footprint the RT model has to be run dozens of times to generate a LUT as shown in Fig. 2.8. Consequently, a practical implementation of this approach requires computationally efficient RT models, which makes the generation of these LUTs a useful application for FIRTM-AD. The asterisk points in Fig. 2.8 are obtained with DISORT and the points marked as circles are results from FIRTM-AD. In the simulations, the tropical atmosphere shown in Fig. 2.3 is used. The optical thickness profile of the background atmosphere is obtained from the correlated k-distribution model developed by Kratz (Kratz 1995).It is seen from the figure that the two groups of points completely overlap, indicating the equivalence of the two models in terms of the accuracy for this retrieval

algorithm. However, the CPU requirements with FIRTM-AD are much less than with DISORT.

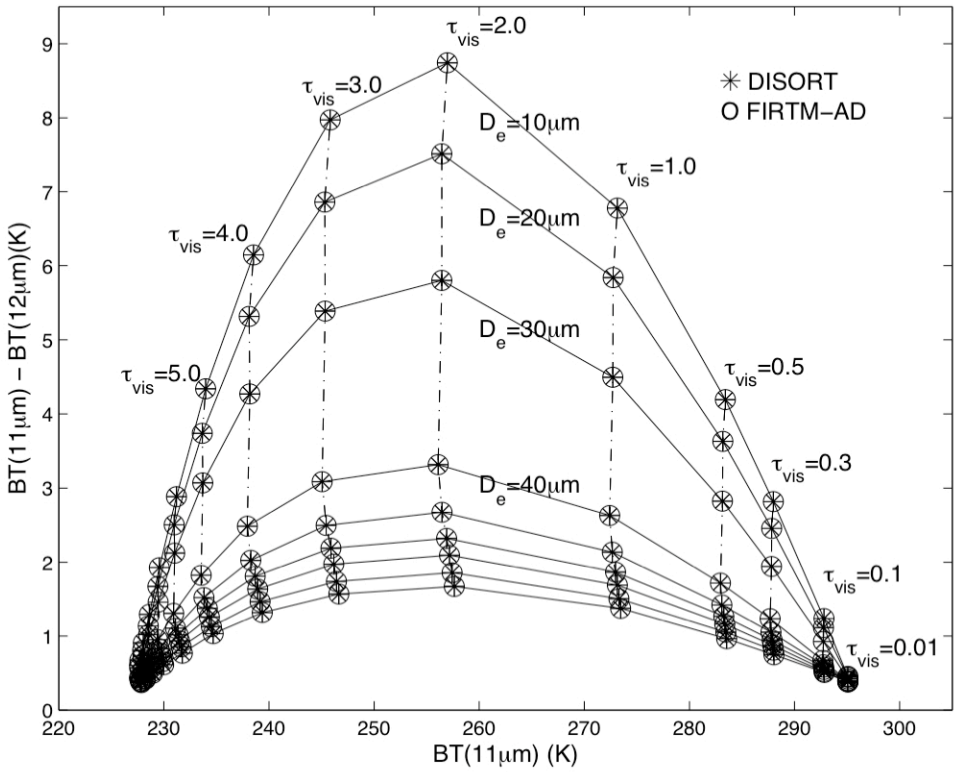

Figure 2.8 A look-up table for the cloud property retrieval using 11- and 12 μm channels. Along each solid line, from right to left, the optical thickness of the cloud increases while the effective size remains constant. Along each dashed line, from top to bottom, the effective size of the cloud increases while the optical thickness remains constant. The asterisks are results from DISORT and the circles are from FIRTM-AD.

In summary, based on the advantages of CHARTS, FIRTM1 and FIRTM2, we have developed a fast IR RT model based on the well-known adding-doubling principle for applications to the forward RT simulations involved in the hyperspectral remote sensing applications under cloudy-sky conditions. Because of the use of the pre-computed LUT, the computational burden associated with the doubling process is substantially alleviated in FIRTM-AD. In comparison with FIRTM1 and FIRTM2, FIRTM-AD is much more flexible and accurate. FIRTM-AD is applicable to multilayered, inhomogeneous and non-isothermal clouds. In addition, FIRTM-AD can be applied to computations at both TOA and the surface, and therefore applicable to both satellite and ground-based hyperspectral sensors. The comparisons have shown that FIRTM-AD is about 250 times faster than DISORT in the computations of BT spectra at TOA and the surface for a single-layered thin ($\tau_{vis} < 1$) cirrus cloud. The RMS BT errors of FIRTM-AD in this type of application are generally smaller than 0.05 K. For two or three-layered thick ($\tau_{vis} > 1$) cloud conditions, FIRTM-AD is still about two orders of magnitude more efficient than DISORT and the error is on the order of 0.1 K.

Finally, it is worth mentioning a limitation of FIRTM-AD. That is, currently, FIRTM-AD is only suitable for forward calculations and cannot be applied to Jacobian calculations. The usefulness of the Jacobians in atmospheric soundings, cloud property retrievals and data assimilations has been demonstrated by numerous studies (Rodgers 2000 and ref. within). However, adjoint model is required for Jacobian calculations. One of the future directions is

to develop the adjoint model for FIRTM-AD on the basis of the radiative perturbation theory briefly introduced in Appendix C.

III. AN INVESTIGATION OF THE OPTICAL PROPERTIES OF QUASI-SPHERICAL ICE PARTICLES: IMPLICATIONS FOR MEASURING ICE PARTICLE SIZE WITH FSSP-TYPE INSTRUMENTS

3.1. Background

Currently, one of the biggest uncertainties in modeling the radiative properties of cirrus clouds is associated with the small ice particles with sizes smaller than about 50 μm in cirrus clouds (McFarquhar et al. 2007). In situ measurements show that these small ice particles are irregular and often have aspect ratios close to unity (e.g., Gayet et al. 1996b; Nousiainen and McFarquhar 2004; Garrett et al. 2003). For this reason, they are often referred to as the "quasi-spherical" ice particles. Because of our inadequate knowledge, the concentration, microphysical and optical properties of these ice particles and consequently their importance have all been controversial issues. Some studies have suggested that in the tops of high (13-18km) and cold (-60 to -90 ^{o}C) tropical cirrus clouds, ice particles with sizes about 20-40 μm dominate the particle size distribution and play an dominant role in determining the radiative properties, such as the shortwave cloud albedo, of cirrus clouds (Knollenberg et al. 1993; Zender and Kiehl 1994). Some studies, on the other hand, have not attributed the same importance to small ice particles. For instance, Heymsfield and McFarquhar (Heymsfield and McFarquhar 1996) showed that large ice particles play an equivalently important role in determining the cloud radiative

properties. Similar results were also reached by some other studies (e.g., McFarquhar and Heymsfield 1997).

An important reason responsible for the divergent view the importance of small ice particles is related to the dubious reliability of conventional cloud particle probes, namely, the Forward Scattering Spectrometer Probe (FSSP, Knollenberg 1981), for measuring the size and extinction cross-section of small ice particles. It is known that FSSP-type probes tend to overestimate the number concentration of small ice particles, in some cases by a factor of 5, because of the shattering of large ice particles at the probe's inlet (e.g., Field et al. 2003; Field et al. 2006).

However, of particular interest here is another important uncertainty. That is, whether the assumption of sphericity for small ice particles may lead to serious underestimation of their sizes and, more importantly, extinction cross-sections. As will be described in details in section 3.3, to derive the size and extinction cross-section of observed ice particles from FSSP measurements, some ice particle shapes must be preassumed. Because the aspect ratios of small ice particles are often close to unity, they are often empirically assumed to be ice spheres (Heymsfield et al. 2006). The uncertainty caused by this assumption has received increasing attentions due to a recent debate (Garrett et al. 2003; Heymsfield et al. 2006; Garrett 2007; Heymsfield et al. 2007). It is reported in Heymsfield et al. (Heymsfield et al. 2006) that cloud extinction derived from FSSP measurements is smaller than the "direct" measurement from the cloud-integrating nephelometer (CIN, Gerber et al. 2000), by a factor of 2 to 2.5.

Garrett (Garrett 2007) argued, in his comments on Heymsfield et al. (Heymsfield et al. 2006), that the difference should be attributed to the underestimation of small ice particles' extinction cross-section by FSSP. He further suspected that the assumption that small ice particles are spheres might have led to the underestimation. On the other hand, in his reply to Garrett (Garrett 2007), Heymsfield et al. (Heymsfield et al. 2007) argued that the difference of cloud extinction measurements between FSSP and CIN should be attributed to the overestimation of CIN caused by the aforementioned shattering effect.

It is worth mentioning that one of the widely used methods for obtaining the effective radius (r_e) of cirrus cloud is based on the following equation (Heymsfield et al. 2006):

$$r_e = \frac{3IWC}{2\rho_{ice}\beta_e}, \tag{3.1}$$

where IWC denotes ice water content measurement, ρ_{ice} is the density of ice and β_e is the extinction coefficient, which is usually derived from the total extinction cross-section measurement from FSSP. Note that in the above equation, the extinction efficiency, i.e., Q_e, of ice particles are taken to be a constant of 2. Evidently from Eq. (3.1), uncertainty in cloud extinction measurement may also affect effective radius estimation.

As indicated above, the uncertainties in FSSP measurement are of great impotence. Clarification of the uncertainties may help to improve our understanding the importance of small ice particles in determining the radiative properties of cirrus clouds. Motivated by these considerations, in this part of the

study we investigate whether and why the assumption of sphericity for small ice particle may lead to serious errors in the FSSP measurement of the extinction of small ice particles.

Specifically, the investigation consists of two parts. In the first part, the optical properties of Platonic solids (i.e., icosahedron, dodecahedron, octahedron, hexahedron or cube, and tetrahedron) will be computed using a numerical scattering model based on the geometrical-optic method and compared to those of equivalent ice spheres. The Platonic solids are particularly interested here because they are all quasi-spherical and therefore represent the nature of small ice particles in cirrus clouds. Moreover, Platonic solids deviate from a sphere in an ordered manner in terms of their extents of asphericity, which makes the comparison of their optical properties with those of equivalent spheres particularly intriguing. In the second part, the implications of the results from the first part for measuring ice particle size and extinction cross-section with FSSP-type probes will be discussed.

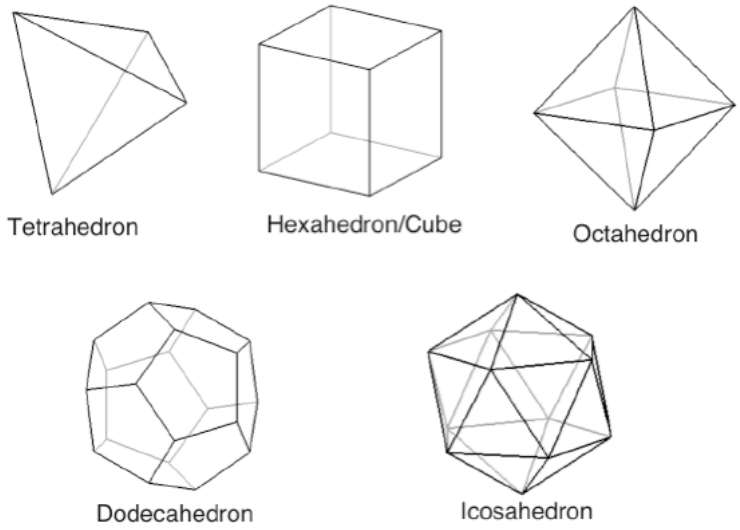

Figure 3.1 Geometries of the Platonic solids, i.e. the tetrahedron, hexahedron (or cube), octahedron, dodecahedron and icosahedron.

3.2. Optical properties of Platonic solids

3.2.1. Geometries of Platonic solids

The Platonic solids (Cromwell 1997), also known as regular solids or polyhedra, are five regular convex polyhedra including tetrahedron, hexahedron, octahedron, dodecahedron and icosahedron that have 4, 6, 8, 12 and 20 faces, respectively. Figure 3.1 shows the geometries of the Platonic solids.

There are a number of ways to quantitatively define the extent of asphericity of a particle. One approach is to use the ratio (δ_V) of the volume of a particle to that of the corresponding circumscribing sphere. Obviously, this ratio is always smaller than unity for a nonspherical particle, and the extent of asphericity decreases with the decrease of δ_V. With this definition of asphericity, the tetrahedron among all the Platonic solids has the maximum asphericity whereas the dodecahedron has the minimum asphericity. Alternatively, the asphericity of a

particle can also be defined in terms of the ratio (δ_S) of the surface area of this particle to that of the corresponding circumscribing sphere. For convex nonspherical particles such as one of the Platonic solids, δ_S is always smaller than unity and inversely proportional to the extent of asphericity. However, such a definition is less obvious and sometimes may be misleading in the case of nonconvex particle, because the surface area of a nonconvex particle may not be necessarily smaller than that of its circumscribing sphere. However, this is not an issue for the present study, as the Platonic solids are nonconvex. The volume-to-surface area ratio ($\delta_{V/S}$) is another measure of the asphericity of a nonspherical particle. Because a sphere has the minimum surface area for a given volume, the quantity $\delta_{V/S}$ for a sphere is always larger than that of a nonspherical particle if the two geometries have the same volume or surface area. Note that $\delta_{V/S}$ is a function of particle size. However, the dependence of $\delta_{V/S}$ on particle size can be eliminated by normalizing $\delta_{V/S}$ with respect to the radius of the circumscribing sphere of a nonspherical particle, i.e. $\delta'_{V/S} = 3\delta_{V/S} / R$, where the constant 3 ensures that $\delta'_{V/S}$ is equal to unity for spheres. The values for δ_V, δ_S and $\delta'_{V/S}$ of the Platonic solids are shown in Table 3.1. Evidently, in terms of either δ_V or δ_S, the asphericity extents of the Platonic solids are ranked in the same order: tetrahedron, octahedron, cube, icosahedron, and dodecahedron. However, in terms of $\delta'_{V/S}$, the cube and octahedron have the same extent of asphericity, and so do the icosahedron and dodecahedron.

Table 3.1 Values of δ_V , δ_S and $\delta'_{V/S}$ of Platonic solids

Platonic solid	δ_V	δ_S	$\delta'_{V/S}$
Tetrahedron	0.1225	0.3676	0.3333
Octahedron	0.3183	0.5513	0.5774
Hexahedron (Cube)	0.3676	0.6366	0.5774
Icosahedron	0.6055	0.7619	0.7947
Dodecahedron	0.6649	0.8367	0.7947

To study the scattering properties of the equivalent sphere for a Platonic solid, we define the radius of the equivalent sphere in the same way as in Yang et al. (Yang et al. 2004) in four different ways as follows:

$$r = R, \tag{3.2}$$

$$r = R_a = (S / 4\pi)^{1/2}, \tag{3.3}$$

$$r = R_v = (3V / 4\pi)^{1/3}, \tag{3.4}$$

$$r = R_{eff} = 3V / S, \tag{3.5}$$

where *V* is the volume and *S* is the surface area of a Platonic solid, R is the radius of the circumscribing sphere, R_a, R_v and R_{eff} are the radii of the spheres that have the same surface area, volume and volume-to-surface ratio as the particle, respectively. With Eq. (3.2), the equivalent sphere of a nonspherical particle is defined in terms of its circumscribing sphere. With Eq. (3.3), the nonspherical particle has the same surface area as its spherical counterpart. Note that Eq. (3.3) also leads to the equivalence of projected area under random orientation conditions, because the averaged projected area of a randomly oriented convex nonspherical particle is one fourth of its surface area (Vouk

1948). The equivalent sphere counterpart defined in Eq (3.4) has the same volume and therefore the same mass as the corresponding nonspherical particle. With Eq. (3.5), the nonspherical particle and its spherical counterpart have the same volume-to-surface-area ratio. An interesting feature for the geometry of a Platonic solid is that the radius of the equivalent sphere defined in Eq. (3.5) is the same as the radius of the corresponding inscribed sphere (Fry et al. 2006). Table 3.2 lists the R_a, R_v and R_{eff} as well as the volumes and surface areas of the Platonic solids in a case where the radii of the spheres circumscribing them are all unity.

Table 3.2 The volume, surface area, R_a, R_v and R_{eff} of Platonic solids in a case where the radii of the spheres circumscribing the solids are all unity

Platonic solid	V	S	R_a	R_v	R_{eff}
Tetrahedron	0.5132	4.6188	0.6063	0.4967	0.3333
Octahedron	1.3333	6.9282	0.7425	0.6828	0.5774
Hexahedron	1.5396	8.0000	0.7979	0.7163	0.5774
Icosahedron	2.5362	9.5745	0.8729	0.8460	0.7947
Dodecahedron	2.7852	10.5146	0.9147	0.8728	0.7947

3.2.2. Single-scattering properties of Platonic solids in geometrical optics regime

Single-scattering properties of the Platonic solids with size parameters in the resonant region (i.e., when the size of a scattering particle is on the order of the incident wavelength) have been studied in Yang et al. (Yang et al. 2004) using the finite-difference time domain (FDTD) method (Yang and Liou 1996a). For small size parameters, it is shown that the scattering properties of

tetrahedron, hexahedron, and octahedron differ substantially from those of their spherical counterparts, whereas the scattering characteristics of icosahedron and dodecahedron are similar to those of spheres. Different from Yang et al. (2004), the present study is intended to understand the scattering characteristics of the Platonic solids with size parameters in the geometrical-optics regime.

A number of methods haven been developed for computing the scattering and absorption properties of nonspherical particles, which were reviewed by Wriedt (1998), Mishchenko et al. (2000), and Kahnert (2003). In the present study the geometric optics method is employed because of its applicability to large size parameters. Specifically, we modified the GOM developed by Yang and Liou (1996b) by incorporating an efficient ray-tracing scheme reported in Zhang et al. (2004) for the particle geometries involved in this study. The model use the geometrical ray-tracing technique to obtain the near field on the surface of the particle, and then the near-field is transformed to the far-field according to the electromagnetic equivalence theorem. The technical details of the GOM used in this study have been reported previously in Yang and Liou (1996a) and Zhang et al. (2004).

Figure 3.2 shows the extinction cross sections (C_e) and asymmetry factors (g) of Platonic solids and their spherical counterparts in a case for weak absorption. The incident wavelength and the refractive index are assumed to be 0.66 μm and $m = 1.31 + i1.65 \times 10^{-8}$ (the refractive index of ice at the wavelength of 0.66 μm (Warren 1984)), respectively. Note that the maximum dimensions, i.e. the diameters of the circumscribing spheres, of all Platonic solids in Fig. 3.2 are

assumed to be the same with a size parameter of $2\pi R/\lambda = 200$. As shown in Fig. 3.2a, the extinction cross sections of the Platonic solids are smaller than those of their spherical counterparts defined in terms of equal maximum dimension, which, however, are larger than those based on equal volume or equal effective size. Among the four spherical equivalences, the equivalence based on equal surface area has the smallest errors in terms of C_e. Figure 3.2a also shows that the differences in C_e between the Platonic solids and their four spherical counterparts decrease with decreasing particle asphericity. The behaviors of C_e in Fig 3.2 can be explained as follows. The extinction cross section of a particle with a size parameter in the geometrical optics regime is twice that of its projected area. Half of the extinction is due to the reflected and refracted rays, whereas the other half is due to diffraction that can be calculated approximately from Fraunhofer diffraction theory. Quantitively, the extinction and scattering cross sections in the geometrical-optics domain can be decomposed as follows:

$$C_e = C_a + C_s \approx 2P, \tag{3.6}$$

$$C_s = C_{diff} + C_{refl} + C_{refr} \tag{3.7}$$

where P is the projected area of particle, C_a is the absorption cross section, C_s is the scattering cross section. C_{diff}, C_{refl} and C_{tr} are, respectively, the diffraction, (external) reflection and refraction contributions. It is evident from Eq. (3.6) that the extinction cross sections of Platonic solids are closest to those of

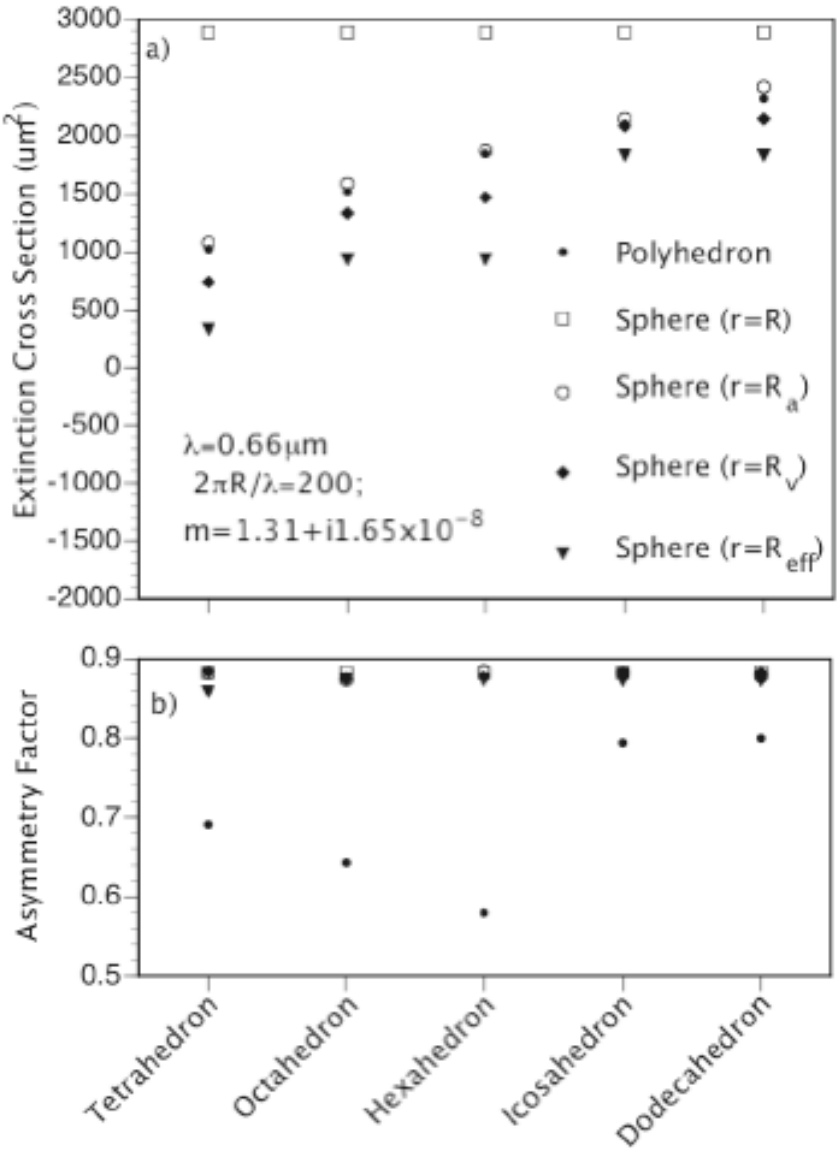

Figure 3.2 Comparison of the extinction cross-section (C_e) and asymmetry factor (g) between the Platonic solids and their spherical equivalences at a wavelength of $\lambda = 0.66\ \mu m$. All the particles are assumed to be ice with a refractive index of $m = 1.31 + i1.65 \times 10^{-8}$.

spheres defined in terms of equal surface area. Moreover, because R, R_a, R_v and R_{eff} approach the same value as particle asphericity decreases, the errors in C_e associated with the four types of spherical equivalences also decreases with decreasing asphericity, namely, from tetrahedron to dodecahedron.

In contrast to the extinction cross section, the asymmetry factors of the Platonic solids, shown in Fig 3.2b are independent of particle asphericity, although substantial differences are noticed between the results for the Platonic solids and spheres. These features indicate that, when absorption is weak, the asymmetry factor of a nonspherical particle is more sensitive to the detailed geometrical structures than to the overall extent of particle asphericity. Figure 3.2b also shows that all four types of spherical equivalences tend to overestimate the asymmetry factor substantially. Macke et al. (Macke et al. 1996) and Muinonen et al. (Muinonen et al. 1996) also noticed that spheres have relatively high asymmetry factors compared with polyhedral particles. Because of the extremely weak absorption, the single-scattering albedos of all Platonic solids and spheres are essentially unity and therefore not shown here.

Figure 3.3 shows the comparison of single-scattering properties between Platonic particles and their spherical counterparts in the case of strong absorption. The incident wavelength is assumed to be 11 μm and the corresponding refractive index for ice is $m = 1.10 + i0.25$ (Warren 1984).

Just as in the weak absorption case, the size parameters of the Platonic solids are also taken as 200. The features associated with C_e (see Fig. 3.3a) of Platonic solids and their spherical counterparts at the 11 μm wavelength are similar to those shown in Fig. 3.2a. However, as shown in Fig. 3.3b, the differences between asymmetry factors computed for Platonic solids and their spherical counterparts are less than 0.004, which are quite small in comparison with those in the case for weak absorption. This is because the scattered energy is essentially from the contributions of the external reflection and diffraction in the case of strong absorption. For a randomly orientated particle, both the processes are not sensitive to the shape of the scattering particle, leading to a weak dependence of the asymmetry factor on the particle shape (van de Hulst 1957). Fig. 3.3c shows the comparison of the single-scattering albedos. Evidently, all four types of spherical equivalences underestimate the single-scattering albedos of the Platonic solids. Note that the single-scattering albedo of the Platonic solids increase with the decreasing asphericity.

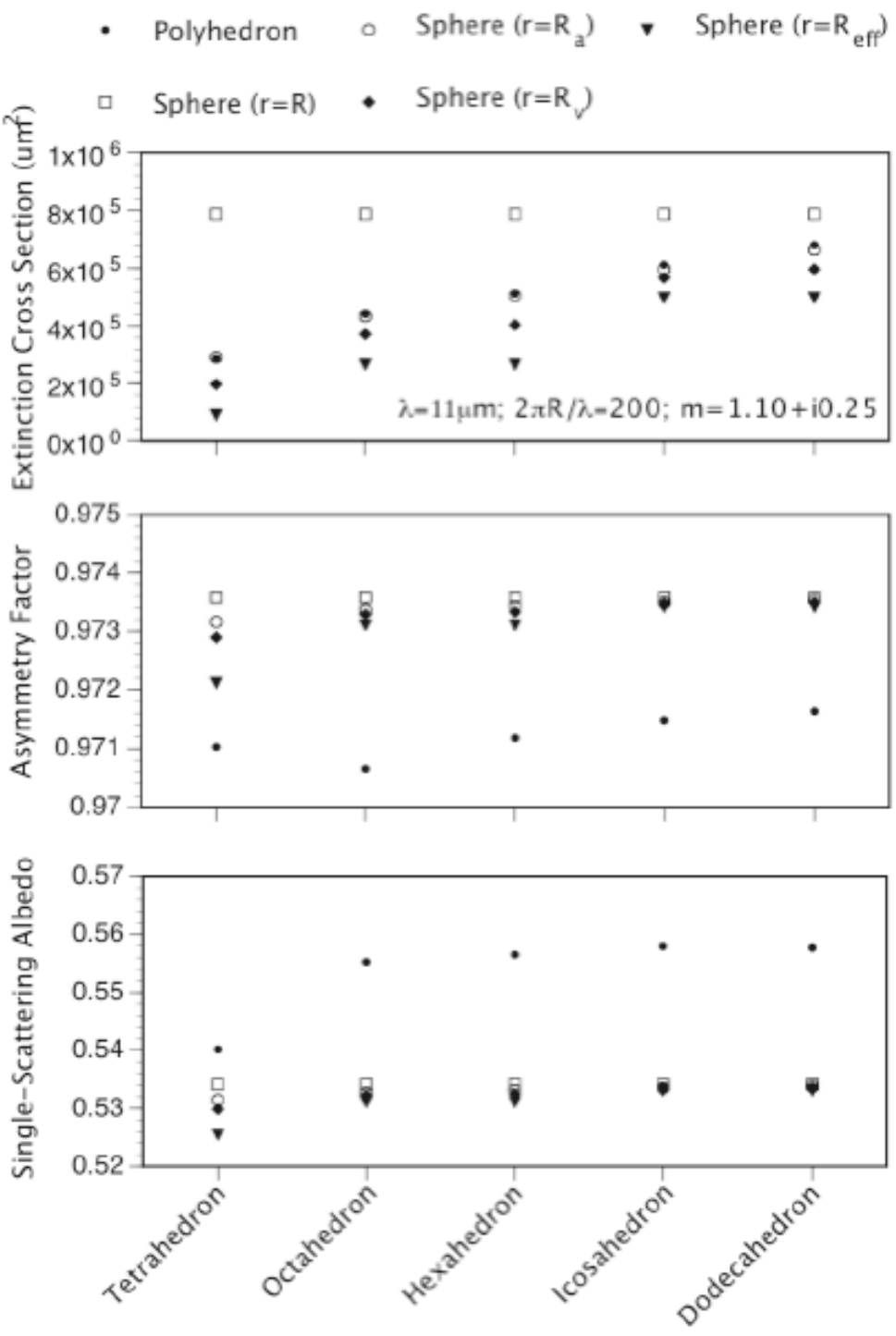

Figure 3.3 Comparison of the extinction cross-section (C_e), single-scattering albedo (ω), and asymmetry factor (g) between the Platonic solids and their spherical equivalences at a wavelength of $\lambda = 11\ \mu m$. All the particles are assumed to be ice with a refractive index of $m = 1.10 + i0.25$.

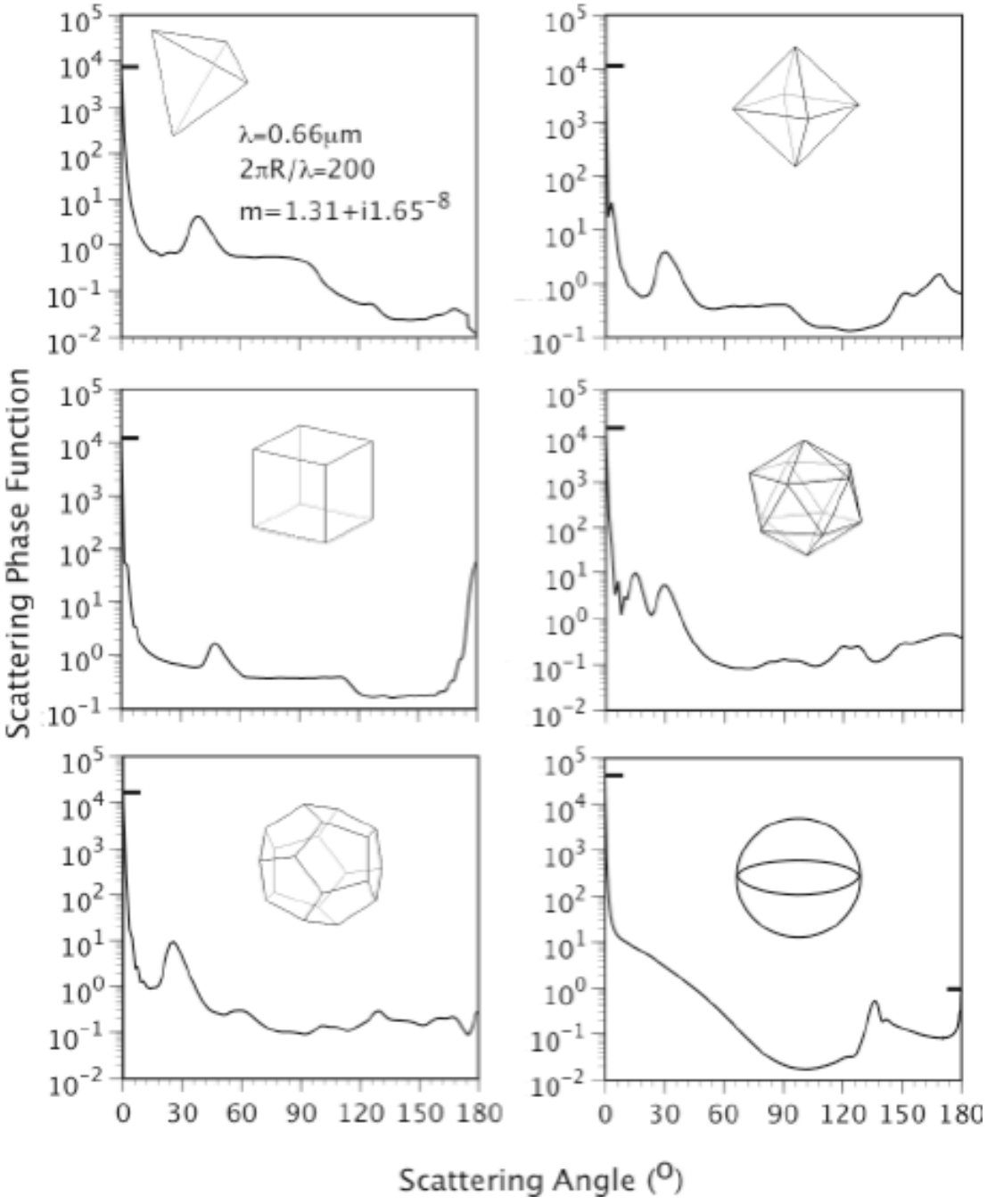

Figure 3.4 Comparison of the scattering phase functions between the Platonic solids and sphere at a wavelength of $0.66\ \mu m$.

Figure 3.4 shows the scattering phase functions of randomly oriented Platonic solids at a wavelength of 0.66 mm. The size parameter for all the Platonic solids is 200. The scattering phase function of an equivalent sphere based on Eq. (3.2) is also shown in Fig. 3.4. The phase functions of the spheres defined by Eqs (3.3) to (3.5) are all similar to that shown in Fig 3.4. To smooth the phase function of the sphere computed from the Lorentz-Mie theory, a modified gamma distribution with an effective variance of 0.1 is used. For the phase function of the sphere, a rainbow peak at a scattering angle of about 137^0 is evident because of the large size parameter used in this study. The phase functions of Platonic solids are quite different from that of the sphere. The pronounced peaks in the phase functions of the Platonic solids occur at moderate rather than large scattering angles. These peaks are due to two sequential refractions through two particle faces (Bohren and Huffman 1983), i.e. the mechanism for halos. The substantial differences between the phase functions of the Platonic solids and the sphere in Fig. 3.4 clearly show that the spherical equivalences are inadequate for the computation of scattered radiances.

Figure 3.5 is the same as Fig. 3.4, except for a case of strong absorption. The phase functions shown in Fig. 3.5 are essentially featureless. This is because the scattering phase functions are dominated by the diffraction and external reflection contributions when the scattering particles are strongly absorptive. For a randomly orientated particle, these contributions are not sensitive to the detailed geometrical details of a scatterer. Note that the scattered intensity at a specific scattering angle is determined not only by the phase function but also by the extinction cross section (C_e) and single-scattering albedo (ϖ) as follows (Bohren and Huffman 1983):

$$I_s(\theta_s) = \frac{I_0 C_e \varpi}{4\pi d^2} P(\theta_s), \tag{3.8}$$

where I_0 is the intensity of the incident radiation and d is the distance between the center of the scatter and the observation point. The above equation reveals that, even if the phase functions of two scatterers are quite similar, such as those of dodecahedron and the sphere in Fig. 3.5, the scattered intensity at the same scattering angle associated with the two scatterers can be substantially different due to the differences in their C_e and ϖ as shown in Fig. 3.3.

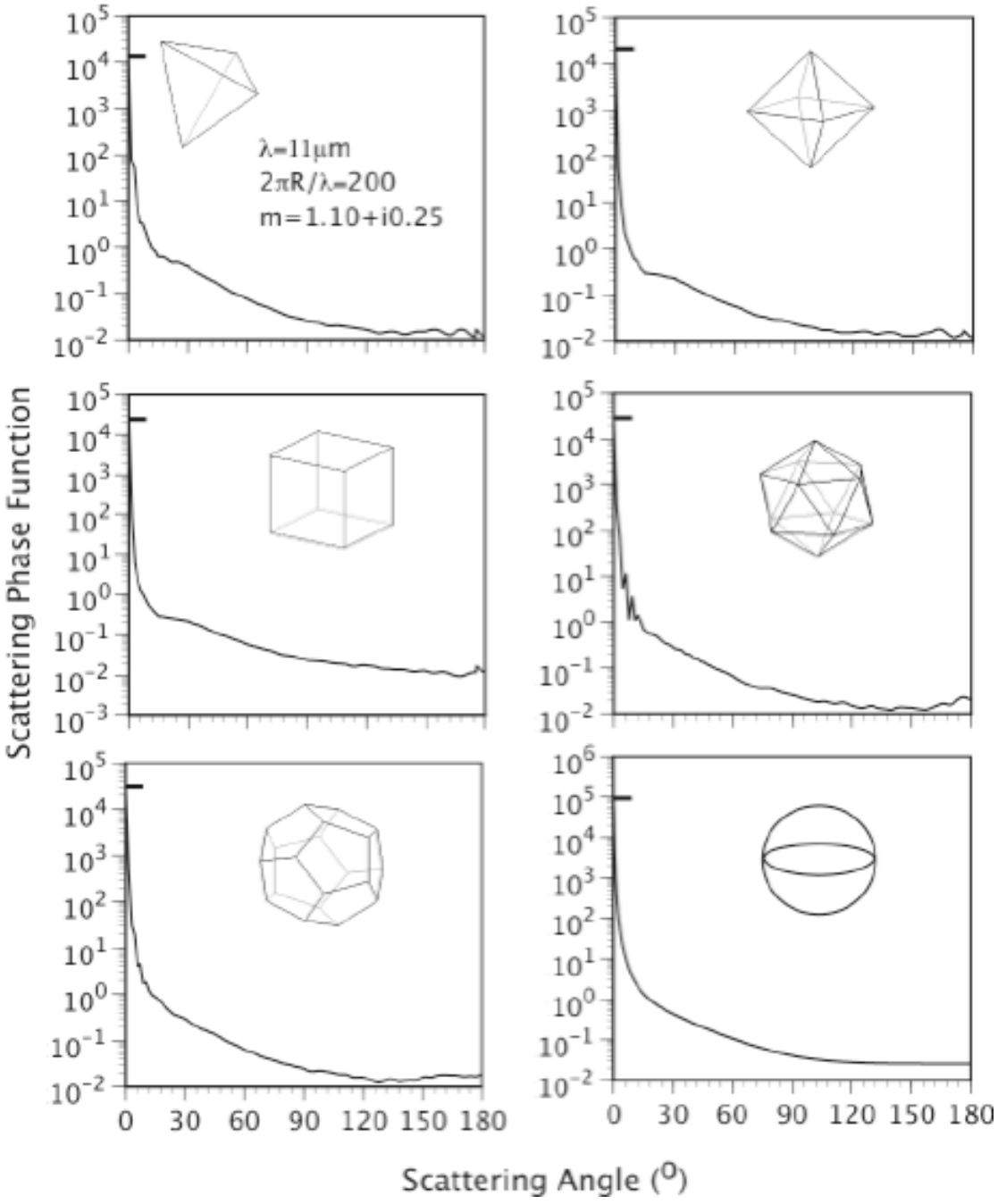

Figure 3.5 Same as Fig. 3.4, except for a wavelength of $11\mu m$.

3.3. Implications for measuring ice particle sizes with FSSP-type probes

The forward scattering spectrometer probe (FSSP), manufactured by particle measuring systems (PMS inc. Boulder, CO) is one of the most widely used instruments for measuring the size spectra of cloud particles (Knollenberg 1981). The design concepts, operation principles and limitations of FSSP have been reported in a number of studies (e.g., Knollenberg 1981; Baumgardner 1986; Gardiner and Hallett 1985). Here, only most salient features of FSSP are introduced. FSSP measures the forward-scattered light within its collecting angles produced by a cloud particle passing through a laser beam (He-Ne 632.8 nm, Dye and Baumgardner 1984) in the sampling volume of FSSP. Mathematically, the operation principle of FSSP is as follows (Dye and Baumgardner 1984):

$$RRF(D) = C_0 C_s(D) \int_{4^0}^{12^0} P_{11}(D,\Theta) \sin\Theta d\Theta , \qquad (3.9)$$

where D denotes the size of the cloud particle, RRF denotes the relative response function (RRF) directly measured by FSSP. C_s and P_{11} are the scattering cross section and phase function of the cloud particle, respectively. Θ is the scattering angle. C_0 is a constant specified during the calibration. The range for the collecting angles of the FSSP is usually from 4^o to 12^o .

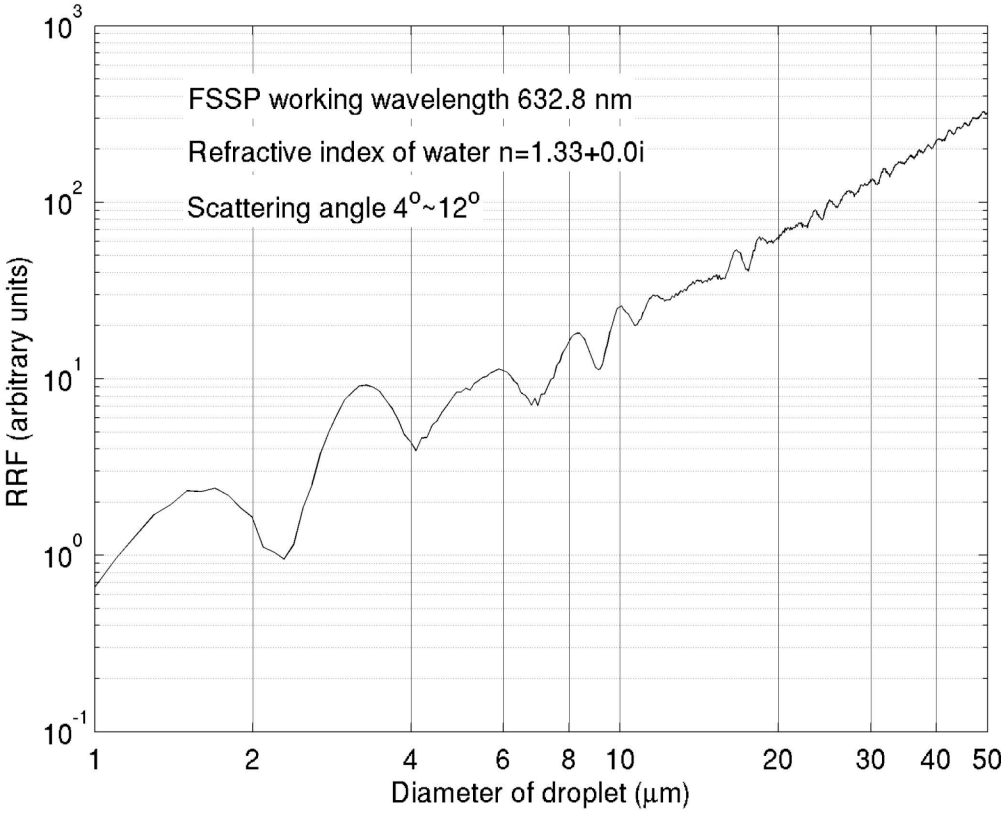

Figure 3.6 This figure shows the sensitivity of FSSP measurement, i.e., the relative response function, to the diameter of water droplets. The optical properties of water droplet at the FSSP working wavelength, 632.8nm, are computed using the Lorenz-Mie code.

Equation (3.9) indicates that the sensitivity of FSSP to cloud particle size comes from two parts. At the first order, the RRF increases linearly with the C_s of cloud particle, which in turn increases (square-power) with cloud particle size. Note that, because the scattering by an ice or water particle at 632.8 nm is conservative, i.e., not absorption, the extinction cross-sections, C_e, is equal to the scattering cross-sections, C_s. To a less extent, the response of FSSP is also sensitive the P_{11} of the cloud particle. Fig. 3.6 shows the sensitivity of FSSP

measurement to the size of water droplets. The Lorenz-Mie code developed by Wiscombe (Wiscombe 1979) is used in the computations involved in Fig. 3.6. Note that the algorithm scale is used for both axes. From Fig. 3.6, it is evident that the response of FSSP to cloud particle size generally follows $RRF \sim D^2$ (i.e., the square power law). This relationship is utilized in practice to infer the cloud particle size and extinction from FSSP measurements. It is worth of mentioning that, as clearly seen in Fig. 3.6, there exist noticeable "ripples" in the curve. These ripples are a result of the interference of transmitted and diffracted light (van de Hulst 1957). These ripples may lead to ambiguities (i.e., small particle size generates larger response) and result in fault particle size measurements (Knollenberg 1981). However, this effect is greatest at near micron sizes but almost completely damped at sizes characteristic of cloud droplet spectra, that is, 10 to 20 μm.

Although FSSP is originally designed to measure the size and extinction of water droplets, FSSP is also widely used for the measurement of aerosols and ice particles (e.g., Knollenberg et al. 1982; Knollenberg et al. 1993). Different from water droplets that are all approximately spheres, ice particles in cirrus cloud are, in most cases, nonspherical. However, because small ice particles usually have aspect ratios close to unity, they are usually assumed to be area-equivalent spheres in the interpretation of FSSP ice particle measurements (Garrett 2007; Heymsfield et al. 2006).

As introduced previously, it is still controversial whether the above assumption may lead to serious errors in FSSP measurements of ice particle

extinction cross-sections. To investigate this issue, we have computed the FSSP response functions for Platonic solids with sizes of about 40μm (corresponding size parameter with respect to the FSSP working wavelength, 632.8nm, is 200). As evident in Fig. 3.7, the responses of FSSP to Platonic solids are substantially smaller than those to equivalent, including area-equivalent, spheres.

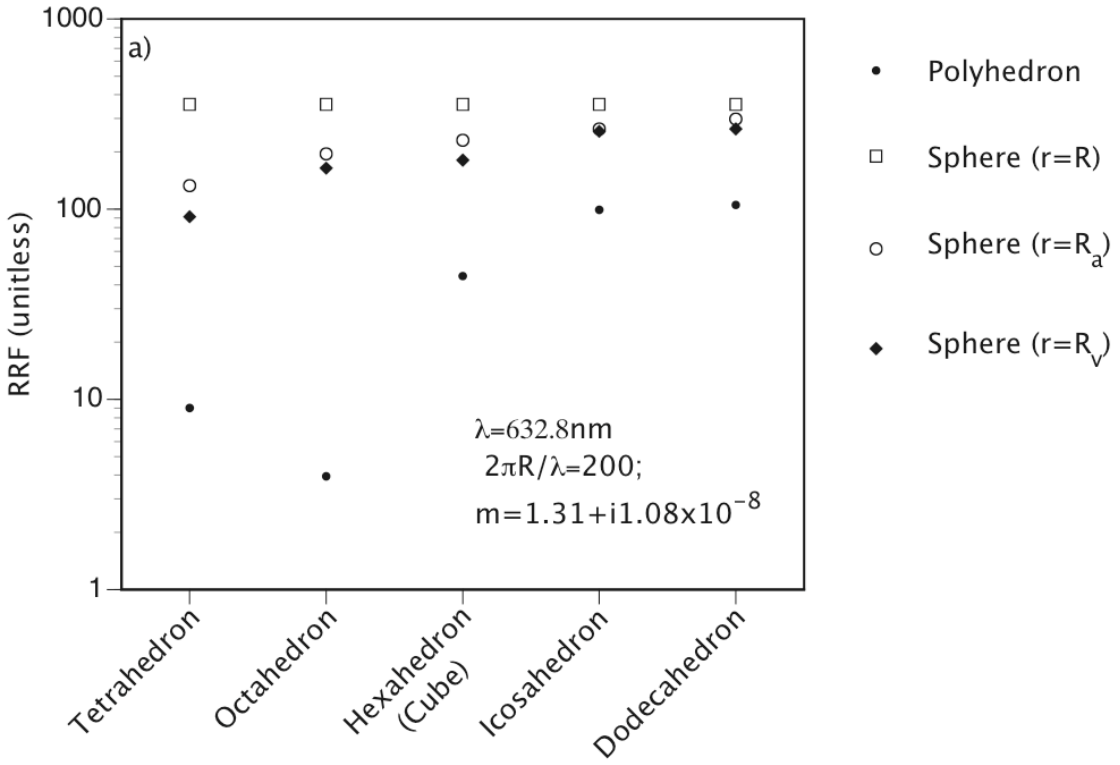

Figure 3.7 Responses of FSSP to Platonic solids and their equivalent spheres.

For Tetrahedron and Octahedron, which have relatively high asphericities (i.e., less like sphere), the differences are as large as orders of magnitude. For Icosahedron and Dodecahedron, which have relatively lower asphericities (more

like sphere) and therefore probably represent the nature of small ice particles better, a-factor-of-2.5 difference is found. Because of the nearly linear relationship between FSSP response function and particle extinction cross-section in Fig. 3.6, a-factor-of-2.5 difference in extinction cross-section is also expected.

Clearly, the above results are in favor of the argument that the sphericity assumption for small ice particles may lead to a-factor-of-2-to-2.5 underestimation of their extinction cross-sections by FSSP-type probes.

Now, the question is what has caused such substantial underestimation? As shown in Eq. (3.9), the response of FSSP is a function of two factors: the C_s and P_{11} of the observed ice particle. Fig. 3.2a reveals that the differences in C_s (note that $C_s = C_e$) between Platonic solids (dots) and their area-equivalent spheres (circles) are quite small. Therefore, this difference is probably attributed to the difference in P_{11} between Platonic solids and their equivalent spheres. Indeed, Fig. 3.2b has reveled that the asymmetry factors (the first moment of P_{11},) of Platonic solids are significantly smaller than those of equivalent, including area-equivalent, spheres. It indicates that the deviation of shape from sphere may lead to substantial decrease in the forward-to-back scattering ratio. This phenomenon has also noticed by Macke et al. 1996; Muinonen et al. 1996. The results of this phenomenon is that, although a Platonic solid has the same C_s as its area-equivalent sphere, the former scatters much less light to the collecting angles of FSSP (4^o~12^o) and therefore generates much smaller response than

the latter, leading to underestimation of the extinction and scattering cross-section.

3.4. Conclusions

To obtain a better understanding of the uncertainty in FSSP ice particle measurement caused by the sphericity assumption for small ice particles, we have first computed the scattering properties of Platonic solids. Then, the single-scattering properties of the Platonic solids are compared with those of four types of spherical equivalences that are defined in terms of (1) equal maximum dimension, (2) equal surface area, (3) equal volume, and (4) equal volume-to surface area ratio for size parameters in the geometric optics regime. The comparisons are made at two wavelengths, 0.66 μm and 11 μm, corresponding to weak and strong absorption, respectively. The comparisons show that the equal-surface-area spherical equivalence has the smallest errors in terms of the extinction cross-section for both the cases for weak and strong absorption. All spherical approximations substantially overestimate the asymmetry factor of the Platonic solids at 0.66 μm. In the case of strong absorption, spherical approximations underestimate the single-scattering albedo. The scattering phase functions of the Platonic solids at a wavelength of 0.66 μm are substantially different from that of the equivalent spheres because of the sensitivity of the phase function to particle morphological details. The phase functions of both the Platonic solids and spheres at 11 μm are quite featureless and similar because diffraction and external reflection dominate the scattered energy.

Based on the above results, we have also simulated the response of FSSP to Platonic solids and their equivalent spheres. It is found that the response of FSSP to Platonic solid is much smaller than its response to equivalent spheres. For Icosahedron and Dodecahedron, which have relatively lower asphericities (more like sphere) and probably represent the nature of small ice particles better, a-factor-of-2.5 difference is found. Therefore, our result is in support of the argument by Garrett (Garrett 2007) that the sphericity assumption for small ice particles may lead to a-factor-of-2-to-2.5 underestimation of their extinction cross-section. It is also found that the underestimation is largely due to the difference in scattering phase function between Platonic solids and their equivalent spheres. That is, a Platonic solid tends to scatter less light, in comparison with equivalent spheres, into the directions within the FSSP collecting angles, which leads to a smaller FSSP response and consequently underestimation of its extinction cross-section.

IV. A COMPARISON OF MODIS AND POLDER CIRRUS CLOUD OPTICAL THICKNESS RETRIEVALS

4.1. Background

Cirrus clouds play an important role in the climate system, primarily because they have significant influence on the radiative energy budget and thermal structure of the Earth-atmosphere system through their radiative effects (Liou 1986). However, our understanding of this role is very limited. Although it is generally believed that the net radiative forcing of most cirrus clouds is positive (i.e., warm the atmosphere) because of their high altitudes, the magnitude of this forcing and how it responses to global warming remains largely unclear (Houghton et al. 2001). Cirrus clouds are still crudely parameterized in today's general circulation models (GCMs) and their climatology and radiative forcing differ substantially from model to model (Zhang et al. 2005). Although *in-situ* observational data have greatly expanded our knowledge on cirrus clouds, they are limited by their small spatial and temporal sampling scales. To improve our understanding of the role of cirrus clouds in climate, continuous global observations of cirrus clouds from satellite-based instruments are indispensable.

A large panel of instruments devoted to cloud measurements has been successfully launched, such as the Moderate resolution Imaging Spectroradiometer (MODIS) and the Polarization and Directionality of the Earth's Reflectances (POLDER). MODIS is a passive sensor aboard both Terra and

Aqua. MODIS captures data in 36 spectral bands covering a wide spectral range, from 0.415 to 14.235 μm, with nadir spatial resolution that varies from 250 × 250 m^2 to 1 × 1 km^2 depending on band (Salomonson et al. 1989). POLDER is a wide field-of-view radiometer currently aboard the French satellite PARASOL. POLDER captures data in 9 bands all in shortwave region with a nadir spatial resolution of 6 × 6 km^2, (Deschamps et al. 1994). In comparison with MODIS, POLDER has relatively narrow spectral coverage and coarse resolution. However, POLDER performs multidirectional measurements (usually in 14, but up to 16 directions) of both reflectance and polarization, which prove to be rich in information about the microphysical properties of cirrus clouds (e.g., C.-Labonnote et al. 2001 and Baran and Labonnote 2006).

Among many cloud parameters retrieved by MODIS and POLDER, cloud optical thickness (τ_c) is one of the most important factors in determining the radiative forcing of clouds (Jensen et al. 1994). In this part of the study, we present a comparison of MODIS and POLDER cirrus cloud optical thickness retrievals. Through the comparison, we will address the following questions: How are the two retreivals different? What are the reasons for the difference? What are the possible implications of the difference for deriving the climatology and assessing the radiative effects of cirrus clouds from satellite data?

Note that both MODIS and POLDER cloud products have been widely used to derive the climatology, compute radiative forcing and validate parameterization of cirrus clouds (e.g., Chepfer et al. 1998; Hong et al. 2007). Therefore, the answers to above questions may not only help to identify and

reduce uncertainties in current cirrus retrieval algorithms, but may also improve our understanding of the climatic effects of cirrus clouds.

A number of current and future satellite-based sensors have instrument characteristics and cloud retrieval algorithms similar to MODIS or POLDER. For example, many design concepts of MODIS has been inherited by the Visible Infrared Imaging Radiometer Suite (VIIRS) that will fly on the National Polar-Orbiting Environmental Satellite System (NPOESS) and on the NPOESS Preparatory Project (NPP) (Miller et al. 2006). The APS (Aerosol Polarimetry Sensor), which is a key instruments deployed by NASA's Glory mission (Mishchenko et al. 2007), will be launched in the near future. The APS has the capabilities similar to POLDER, i.e., making polarimetric observations from multi-angles (Mishchenko et al. 2007). Therefore, findings from this study may provide valuable guidance for the development to of cirrus cloud retrieval algorithms for these future sensors.

Another motivation for this study is to obtain an understanding of the advantages and limitations of MODIS and POLDER operational cirrus cloud retrieval algorithms. Such understanding is crucial for the development of a MODIS-POLDER synergistic cirrus cloud retrieval algorithm. Both MODIS/Aqua and POLDER/Parasol are working in the framework of NASA's "A-train" satellite constellation and therefore taking nearly simultaneously measurements. MODIS and POLDER offer different, but somehow complementary, advantages for monitoring cloud properties. For example, Riedi et al. (Riedi et al. 2007) demonstrated that a combination of information from the two instruments brings

new perspectives for retrieving cloud top thermodynamic phase, which are helpful to discriminate and resolve some ambiguous cases. Therefore, a combination of MODIS and POLDER data for cirrus cloud retrieval is feasible and should be interesting. From this perspective, a comparison of stand-alone cirrus cloud retrievals from MODIS and POLDER is a necessary first step and should yield interesting information.

4.1.1. MODIS operational cloud optical thickness retrieval algorithm

The theoretical basis and practical implementation of the MODIS operational cloud optical thickness retrieval algorithm have been described in details by King et al. (King et al. 1997). Here, we only explain the fundamental principle behind the retrieval.

In this algorithm, cloud optical thickness is retrieved utilizing the solar reflective bands. Specifically, the 0.86 μm band (MODIS band #2) is used for cloud optical thickness retrieval over ocean and replace by the 0.66 μm band (MODIS band #1) over land surface. Both bands are located out side of the water vapor and oxygen absorption regions and the surface reflectance in these two bands is generally small, about 2%~7% over ocean (King et al. 1997; Jin et al. 2004). Consequently, in cloudy conditions, the reflection of solar radiation in these bands is largely due to the reflection of clouds.

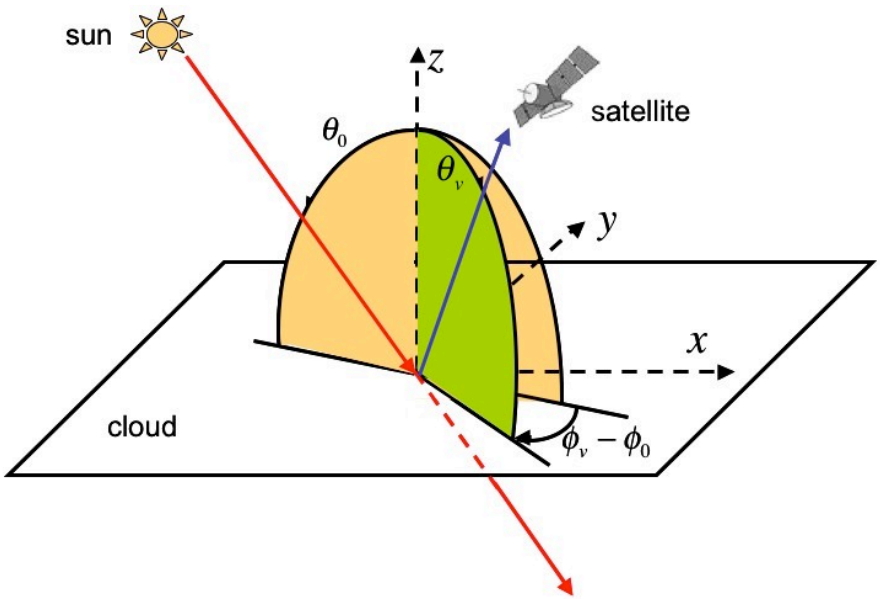

Figure 4.1 Schematic of sun-satellite viewing geometry. θ_0 is the solar zenith angle, ϕ_0 is the solar azimuthal angle, θ_v is the sensor viewing zenith angle, , and ϕ_v the sensor azimuthal angle.

It is well known that cloud reflection function depends on the following factors: 1)The optical thickness of cloud (τ_c), which is the integration of extinction over cloud physical thickness. 2) The bulk-scattering properties of clouds. More specifically, the single-scattering albedo ($\langle\omega\rangle$) and the scattering phase function of clouds ($\langle P_{11}\rangle$). 3) The sun-satellite viewing geometry. As illustrated in Fig. 4.1, the sun-satellite viewing geometry is determined by four angles, i.e., the solar zenith angle, θ_0 ($0<\theta_0<\pi/2$), the solar azimuthal angle, ϕ_0 ($0<\phi_0<2\pi$), the sensor viewing zenith angle, θ_v ($0<\theta_v<\pi/2$), and the sensor azimuthal angle, ϕ_v ($0<\phi_v<2\pi$).

The dependence of R_c on above factors can be clearly seen from the definition of R_c (Liou 2002):

$$R_c(\tau_c,\langle\omega\rangle,\langle P_{11}\rangle,\theta_0,\theta_v,\phi_v-\phi_0)=\frac{\pi I(\theta_v,\phi_v)}{\mu_0 F_0}, \tag{4.1}$$

where $\mu_0=\cos\theta_0$, $I(\theta_v,\phi_v)$ is the up-well radiance observed at the top of cloud in the satellite-viewing direction, and F_0 is the solar flux density in the direction specified by θ_0 and ϕ_0.

The scattering albedo ($\langle\omega\rangle$) and phase function ($\langle P_{11}\rangle$) of cloud are two important parameters in radiative transfer computation. The former determines the partitioning of cloud extinction between scattering and absorption. The latter determines the angular distribution of the scattered radiation. Together, $\langle\omega\rangle$ and $\langle P_{11}\rangle$ determine how a unit volume of cloud particles interacts radiatively with incident sunlight. The asymmetry factor ($\langle g\rangle$) is the first moment of $\langle P_{11}\rangle$. It indicates the ratio of forward-scattered to backward-scattered light and therefore an important bulk-scattering property of cloud. $\langle g\rangle$ is defined as follows (Liou 2002):

$$\langle g\rangle=\frac{1}{2}\int_{-1}^{1}\langle P_{11}(\cos\theta_s)\rangle\cos\theta_s d\cos\theta_s, \tag{4.2}$$

where θ_s is the scattering angle ($0<\theta_s<\pi$), which is dependent on of the sun-satellite viewing geometry as follows:

$$\cos\theta_s=\cos(\pi-\theta_0)\cos\theta_v+\sin\theta_0\sin\theta_v\cos(\phi_v-\phi_0). \tag{4.3}$$

As first suggested by Hansen and Travis (Hansen and Travis 1974), bulk-scattering properties of clouds are not dependent on the exact nature of cloud

microphysics, such as the particle size distribution and, in case of cirrus cloud, the ice particle habit distribution, depending primarily on the effective radiative radius (r_e) of cloud. The definition of r_e for cirrus clouds used in MODIS retrieval is as follows (Foot 1988):

$$r_e = \frac{3}{4} \frac{\int_{D_{\min}}^{D^{\max}} \left[\sum_{h=1}^{M} V_h(D) f_h(D) \right] \times n(D) dD}{\int_{D_{\min}}^{D^{\max}} \left[\sum_{h=1}^{M} A_h(D) f_h(D) \right] \times n(D) dD}, \tag{4.4}$$

where D is the ice particle size, $n(D)$ denotes number density of ice particles with size from D to $D + dD$. The value of $n(D)$ is specified by the particle size distribution (PSD). f_h is the ice particle habit fraction for habit h, M is the number of habits. $V_h(D)$ and $A_h(D)$ are respectively the volume and projection area of ice particle habit h with a size of D.

The relationship between r_e and bulk-scattering properties of cirrus clouds employed in the current version of MODIS operational cloud retrieval algorithm (collection 5) is based on a model due to Baum et al. (2005b) (hereafter referred to as “Baum05 model”). In Baum05 model, cirrus ice particles are categorized into six regular habits, i.e., droxtal, solid hexagonal column, solid hexagonal plate, hollow hexagonal column, bullet rosette and aggregate. The fraction of each habit as a function of ice particle size is assumed to follow the distribution illustrated in Fig 4.2. For the sake of later comparison with POLDER algorithm, it is important to point it out that the predominant habits in Baum05 model are plates, hollow and solid columns, and rosettes, as shown in Fig. 4.2. Moreover,

all ice particle habits are assumed to have smooth surfaces and no inclusions of air bubbles or aerosol particles.

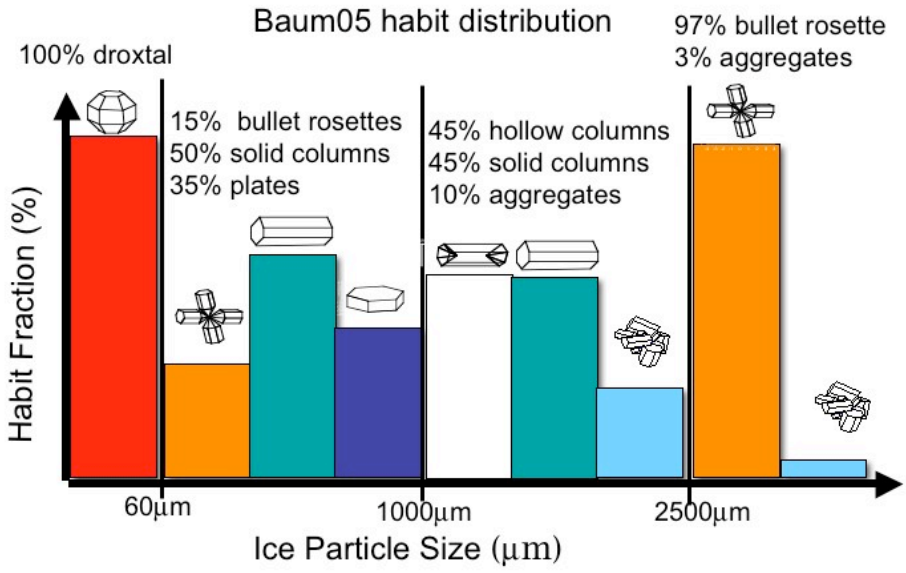

Figure 4.2 The ice particle habit distribution used in the Baum05 model (Baum et al. 2005a)

Because the absorption of ice is negligible (Warren 1984) in the 0.66 and 0.86μm bands, the single-scattering albedo $\langle \omega \rangle$ for these bands is essentially unity, i.e. the scattering within cirrus cloud in these bands is conservative. Consequently, for a given cloud optical thickness, the reflection function of cloud in these two bands is solely determined by the scattering phase function, $\langle P_{11} \rangle$, of cloud. The solid black line in Fig. 4.3a indicates the $\langle P_{11} \rangle$ of cirrus cloud with an effective radius r_e of 30 μm for MODIS 0.86 μm band according to Baum05 model. It is worthy of note that several pronounced scattering features associated with hexagonal shapes are clearly visible. For example, in the region between

60° to 180°, which is particular important for satellite-based and airborne instruments, the features include a steep slope between about 120° and 140°, a moderate scattering peak at about 156° and a sharp backscattering (180°) peak.

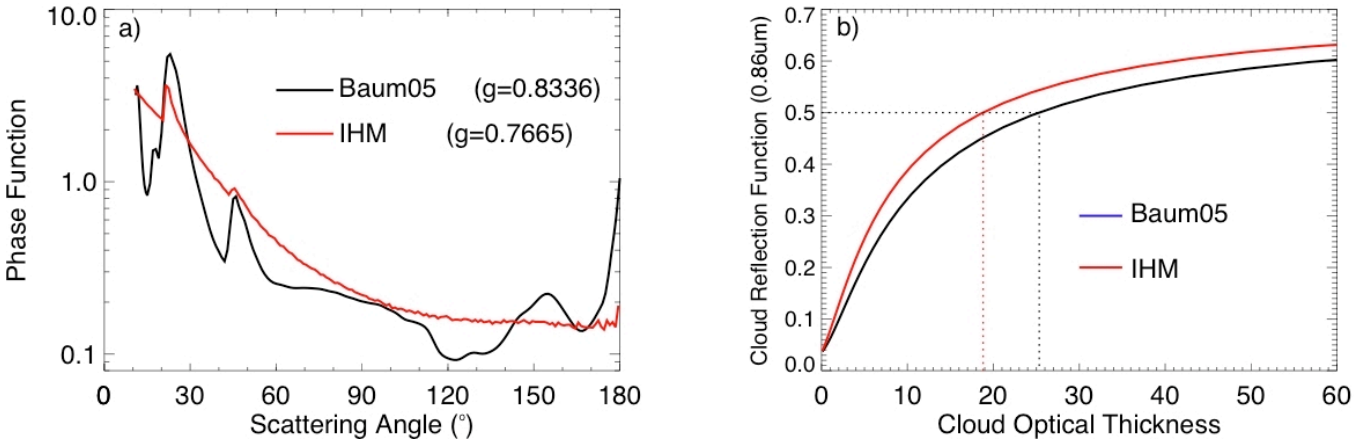

Figure 4.3 a) The scattering phase functions of cirrus clouds in MODIS 0.86-μm band based different ice particle microphysics. b) The look-up tables for MODIS cirrus cloud optical thickness retrieval corresponding to the scattering phase functions in a). In the radiative transfer simulation, the surface is assigned a Lambertian reflectance of 0.05. The solar zenith angle, satellite viewing zenith angle and sun-satellite relative azimuthal angle are 40^o, 20^o and 90^o.

The existence of these scattering features is due to the aforementioned fact that plates, hollow and solid columns, and rosettes predominate the Bum05 ice particle habit distribution and the all these habits have the basic hexagonal structure.

Given the bulk-scattering properties of cirrus clouds, the cloud reflection function (R_c) in the MODIS bands of interest (i.e., 0.66 and 0.86 μm bands) for a given cloud optical thickness (τ_c) and sun-satellite viewing geometry can be readily computed using radiative transfer models. The black line in Fig. 4.3b indicates the relationship between R_c and τ_c based on the Baum05 model in the

MODIS 0.86-μm band when $\theta_0 = 40^\circ$, $\theta_v = 20^\circ$ and $\phi_v - \phi_0 = 90^\circ$. The discrete ordinate model (DISORT) developed by Stamnes et al. (Stamnes et al. 1988) is used for the computations in Fig. 4.3b.

A precomputed database of the relationship between R_c and τ_c under various conditions, i.e., for different effective radii and sun-satellite viewing geometries, is the key component of the MODIS operational cloud retrieval algorithm. Such database is usually referred to as the "look-up table" (LUT) in MODIS nomenclature. Cloud optical thickness is retrieved in the operational algorithm by mapping the observed R_c onto an appropriate LUT (King 1987; King et al. 1997).

In addition to the theoretical basis, two other aspects of MODIS retrieval algorithm are worthy of mention here for the sake of the later comparison with POLDER retrieval. The first one is that MODIS retrieved cloud optical thickness at the horizontal resolution of 1 × 1 km^2. The other is that the effective radius of cloud is inferred on the basis of measurements of cloud reflection in the shortwave infrared (SWIR) bands, such the 1.6 and 2.1-μm bands.

4.1.2. POLDER operational cloud optical thickness retrieval algorithm

The POLDER operational cloud optical thickness retrieval algorithm is fairly similar to that of MODIS described above. POLDER also utilizes its 0.86-μm band for cloud optical thickness retrieval over ocean surface and the retrieval algorithm is also based on precomputed LUTs that relate cloud optical thickness to observed cloud reflection function (Buriez et al. 2005). However, the POLDER

cirrus cloud retrieval algorithm differs substantially from that of MODIS in the following four aspects.

1) Retrieval resolution. Although POLDER has a "full-resolution" of about 6 × 6 km^2, cloud optical thickness is retrieved at the resolution of "superpixel", which is about 18 × 18 km^2, composed of 3 × 3 full-resolution pixels (Buriez et al. 2005). In practice, radiances of 3 × 3 full-resolution pixels are first aggregated to the resolution of superpixel and then cloud optical thickness corresponding to an 18 × 18 km^2 superpixel is retrieved on the basis of the aggregated radiance.

2) Cirrus cloud bulk scattering model. The cirrus bulk scattering model employed in POLDER retrieval is the "Inhomogeneous Hexagonal Monocrystal" (IHM) model developed by C.- Labonnote et al. (C.-Labonnote et al. 2000). The IHM model is used, because it is found to be in good agreement with both total and polarized reflectance measurements of POLDER (C.-Labonnote et al. 2001). The IHM model corresponds to randomly oriented solid hexagonal column containing small air bubbles. The length/diameter ($L/2R$) of IHM ice particle is 137 μm /55 μm while the effective radius of air bubbles in IHM is 1 μm. The effective radius of IHM according to the definition in Eq. (4.4) is 30 μm. The $\langle P_{11} \rangle$ of the IHM model in POLDER's 0.86-μm band is shown in Fig. 4.3a. Evidently from Fig. 4.3a, the $\langle P_{11} \rangle$ of IHM model (red line) is substantially different from that of Baum05 model (black line). First of all, the $\langle P_{11} \rangle$ of IHM model is quite smooth and essentially featureless. Those scattering peaks in $\langle P_{11} \rangle$ of Baum 05 model are effectively smoothed out due to the inclusion of small ice bubbles (C.-

Labonnote et al. 2000). Another important difference between IHM and Baum05 model is in asymmetry factor. According to Baum05 model, the asymmetry factor of cirrus cloud with an effective radius of 30 μm at the wavelength of 0.86μm is 0.8336, while the corresponding value of the IHM model is 0.7665.

3) Absence of SWIR band in the retrieval. The spectral coverage of 9 POLDER bands in wavelength is ranging from 0.443 to 0.910 μm. The absorption of ice in these bands is weak. As a result, POLDER lacks the capability to retrieve the effective radius of cirrus clouds. This leads to some uncertainties in POLDER cloud optical thickness retrieval.

4) Multidirectional optical thickness retrieval. As aforementioned, POLDER performs measurements of solar reflection in multiple directions. This multi-directional capability of POLDER is illustrated in Fig 4.4. In the figure, the 14 POLDER viewing directions (filled black squares) over a pixel (1.13^{o} N; 81.38^{o} W July 22th, 2007, local time 13:43) are plotted in a (θ_v, ϕ_v) polar diagram, of which

the radius corresponds to satellite-viewing zenith angle θ_v, and the angle corresponds viewing azimuth ϕ_v relative to the solar direction ϕ_0. The red star in the figure indicates the solar zenith angle ($\theta_0 = 26.81^\circ$). Isoscattering angle, θ_s, is also contoured from 80° to 170° in 10° increments. With such multi-directional capability, POLDER first retrieves cloud optical thickness all available directions. Then, a directionally averaged optical thickness is derived from the multi-directional retrievals as follows:

$$\tau_c = \frac{1}{N}\sum_{i=1}^{N}\tau_c(\theta_{v,i},\phi_{v,i}), \tag{4.5}$$

where $\tau_c(\theta_{v,i},\phi_{v,i})$ is the cloud optical thickness retrieved in i^{th} direction $(\theta_{v,i},\phi_{v,i})$, N is the total available direction. Several studies have shown that the multi-directional cloud optical thickness retrievals from PODLER contain rich information on the microphysical properties of cirrus clouds (e.g., C.-Labonnote et al. 2001; Baran and Labonnote 2006; Knap et al. 2005).

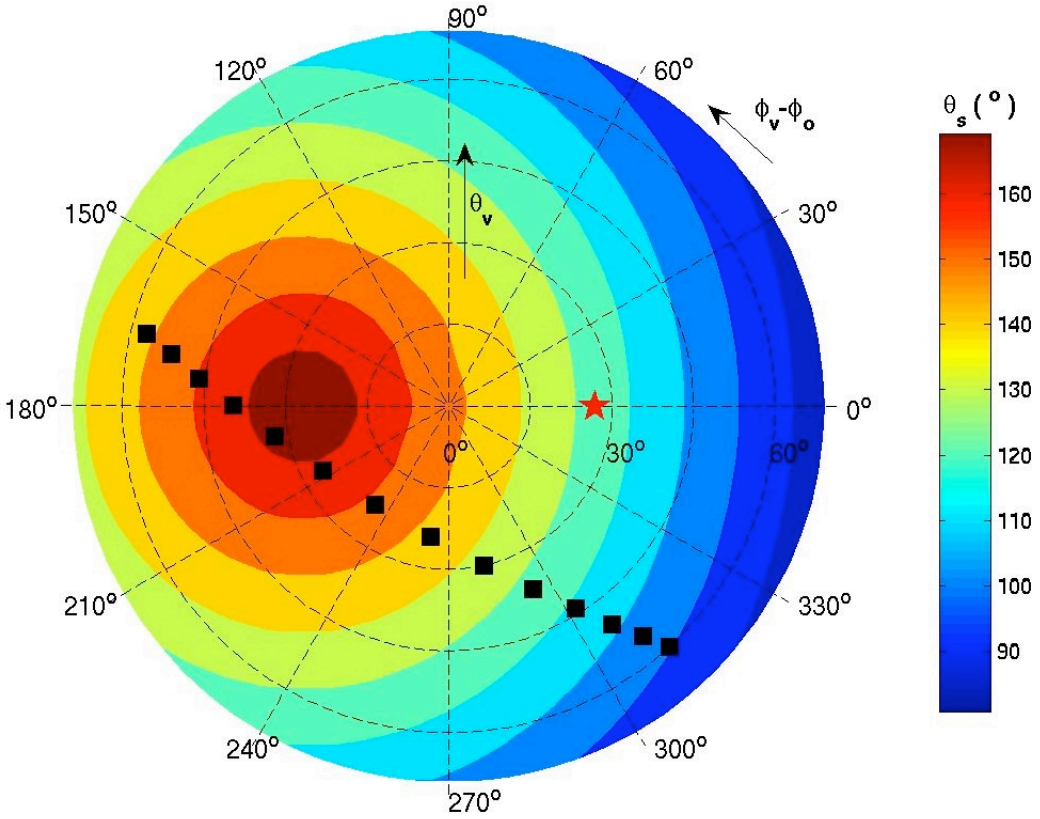

Figure 4.4 Schematic of POLDER angular sampling pattern. The black squares correspond to 14 POLDER viewing directions over a chosen pixel (1.13^o N; 81.38^o W July 22th, 2007, local time 13:43). The radius of the polar coordinate corresponds to satellite-viewing zenith angle θ_v, and the angle corresponds viewing azimuth ϕ_v relative to the solar direction ϕ_0. The red star in the figure indicates the solar zenith angle ($\theta_0 = 26.81^\circ$). Isoscattering angle, θ_s, is contoured in color from 80° to 170° in 10° increments.

4.2. Comparison of MODIS and POLDER cirrus cloud optical thickness retrievals

4.2.1. Case selection

For the comparison of MODIS/Aqua and POLDER/Parasol level-2 cirrus cloud topical thickness retrievals, we have selected an Aqua-MODIS granule acquired over Central America at 18:45 UTC on July 22, 2007. A true-color (R, 0.645-μm; G, 0.555-μm; B, 0.469-μm) composite image of the granule is shown in Fig. 4.5. The evolution of cloud systems over this area from 10:45 to 20:28 UTC observed from geostationary satellites (GOES-10 and GOES-12) is shown in Fig. 4.6. The images in Fig. 4.6 are provides by NASA Langley center (http://www-angler.larc.nasa.gov/tc4/). It can be inferred from GOES observations that, a deep convective system developed early to the south of Panama had dissipated, leaving behind the anvil clouds that cover the center of the MODIS granule in Fig 4.5. To the northeast of the anvils is another convective system at its later stage.

An important consideration for the selection of the granule in Fig. 4.5 is that NASA's TC^4 mission (Tropical Composition, Cloud and Climate Coupling) was conducted during July and August 2007 over the same region. Various in-situ and remote sensing instruments were employed in TC^4 mission, flying on board three NASA research aircraft, specifically, ER-2, DC-8 and WB57. On July 22, 2007, several flight segments of the ER-2 and DC-8 coincided with the over-flight of "A-train" (Steven Platnick, Personal communication). Although the data

from TC[4] mission are not publicly available yet at the moment of writing, they may provide valuable information on the case for future study.

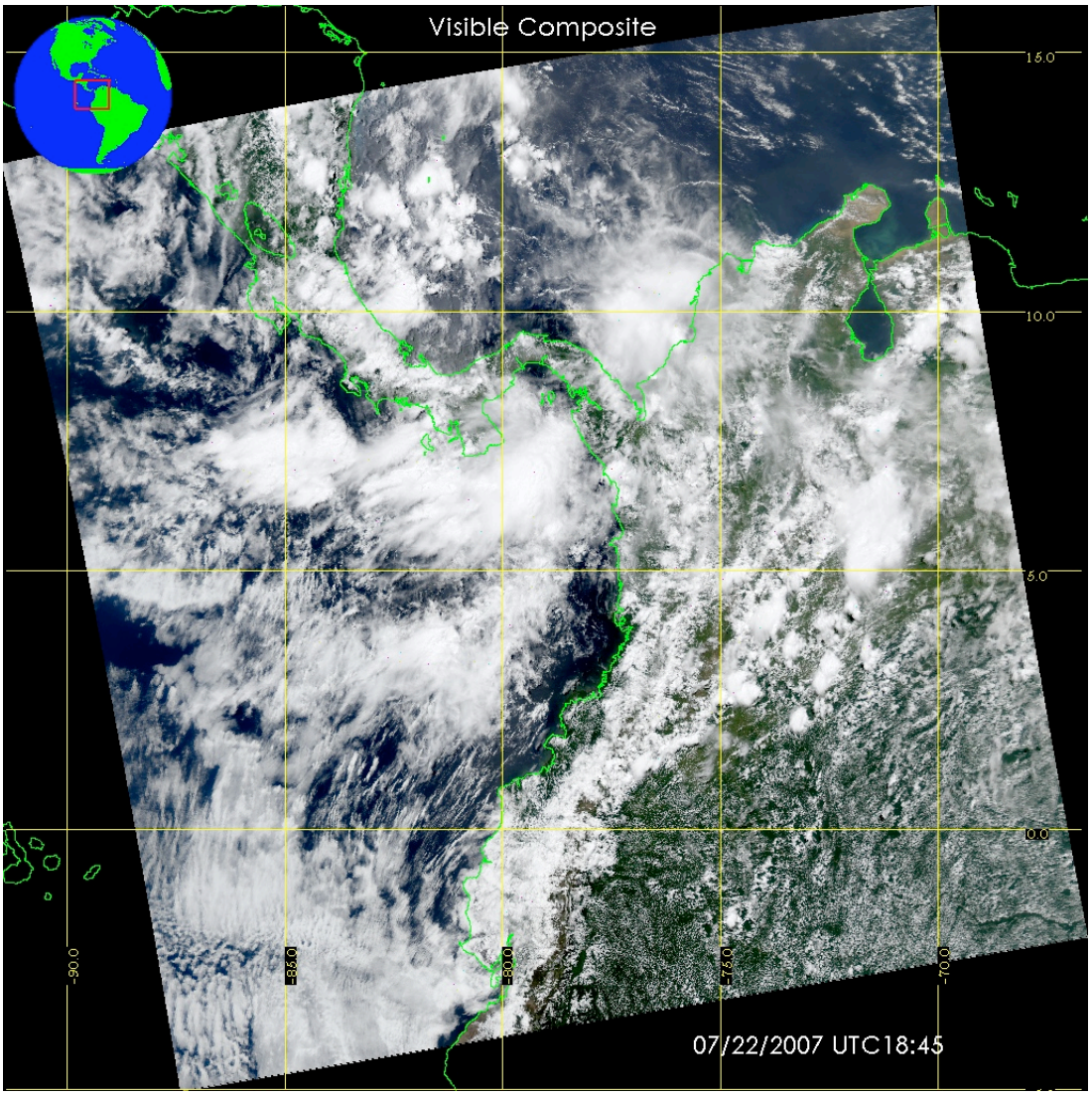

Figure 4.5 The true-color image of the selected MODIS/Aqua granule over the Central America on July 22, 2007 (UTC time 18:45).

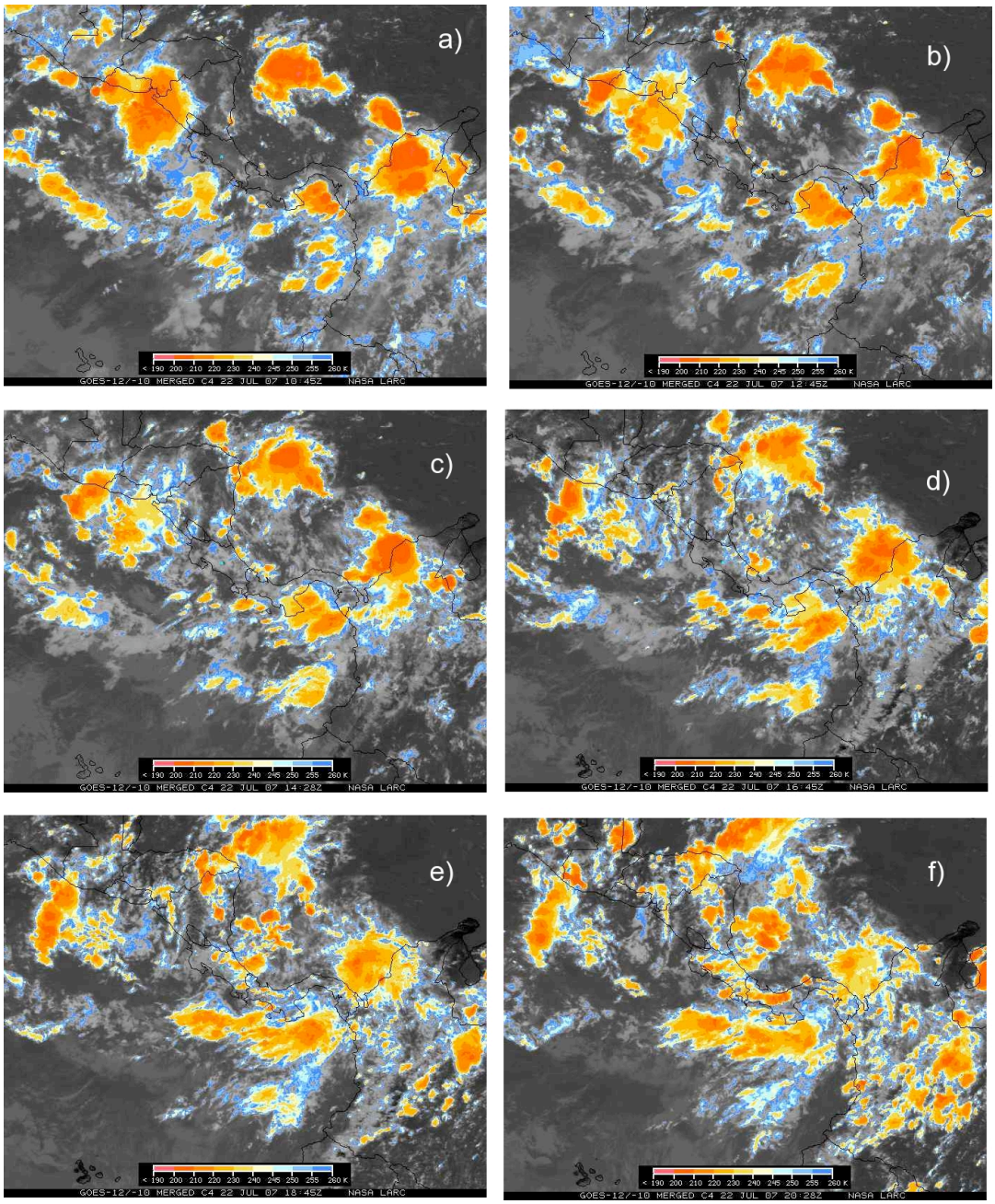

Figure 4.6 GOES-12 and GOES-10 merged infrared (11μm) color images over Central America for a) 10:45 b) 12:45 c) 14:28 d) 16:45 e) 18:45 and f) 20:28 UTC, on July 22, 2007.

4.2.2. MODIS/POLDER collocation

An important step before the comparison is the collocation of MODIS and POLDER retrievals. Both the level-2 operational cloud products and level-1 geolocated radiance products have been collocated using a state-of-the-art data fusion system developed by Laboratoire d'Optique Atmospherique (France). The collocation is made at the POLDER full resolution, i.e., 6 × 6 km^2. The objective of the collocation is to obtain two sets of cloud properties for each collocated pixel, one corresponding to MODIS and the other corresponding to POLDER retrieval. Further detail follows.

1) Level-1 product collocation. The POLDER level-1 geolocated radiance product (L1-B) has the POLDER full resolution, i.e., 6 × 6 km^2. The MODIS level-1 product used for the collocation, MOD021km, has the resolution of 1 × 1 km^2. To collocate these two products, MODIS pixels are first collocated to POLDER full resolution pixels. Then, within each POLDER full resolution pixel, radiances from MOD021km product are averaged over all pixels to obtain a mean radiance for the collocation.

2) Level-2 product collocation. As aforementioned, the MODIS level 2 cloud product (MOD06) has the horizontal resolution of 1 × 1 km^2. The POLDER level 2 cloud product (RB2) has the resolution of POLDER super-pixel, i.e., 18 ×18 km^2. The collocation of MODIS and POLDER level 2 products is made at POLDER full resolution, i.e., 6 × 6 km^2. The collocation consists of two steps. In the first step, POLDER full-resolution pixels (6 × 6 km^2) are collocated to the

POLDER super-pixels (18 × 18 km^2). After this first step collocation, cloud properties from POLDER RB2 products are assigned to full-resolution pixels. Note that, if two full-resolution pixels are within the same super-pixel, the same cloud properties POLDER full-resolution pixels will be assigned to both of them. In the second step of the collocation, MODIS MOD06 pixels with 1 × 1 km^2 resolution are first collocated to POLDER full-resolution pixels. Then, within each POLDER full-resolution pixel, cloud properties from MODIS MOD06 cloud product are averaged over all MODIS pixels to obtain a new set of cloud properties. Therefore, after the above two-step collocation, each POLDER full-resolution pixel has two sets of cloud properties, one from PODLER RB2 and one from MODIS MOD06 cloud product.

The bulk scattering properties of water clouds consisting of spherical water droplets differ substantially from those of ice clouds consisting nonspherical ice particles. For this reason, both MODIS and POLDER retrieval algorithms require information of cloud top thermodynamic phase (i.e., ice cloud or water cloud) for cloud optical thickness retrievals. Figure 4.7 shows the cloud thermodynamic phase retrievals from MODIS (left panel) and POLDER (right panel) for the image of Fig. 4.5. Although the two fairly well on the over-all pattern of cloud top thermodynamic phase, significant differences are observed, especially, along cloud edges. The reasons for the differences between MODIS and POLDER cloud top thermodynamic phase retrievals fall out of the scope of this study but interested readers are directed towards Riedi et al. (Riedi et al. 2007). To eliminate the uncertainty caused by the difference between MODIS

and POLDER in cloud phase retrieval, only those pixels that are labeled as ice clouds by both MODIS and POLDER are chosen for the cloud optical thickness comparison.

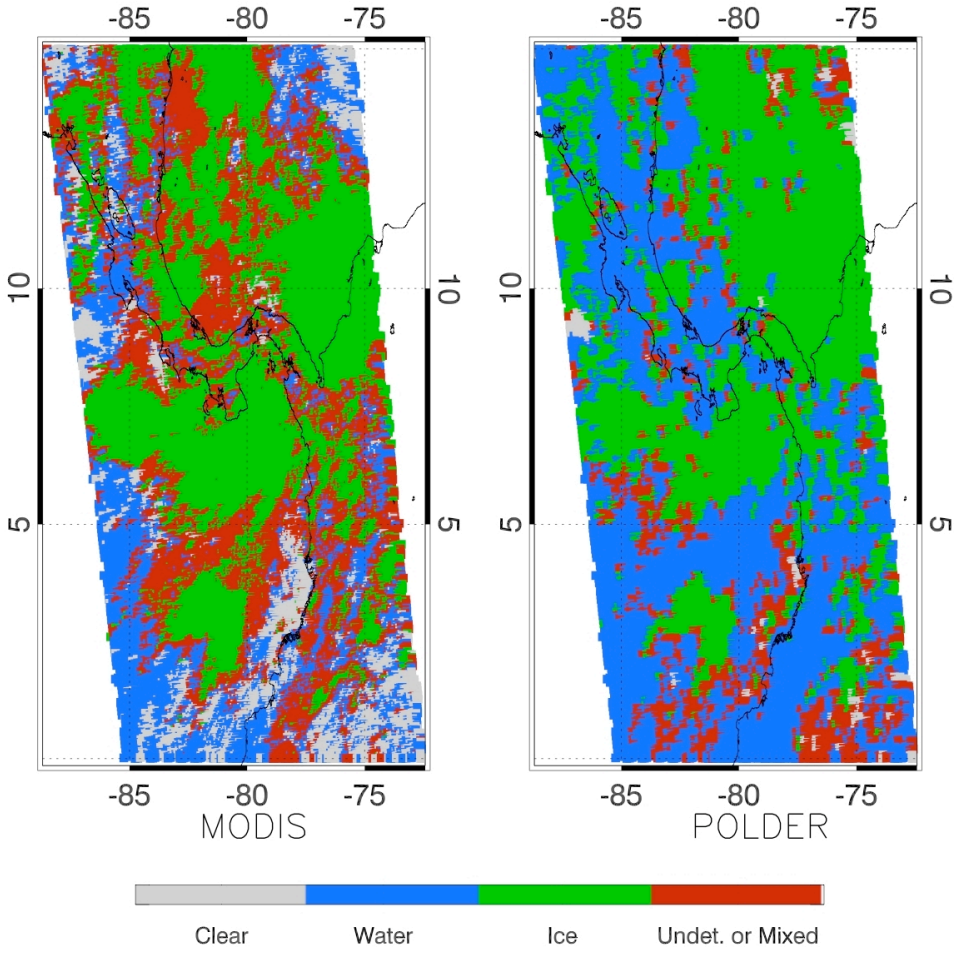

Figure 4.7 Cloud top thermodynamic phase retrieval from MODIS (left panel) and POLDER (right panel) cloud products for the granule in Fig. 4.5

4.2.3. Results

Figure 4.8 shows the cloud optical thicknesses (τ_c) of cirrus clouds in the selected granule from MODIS (left panel) and POLDER (right panel). The τ_c retrieval from POLDER (τ_c^{POLDER}) is similar to that of MODIS (τ_c^{MODIS}) in overall pattern. However, the difference in retrieval resolution between MODIS and POLDER is evident. It is also clear in Fig. 4.8 that POLDER tends to retrieve smaller τ_c than MODIS. Such difference is more evident in Fig. 4.9, which shows a scatterplot of pixel-to-pixel comparison between MODIS and POLDER retrievals. Fig. 4.9 also reveals that τ_c^{POLDER} is in good correlation with τ_c^{MODIS}. To further investigate the relationship between τ_c^{POLDER} and τ_c^{MODIS}, we plotted the density and cumulative distribution functions of $\tau_c^{POLDER} / \tau_c^{MODIS}$ in Figs. 4.10a and 4.10b, respectively. Here, the density of $\tau_c^{POLDER} / \tau_c^{MODIS}$ is defined as the fraction of pixels with certain value of $\tau_c^{POLDER} / \tau_c^{MODIS}$. Note that the density function in Fig. 4.10a has been normalized with respect to its maximum value. It is intriguing to note that $\tau_c^{POLDER} / \tau_c^{MODIS}$ seems to follow the log-normal distribution, i.e.,

$$\log_{10}\left(\frac{\tau_c^{POLDER}}{\tau_c^{POLDER}}\right) \sim N(\mu, \sigma^2). \tag{4.6}$$

The median value of $\tau_c^{POLDER} / \tau_c^{MODIS}$ is 0.6827. The blue line in Fig. 4.9 corresponds to $0.6827\tau_c^{MODIS}$, which, apparently, fits POLDER retrievals fairly well. The histograms of $\tau_c^{POLDER} / \tau_c^{MODIS}$ show that τ_c^{POLDER} is smaller than τ_c^{MODIS}, (i.e.,

$\tau_c^{POLDER} / \tau_c^{MODIS} < 1$) for about 80% of total pixels and for half of total pixels, τ_c^{POLDER} is smaller than τ_c^{MODIS} by more than about 30%.

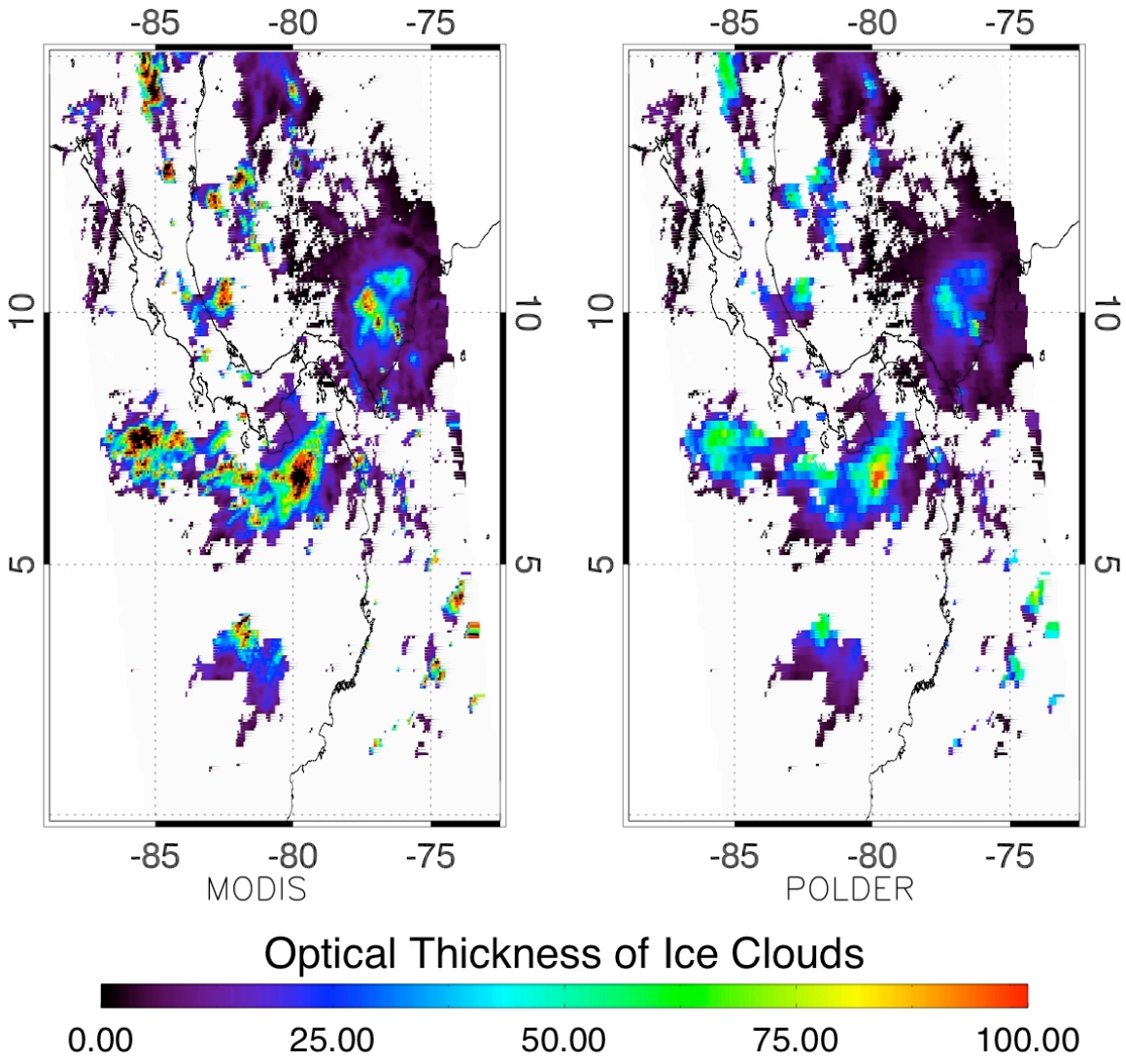

Figure 4.8 The cloud optical thickness of ice clouds in the granule of Fig. 4.5 according to MODIS (left panel) and POLDER (right panel) cloud products. Note that only pixels labeled as "ice cloud" by both MODIS and POLDER are plotted.

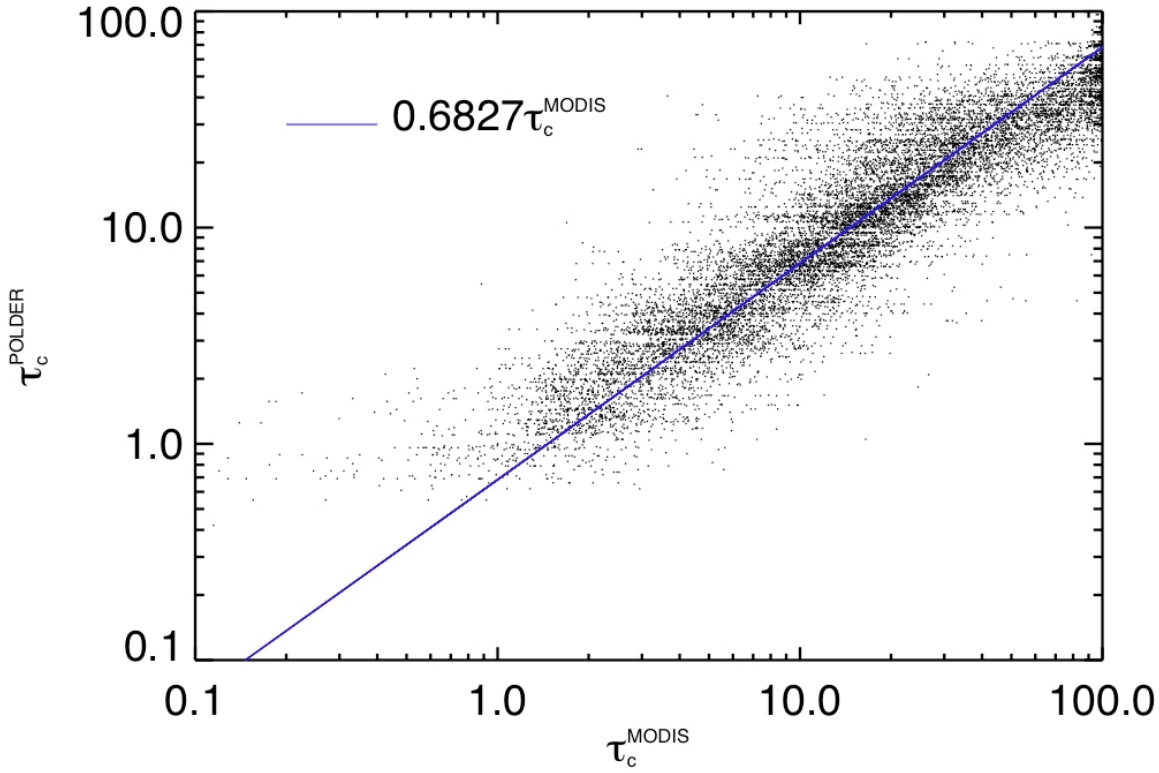

Figure 4.9 A scatter plot of POLDER (τ_c^{POLDER}) versus MODIS (τ_v^{MODIS}) cirrus optical thickness retrieval, along with a linear fit (blue line) of τ_c^{POLDER} by $0.6827\tau_v^{MODIS}$. Note that the logarithm scale is used in both axes.

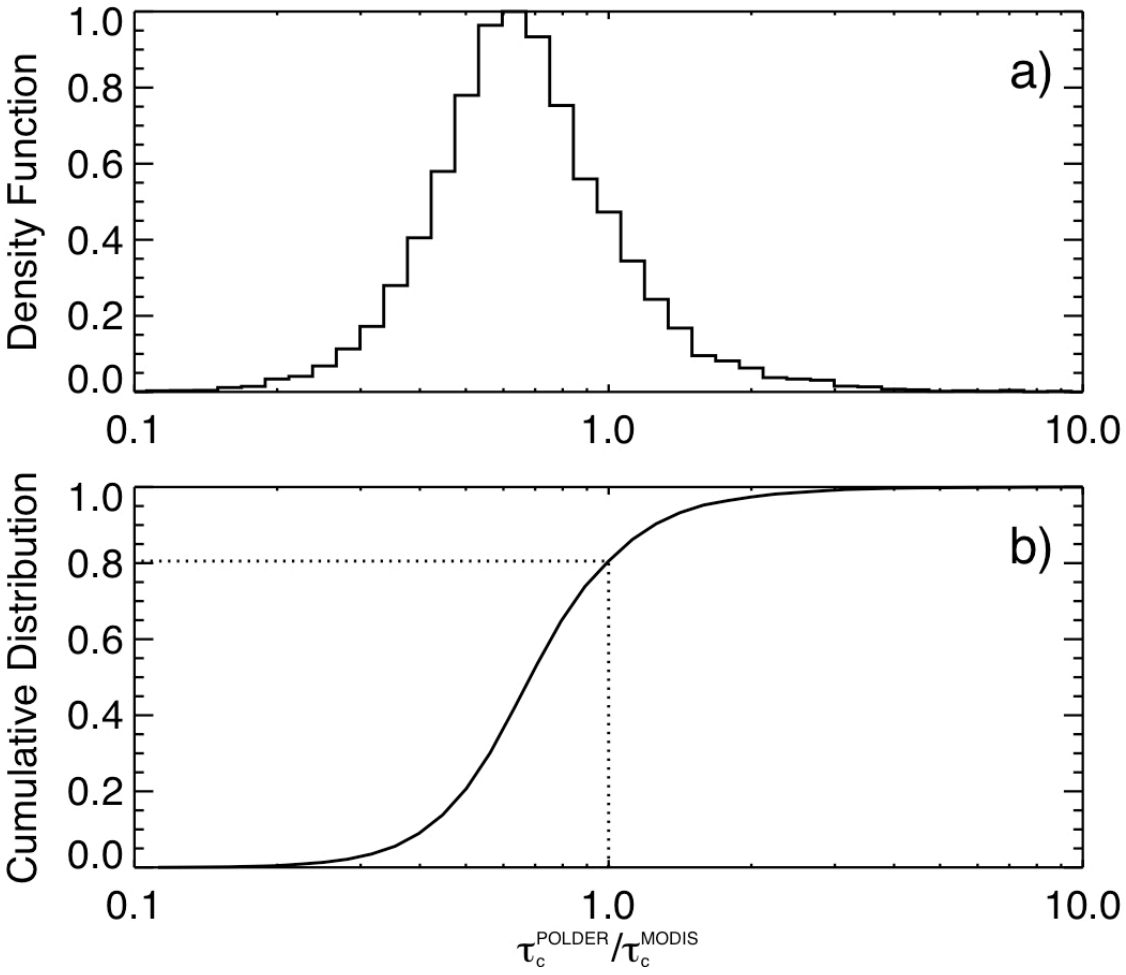

Figure 4.10 The histograms of the ratio $\tau_c^{POLDER} / \tau_c^{MODIS}$. This figure shows a) the probability density function and b) cumulative distribution of $\tau_c^{POLDER} / \tau_c^{MODIS}$. The density function is defined as the fraction of pixels within certain intervals of $\tau_c^{POLDER} / \tau_c^{MODIS}$ over the total collocated cirrus cloud pixels. Note that the density function in a) has been normalized with respect to its maximum value.

4.2.4. Discussion

It is shown in last section that optical thickness of cirrus clouds retrieved from POLDER is substantially smaller than that from MODIS. In this section we investigate the possible reasons for this difference.

As introduced in section 4.1, MODIS and POLDER operational cloud retrieval algorithms are different in several aspects. It is very likely that these differences in retrieval algorithm have contributed to the difference between τ_c^{POLDER} and τ_c^{MODIS} shown in Figs. 4.9 and 4.10. A detailed analysis follows.

1) The effect of retrieval resolution. It is well known that, due to cloud heterogeneity and the nonlinear dependence of cloud reflection on cloud optical thickness, the average cloud reflection of a cloudy scene found by averaging reflection of independent pixels within the scene tends to be smaller than that calculated using the average cloud optical thickness in the scene (Cahalan et al. 1994; Oreopoulos and Davies 1998). This difference, termed as the "plane-parallel albedo bias", is schematically illustrated in Fig. 4.11. Consider a simplest case, as in Fig. 4.11, where the optical thickness distribution with in a cloudy pixel consists of only two values, for example, 10.0 and 30.0. The cloud optical thickness ($\tau_c^{retrieval}$) retrieved from the averaged cloud reflection (i.e, $\left[R_c(10.0)+R_c(20.0)\right]/2$) is 16.5, which is significantly smaller than the arithmetic mean optical thickness ($\tau_c^{average}$), 20.0. As introduced previously, τ_c^{POLDER} for each collocated pixel is from POLDER level-2 product, in which cloud optical thickness is retrieved from cloud reflection measured at the resolution of 18 × 18 km^2 ,

while τ_c^{MODIS} for each collocated pixel is an arithmetic mean of MODIS level-2 retrievals with spatial resolution of 1 × 1 km^2. As a result, the plane-parallel bias could be a reason explaining why τ_c^{POLDER} is substantially smaller than τ_c^{MODIS}.

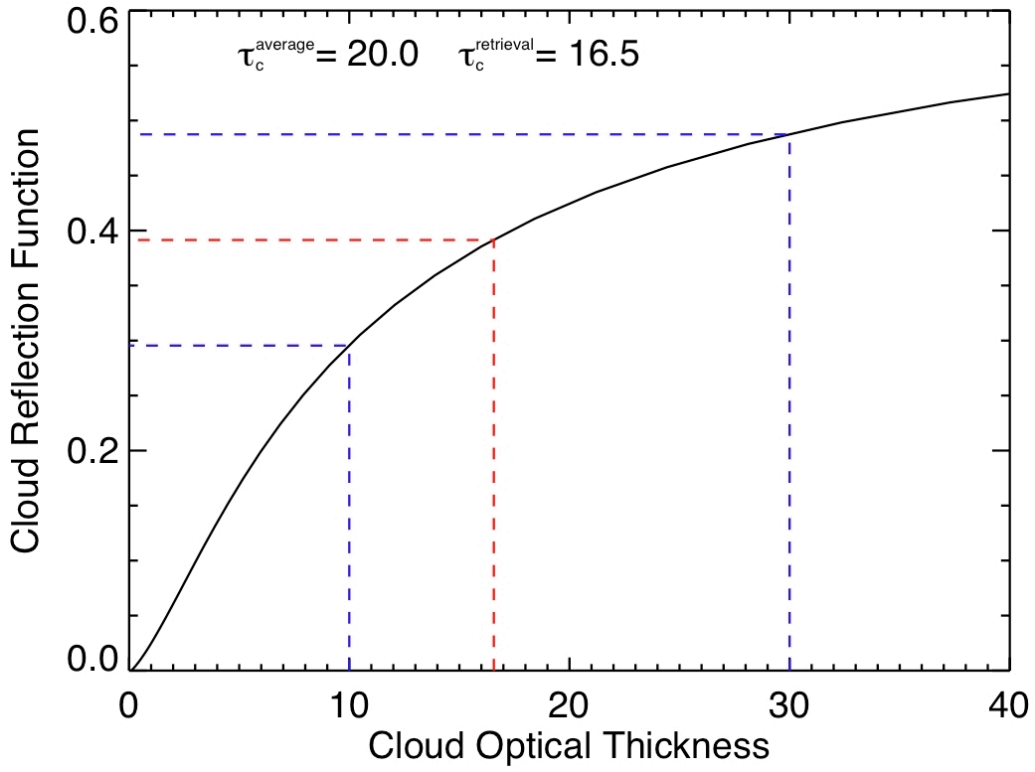

Figure 4.11 A schematic of the "plane-parallel albedo bias". The black line indicates the relationship between cloud reflection function and cloud optical thickness ($R_c - \tau_c$ relationship). Assuming a cloud scene with an optical thickness distribution consisting of two values, 10 and 30, the dashed red line indicates the retrieval based on the averaged reflection function. Because of the nonlinear nature of $R_c - \tau_c$ relationship, the retrieval is smaller than the arithmetic mean of the optical thickness distribution.

2) Uncertainty associated with cloud effective radius in POLDER retrieval.

As introduced in section 4.1, because of the lack of ice absorbing band such as the 2.11-μm band of MODIS, POLDER lacks the ability to retrieve the effective radius (r_e) of cirrus clouds. For this reason, there exists an uncertainty associated with r_e in POLDER cloud optical thickness retrieval and it may play a role in causing the difference between POLDER and MODIS retrievals. The significance of this uncertainty depends on the extent to which POLDER IHM model represents the nature of cirrus clouds in terms of cloud effective radius. Fig. 4.12 shows the histogram of cloud effective radius of the cirrus clouds in the selected granule according to MODIS cloud product. Evidently from the figure, the distribution of r_e is close to a normal distribution with a mean value of 28.18 μm and standard deviation of 10.43 μm. The histogram of r_e suggests that the uncertainty associated with r_e in POLDER cirrus optical thickness retrieval is unlikely to cause severe bias, but random errors, because the difference between the r_e of IHM model (30 μm) and the mean value (28.18 μm) of MODIS retrieval is small in comparison the with standard deviation of r_e (10.43 μm).

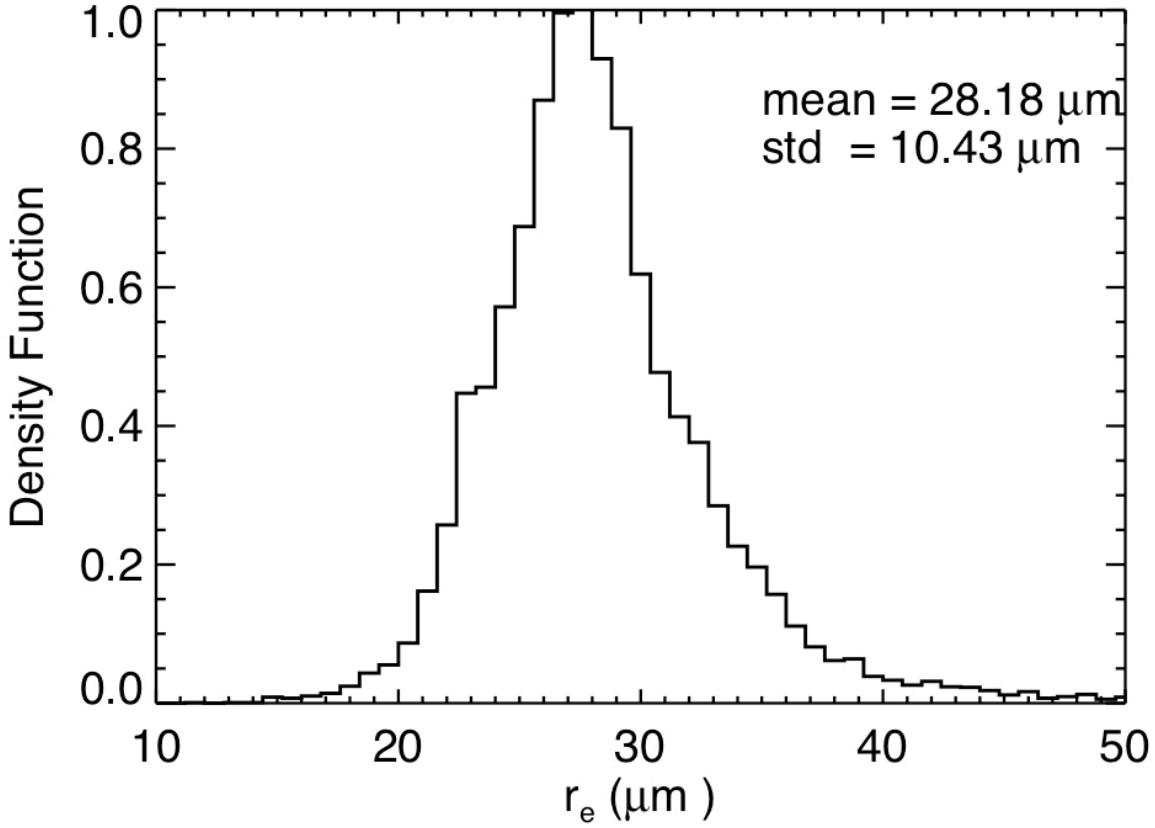

Figure 4.12 Histogram of the cloud effective radius (r_e) of cirrus clouds in the selected granule retrieved by MODIS. The density function has been normalized with respect to its maximum value.

3) Difference in cirrus bulk scattering model. As introduced in section 4.1, the MODIS cirrus cloud optical thickness retrieval is based on the Bum05 cirrus bulk scattering model, while the POLDER retrieval is based on the IHM model. Among others, one of the most important differences between the Baum05 and IHM model is in the asymmetry factor in 0.86 μm band used for both POLDER and MODIS τ_c retrieval. Fig. 4.13 shows the asymmetry factors in the 0.86 μm band as a function of cloud effective radius according to Baum05 (solid line with asterisks). For the sake of comparison, the asymmetry factor according to the

IHM is also plotted (open diamond). Two features are evident. Firstly, the asymmetry factor according to IHM model is substantially smaller that according to the Baum05 model. Secondly, according to the Baum05 model asymmetry factor in the 0.86 μm band increases with cloud effective radius linearly.

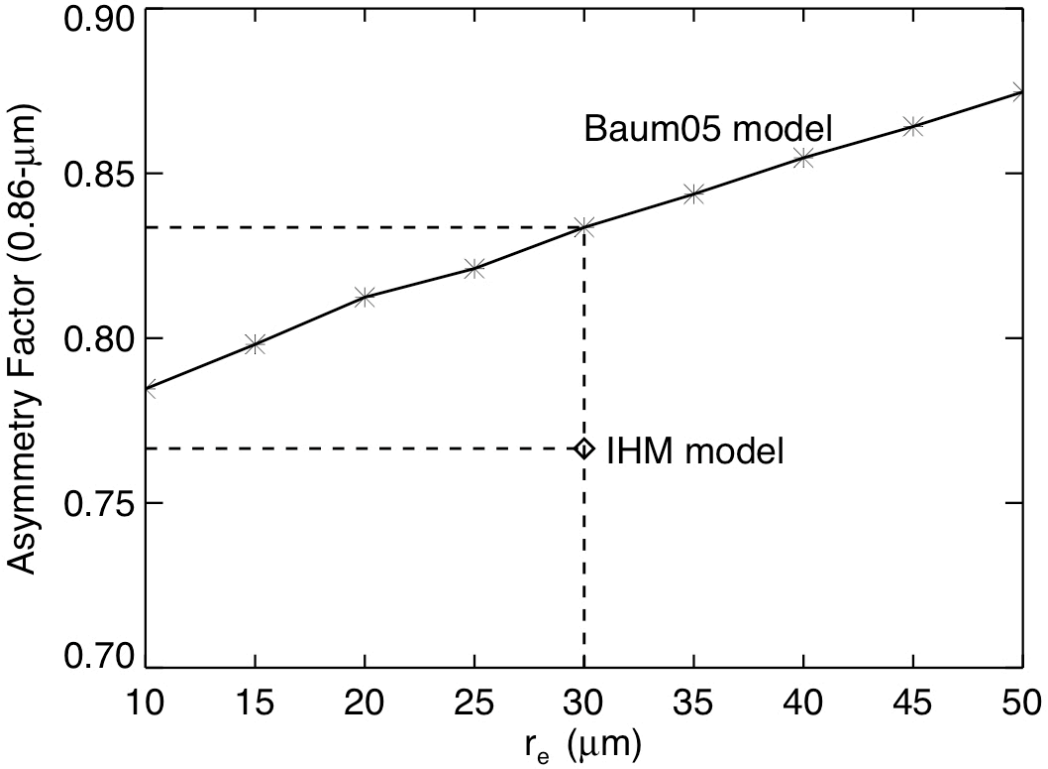

Figure 4.13 Asymmetry factors of cirrus cloud for the wavelength of 0.86 μm as a function of cloud effective radius. The black line with asterisks denotes the Baum05 model and the diamond corresponds to the IHM model.

Asymmetry factor plays an important role in determining cloud reflection function, as it denotes the ratio of forward scattering to backscattering. Indeed, it has been shown that reflection properties of optically thick layers depend primarily on the "scaled cloud optical thickness", τ'_c, although the details of the

single scattering phase function affect the directional reflectance of the cloud layer (King 1987). The scaled optical thickness is defined as follows (King 1987):

$$\tau'_c = (1 - \omega g)\tau_c . \tag{4.7}$$

In a nonabsorbing band such as the 0.86 μm band, ω is unity and the above equation reduces to:

$$\tau'_c = (1 - g)\tau_c . \tag{4.8}$$

The above equation indicates that cirrus clouds based the IHM model are more reflective than those based the Baum05 model under the same conditions (i.e. same optical thickness), which may be an important reason why τ_c^{POLDER} is substantially smaller than τ_c^{MODIS}.

To identify the relative importance of the above three reasons, the following three experiments have been performed and compared. Table 4.1 described the configurations of these experiments. Lambertian surface has been assumed in all experiments. The surface reflectance is determined from the observations in the clear-sky region. The effects of atmospheric gases such as water vapor and ozone have been neglected, because their absorption and scattering (i.e., Rayleigh scattering) are very weak in the 0.86 μm band.

Table 4.1 Configurations of three experiments

Experiment	Radiance source	Radiance resolution	Bulk scattering model
A	MODIS	6 × 6 km^2	Baum05 ($r_e = 30\mu m$)
B	POLDER	6 × 6 km^2	IHM ($r_e = 30\mu m$)
C	POLDER	6 × 6 km^2	Baum05 ($r_e = 30\mu m$)

The objective of experiment A is to investigate the impact on retrieved optical thickness of using a constant cloud effective radius in MODIS retrieval. The value 30μm is chosen here because it is close to both the mean value of the effective radius from MODIS cloud product (see Fig. 4.12) and that of the IHM model. Fig. 4.14 shows comparison of cirrus optical thickness between the results from experiment A (τ_c^A) and the MODIS operational retrieval averaged to 6 × 6 km^2 resolution (τ_c^{MODIS}). In Fig. 4.14a, $\tau_c^A / \tau_c^{MODIS}$ also appears to follows the log-normal distribution. The mean, median and standard deviation of $\tau_c^A / \tau_c^{MODIS}$ are 0.987, 0.985 and 0.332, respectively. The cumulative distribution function at $\tau_c^A / \tau_c^{MODIS} = 1$ is 52%. It is obvious from the comparison that results from experiment A is in very good agreement with τ_c^{MODIS}, indicating that the use of a constant effective radius close to the mean value of r_e has moderate impact on cirrus optical thickness retrieval. The primary reason for this is the linear dependence of the asymmetry factor on cloud effective radius, shown in Fig. 4.13.

The comparison between experiments A and MODIS retrieval suggests that the uncertainty associated with cloud effective radius in POLDER retrieval is unlikely to be the leading reason causing the difference between τ_c^{MODIS} and τ_c^{POLDER}.

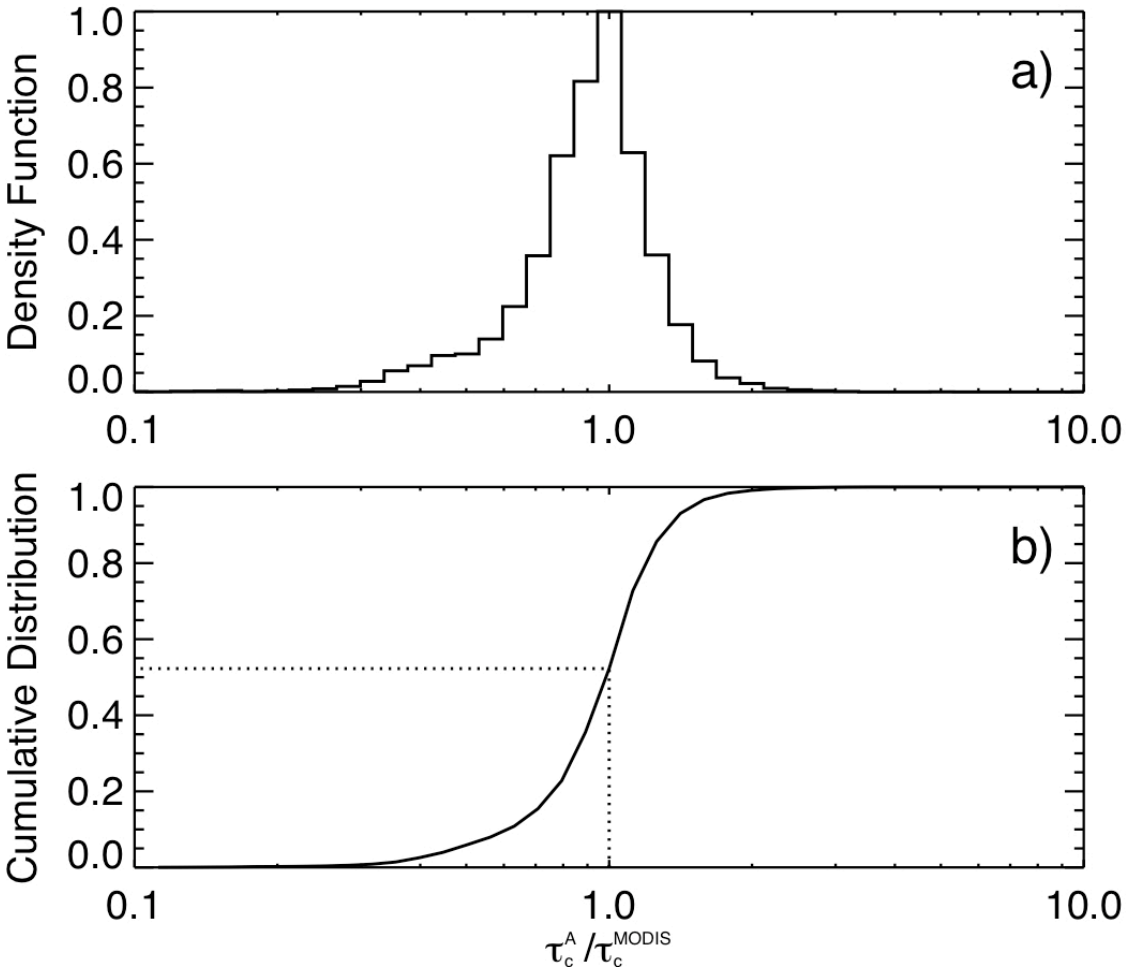

Figure 4.14 Same as Fig. 4.10 for the ratio $\tau_c^A / \tau_c^{MODIS}$.

The objective of experiment B is to test the hypothesis that the plane-parallel albedo bias is the primary reason for the difference between τ_c^{MODIS} and τ_c^{POLDER}. Fig. 4.15 shows the comparison between experiment A and B. Note that radiance observations at the resolution of 6 × 6 km^2 are used for optical thickness retrieval in both experiments. Therefore, the uncertainty caused by plane-parallel albedo bias does not play a role here. Evidently from Fig. 4.15, τ_c^B, which is retrieved from 6 × 6 km^2 POLDER radiance, is substantially smaller than τ_c^A retrieved from MODIS radiance observations with the same resolution. A comparison of Fig. 4.15 and Fig. 4.10 reveals clearly that the statistics of τ_c^B / τ_c^A is in good agreement with that of $\tau_c^{POLDER} / \tau_c^{MODIS}$, except that the standard deviation of τ_c^B / τ_c^A (0.38) is significantly smaller than that of $\tau_c^{POLDER} / \tau_c^{MODIS}$ (0.94). Therefore, the results suggest that the plane-parallel albedo bias is unlikely to play a major role in the difference between τ_c^{MODIS} and τ_c^{POLDER}.

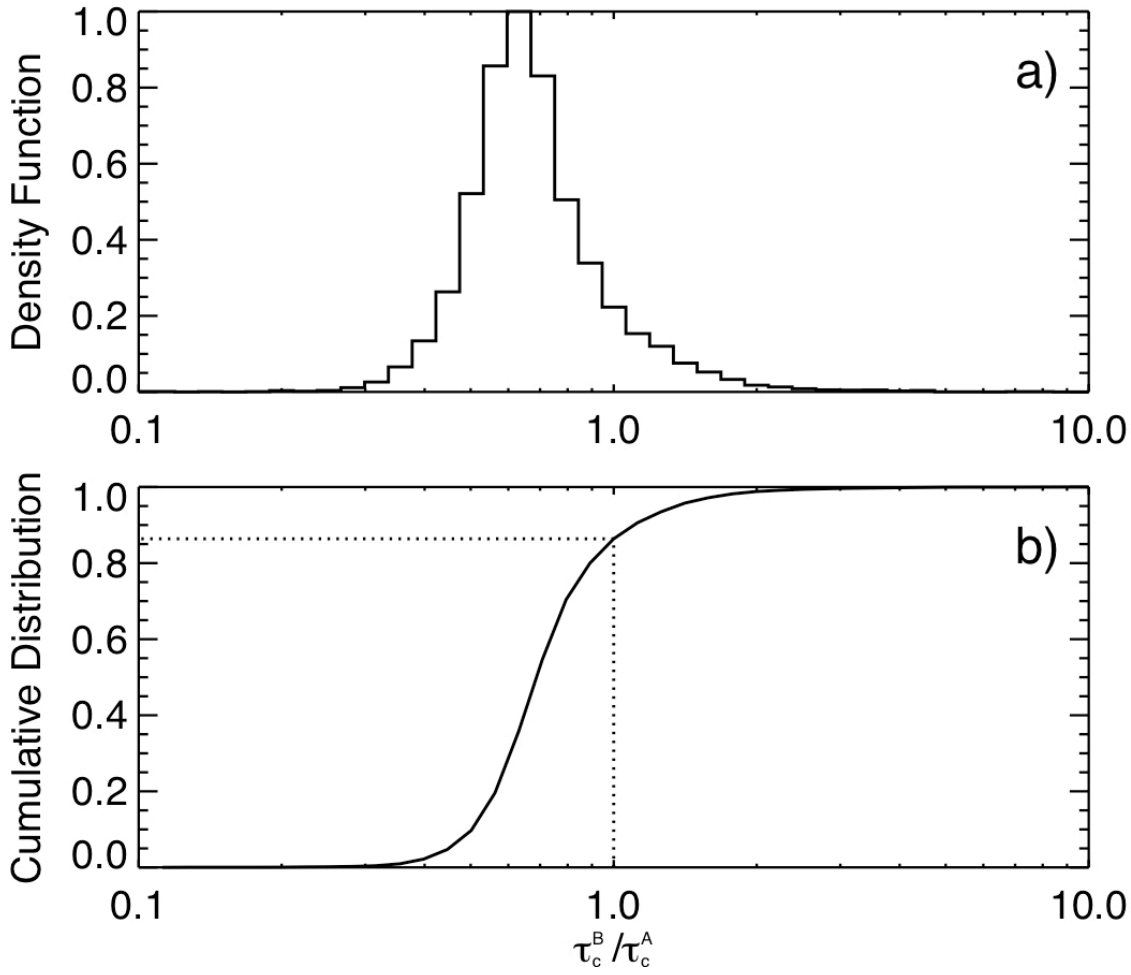

Figure 4.15 Same as Fig. 4.10 for the ratio τ_c^B / τ_c^A

In the experiment C, the Baum05 model ($r_e = 30\mu m$), instead of the IHM, is used for POLDER retrieval. Thus, the only difference between experiment C and experiment A is the source of observation, i.e., POLDER radiance observations at the resolution of 6 × 6 km^2 are used in the experiment C, while MODIS observations at the same resolution are used in the experiment A. Fig. 4.16 shows the comparison of τ_c^C and τ_c^A. Evidently, the two agree with each other closely. The good agreement between τ_c^C and τ_c^A indicates that, based on the

same assumption of cirrus cloud bulk scattering properties, PODLER and MODIS yield similar cirrus optical thickness retrievals.

To summarize the findings from the above-descried experiments and comparisons, the statistics of $\tau_c^{POLDER}/\tau_c^{MODIS}$, $\tau_c^{A}/\tau_c^{MODIS}$, τ_c^{B}/τ_c^{A}, τ_c^{C}/τ_c^{A} are collected in Table 4.2. A pixel-to-pixel comparison of collocated POLDER and MODIS cirrus cloud optical thickness retrievals reveals that for about 80% of collocated pixels τ_c^{POLDER} is smaller than τ_c^{MODIS} ($C(1.0)$=80.53%) and for half of the collocated pixels τ_c^{POLDER} is smaller than τ_c^{MODIS} by more than 37% (i.e., median of $\tau_c^{POLDER}/\tau_c^{MODIS}$ is 0.6287). A comparison of experiment A and MODIS operational retrieval tests and rejects the hypothesis that uncertainty associated with cloud effective radius in POLDER retrieval plays a major role causing the difference in τ_c^{POLDER} and τ_c^{MODIS}. Results from experiments B suggests that plane-parallel albedo bias is unlikely to be the leading reason for the difference in τ_c^{POLDER} and τ_c^{MODIS}. A comparison of experiment C and A shows that based on the same cirrus bulk scattering model, MODIS and POLDER yield very similar cirrus cloud optical thickness retrievals.

The above findings have made it clear that the difference in operational MODIS and POLDER cirrus cloud optical thickness retrievals is mainly caused by the fact that different assumptions of the bulk scattering properties of cirrus cloud have been used in MODIS and POLDER retrievals. The underlying physics is that, under the same conditions (i.e., same optical thickness), cirrus clouds based on the Baum05 model are more reflective than based on the IHM model.

This difference in cloud reflection results in substantial difference in cirrus cloud optical thickness retrieval between MODIS and POLDER.

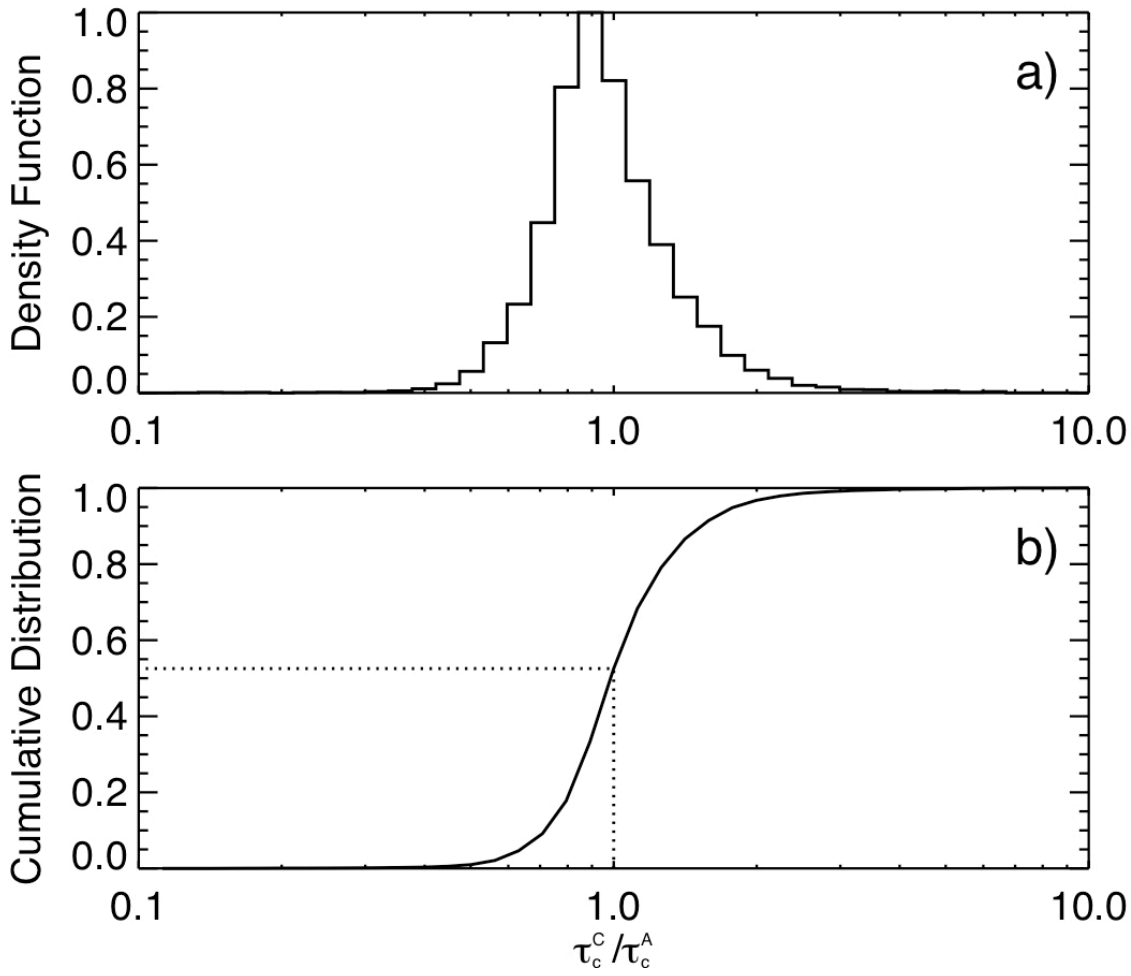

Figure 4.16 Same as Fig. 4.10 for the ratio τ_c^C / τ_c^A

Table 4.2 Statistics of the ratios, $\tau_c^{POLDER} / \tau_c^{MODIS}$, $\tau_c^A / \tau_c^{MODIS}$, τ_c^B / τ_c^A and τ_c^C / τ_c^A.

Comparison	Distribution	Mean	Median	Std	C(1.0)
$\tau_c^{POLDER} / \tau_c^{MODIS}$	Log-normal	0.8082	0.6827	0.9483	80.53%
$\tau_c^A / \tau_c^{MODIS}$	Log-normal (normal)	0.9870	0.9845	0.3323	52.26%
τ_c^B / τ_c^A	Log-normal	0.7703	0.6879	0.3802	86.38%
τ_c^C / τ_c^A	Log-normal (normal)	1.0880	0.9851	0.5109	52.53%

4.3. Implications for climate studies

As mentioned in the introduction, the radiative effects of cirrus clouds depend on many parameters, among which cloud microphysics and optical thickness are two crucial ones (Jensen et al. 1994). It is shown in the last section that there currently exists a large divergence in our understanding of the microphysics and consequently optical thickness of cirrus clouds. Some intriguing and important questions immediately arise from these differences. What are the consequences of these differences, in terms of understanding the radiative effects, especially the shortwave forcing, of cirrus clouds? More specifically, how is shortwave radiative forcing (F_{SW}) of cirrus clouds based on MODIS retrieval τ_c^{MODIS} different from that based on POLDER retrieval τ_c^{POLDER}? Whether and how could the difference in F_{SW} lead to different understanding of the role of cirrus clouds in climate?

To seek answers to these questions, an investigation of the sensitivity of cirrus shortwave radiative forcing to the microphysics and optical thickness of cirrus clouds has been carried out. In this investigation, two sets of cirrus shortwave radiative forcing in the region 30^o N to 30^o S in the year 2006 have been computed. One is based on the MODIS monthly mean cloud product (MOD08_M3) and the Baum05 model. The other is based on POLDER monthly mean cloud product (RB3) and the IHM model. The computation is carried out using a comprehensive solar radiation model developed by Chou et al. (Chou 1992). It must be pointed out that the objective here is not to derive the real cirrus shortwave radiative forcing, which is a complicated and challenging task beyond the scope of this study. Instead, we are only interested the difference between MODIS-based and POLDER-based cirrus shortwave radiative forcing under the same conditions. For this reason, the computations are performed in a relatively simple scenario. Specifically, the monthly mean solar zenith angles without diurnal variation are used in the computation and cirrus cloud is assumed to locate between 175 and 225 mb. As aforementioned, the optical thickness of cirrus clouds is based on MODIS or POLDER products. The corresponding bulk scattering parameters, i.e., the singe-scattering albedo and asymmetry factor, are based on the Baum05 or IHM model.

Fig. 4.17 shows the zonal, monthly mean of optical thickness of cirrus clouds from 30^o N to 30^o S in the year 2006, observed from MODIS (left panel) and POLDER (right panel). Two features are evident in Fig. 4.17. Firstly, the optical thickness of cirrus clouds shows a strong seasonal variation. Secondly,

POLDER observations are substantially smaller than those from MODIS. Fig. 4.17 shows that, not only for the granule shown in the last section, the substantial difference between MODIS and POLDER cirrus optical thickness retrievals (i.e., POLDER retrieval is smaller than MODIS) is also seen on a much larger scale.

Fig. 4.18 shows the cloud shortwave radiative forcing (F_{SW}) due to cirrus clouds derived from MODIS (left panel) and PODLER (right panel) observations. The definition of F_{SW} is defined as (Ramanathan et al. 1989)

$$F_{SW} = F_{SW}^{cloudy} - F_{SW}^{clear}, \tag{4.9}$$

where F_{SW}^{cloudy} and F_{SW}^{clear} denote the downward shortwave flux at the top of atmosphere (TOA) with and without the presence of cirrus clouds, respectively. As expected, the shortwave radiative forcing is highly correlated to the optical thickness of cirrus cloud. A comparison of Fig. 4.17 and Fig. 4.18 reveals that the difference between MODIS-based and POLDER-based F_{SW} is much smaller that that between MODIS-based and POLDER-based τ_c. Indeed, as illustrated in Table 4.3, the annual area-averaged cirrus optical thickness according to POLDER (7.822) over the region is smaller than that according to MODIS (13.137) by about 40%. However, the difference in annual area-averaged F_{SW} between MODIS and POLDER is within only 10%.

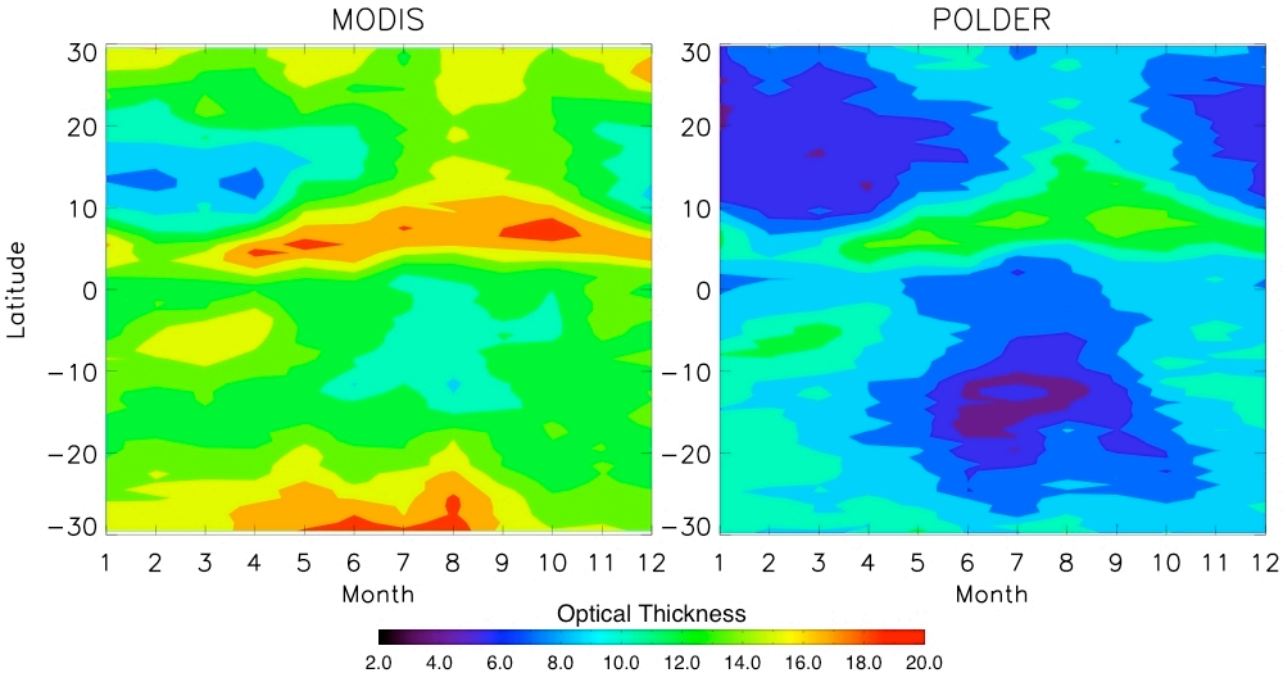

Figure 4.17 The left panel shows the zonal mean optical thickness of cirrus clouds in the region 30^{o} N to 30^{o} S as function of moth in the year 2006 retrieved by MODIS. The right panel shows the corresponding retrieval from PODLER.

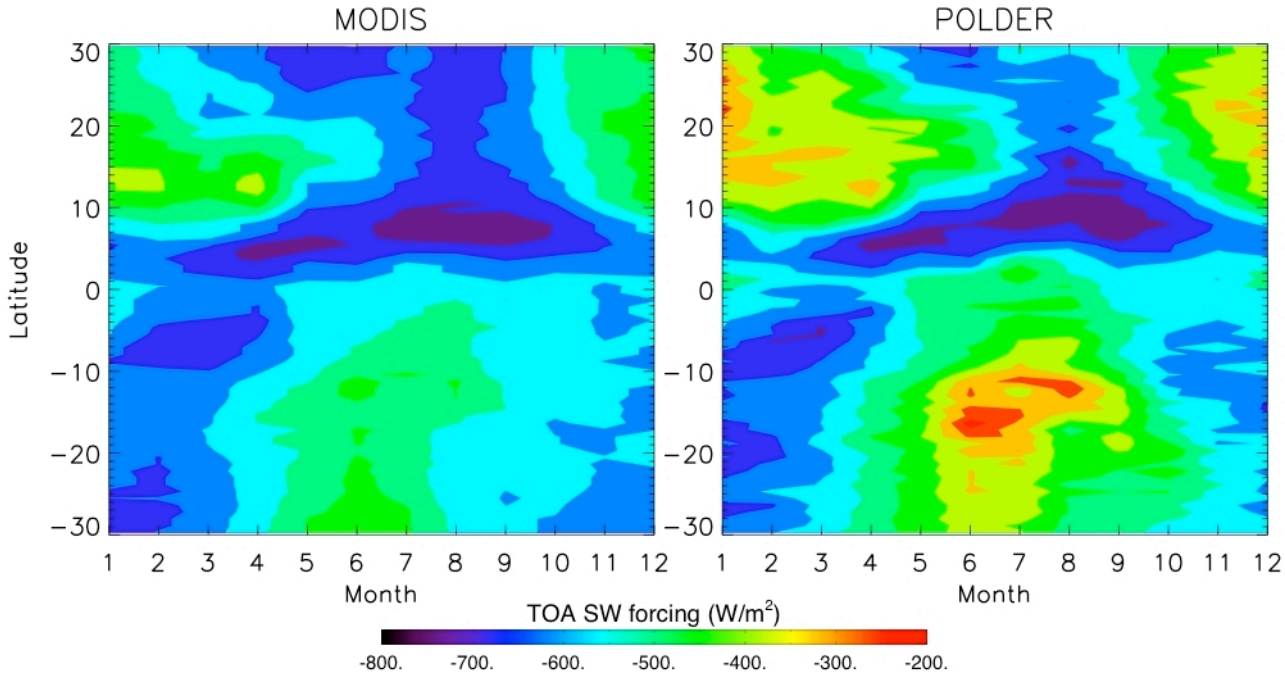

Figure 4.18 This figure shows the shortwave cirrus radiative forcing calculated based on the MODIS optical thickness retrieval + Baum05 model (left panel) or POLDER retrieval + IHM model (right panel).

Table 4.3 Annual area-averaged τ_c and corresponding F_{sw} according to different model set-ups. The numbers in the brackets denote relative differences with respect to the case in which MODIS τ_c retrieval and Baum05 model are used in the radiative transfer model.

	Annual area-averaged τ_c	Annual area-averaged F_{sw} (W/m^2)
MODIS τ_c Baum05 model	13.137	-570.178
POLDER τ_c IHM model	7.822 (-40.456%)	-519.068(-8.963%)
POLDER τ_c Baum05 model	7.822 (-40.456%)	-427.207 (-25.074%)

The above sensitivity study has shown that, although there exists a substantial difference between POLDER and MODIS cirrus cloud optical thickness retrievals, the shortwave radiative forcings of cirrus clouds derived from the two retrievals are actually in good agreement (different only by about 9%). The reason for this agreement is probably due to the cancellation of the difference in optical thickness retrievals by the difference in bulk scattering model, more specifically, the asymmetry factor. As aforementioned, IHM model is more reflective than the Baum05 model for the same optical thickness, due to the fact that the asymmetry factor of the former is substantially smaller than the latter. As a result, although τ_c^{POLDER} is substantially smaller than τ_c^{MODIS}, cirrus shortwave radiative forcing based on MODIS retrieval and the Baum05 model is quite similar to that based on POLDER retrieval and IHM model. To make this point more clearly, we have also computed the F_{SW} using the combination of POLDER optical thickness retrieval and the Baum05 model, in which case the above-described cancellation is not possible. As shown in Table 4.3, the annual

area-averaged F_{SW} corresponding to this combination is -427.207 W/m^2, more than 25% smaller than that based on the combination of MODIS retrieval plus the Baum05 model.

In summary, it is shown through the above sensitivity study that due to the cancellation of the difference in τ_c retrievals by the difference in asymmetry factor, F_{SW} based on POLDER cloud product plus the IHM cirrus bulk scattering model is in good agreement with its MODIS counterpart. However, the cancellation is not ideal, as there still exists about 10% relative difference of F_{SW} .

4.4. Implications for the development of future cirrus cloud retrieval algorithms

As previously mentioned, the VIIRS (Visible Infrared Imager Radiometer Suite) is one of the key instruments on board of the next generation of polar orbiting satellite system of United States—the NPOESS (National Polar Orbiting Satellite System) (Miller et al. 2006). Global observations of cloud, including cirrus, properties in the NPOESS era will reply heavily on the VIIRS, which makes the development of a reliable cirrus cloud retrieval algorithm for VIIRS crucially important.

One of the difficulties in the development of cirrus cloud retrieval algorithm is the selection of cirrus bulk scattering model. As previously shown in the section 4.2, different assumptions of cirrus bulk scattering properties may lead to substantially different cirrus optical thickness retrievals. For this reason, one of the outstanding issues receiving increasing attention from cirrus remote sensing

community is whether the scattering phase function of cirrus cloud in the shortwave region, such as the 0.86μm band, is smooth and featureless as similar to the IHM model, or featured with strong scattering peaks as similar to the Baum05 model (see Fig. 4.3). Although several recent studies have shown some evidences in favor of the featureless phase function (e.g., C.-Labonnote et al. 2001; Baran and Labonnote 2006; Knap et al. 2005), this issue remains rather controversial and requires further investigations.

Our objective here, however, is not to seek answers to this issue. Instead, we would like to bring attention to a potential uncertainty relevant to the above issue in deriving the seasonal variations of cirrus cloud optical thickness and shortwave radiative forcing from MODIS radiance measurements.

In section 4.2, the effects of cirrus bulk scattering model on cirrus optical thickness retrieval have been investigated through a comparison of collocated POLDER and MODIS cloud products. However, the focus has been mainly set to on the asymmetry factor and its effects on the overall statistics of cirrus optical thickness retrieval (e.g., median value). Several recent studies (e.g., C.-Labonnote et al. 2001; Baran and Labonnote 2006; Knap et al. 2005) have noticed that optical thickness retrievals based on different cirrus scattering phase functions can be substantially different. Moreover, it has been shown the difference depends sensitively on the sun-satellite viewing geometry, or, more specifically, the scattering angle (θ_s). To illustrate this point, we have performed two optical thickness retrievals for the granule in Fig. 4.5. Both retrievals are based on MODIS radiance observations. However, the Baum05 model with

$r_e = 30\mu m$ is employed in one retrieval and the IHM model in the other. Hereafter, the two retrievals will be referred to as τ_c^{Baum05} and τ_c^{IHM}, respectively. Fig. 4.19 shows $\tau_c^{\text{IHM}} / \tau_c^{\text{Baum05}}$ as a function of scattering angles. Two features in Fig. 4.19 are worth mentioning here. First of all, τ_c^{IHM} is substantially smaller than τ_c^{Baum05}, which is largely attributed to the difference in asymmetry factor between the IHM and Baum05 model. Secondly, and more importantly here, it is evident that the difference between τ_c^{IHM} and τ_c^{Baum05} depends sensitively on θ_s.

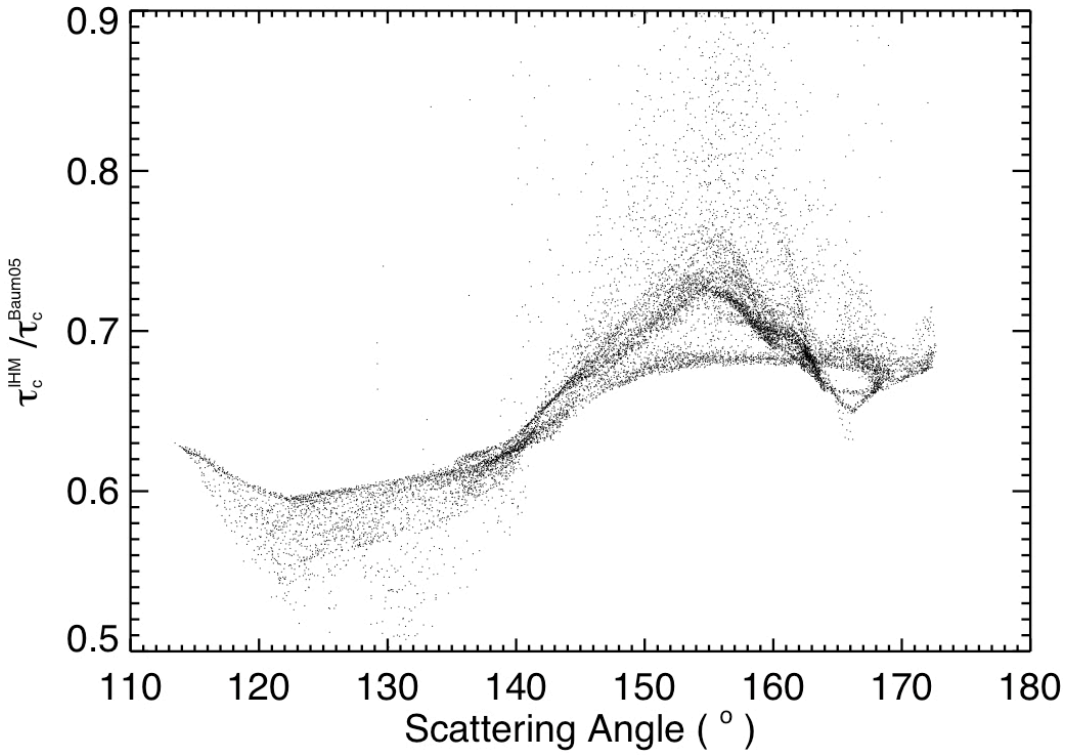

Figure 4.19 The ratio of $\tau_c^{\text{IHM}} / \tau_c^{\text{Baum05}}$ versus scattering angle**.**

Because MODIS angular scan pattern (Salomonson et al. 1989) remains same for all seasons, the statistics of θ_s corresponding to sun-MODIS viewing

geometry (see Eq. (4.3)), for example the mean value, depend closely on the position of the Sun. As schematically illustrated in Fig. 4.20, θ_s increases as solar zenith angle (θ_0) decreases from winter to summer and then decreases as the Sun returns to its winter position. This seasonal variation of MODIS θ_s is clearly seen in Fig. 4.21 showing the map of the zonal mean MODIS θ_s over the region 30^o N to 30^o S as a function of month.

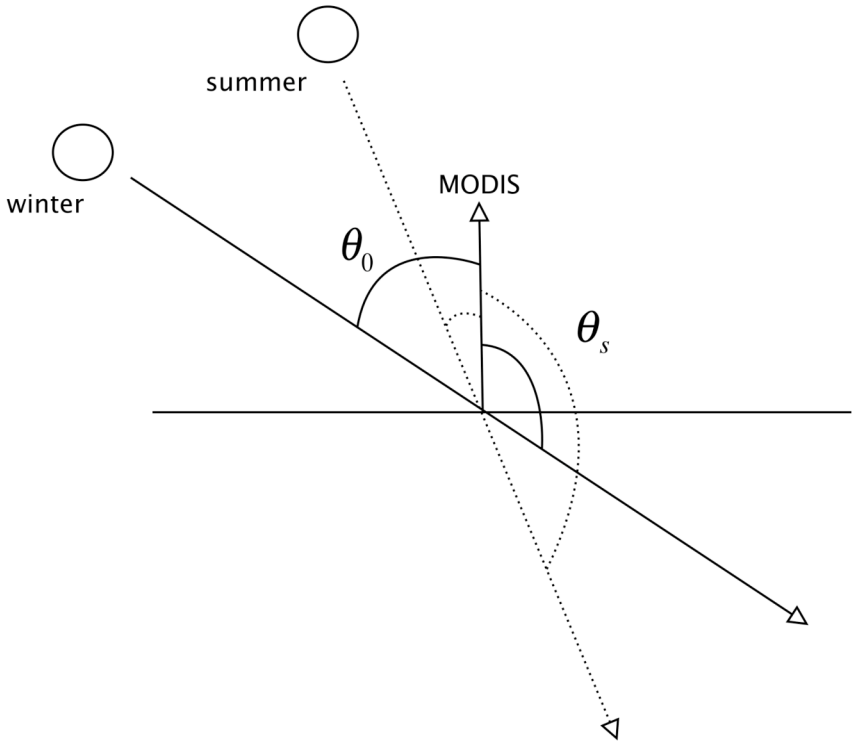

Figure 4.20 A schematic of seasonal variation of MODIS scattering angle. In the figure, θ_0 denotes the solar zenith angle and θ_s denotes the scattering angle**.**

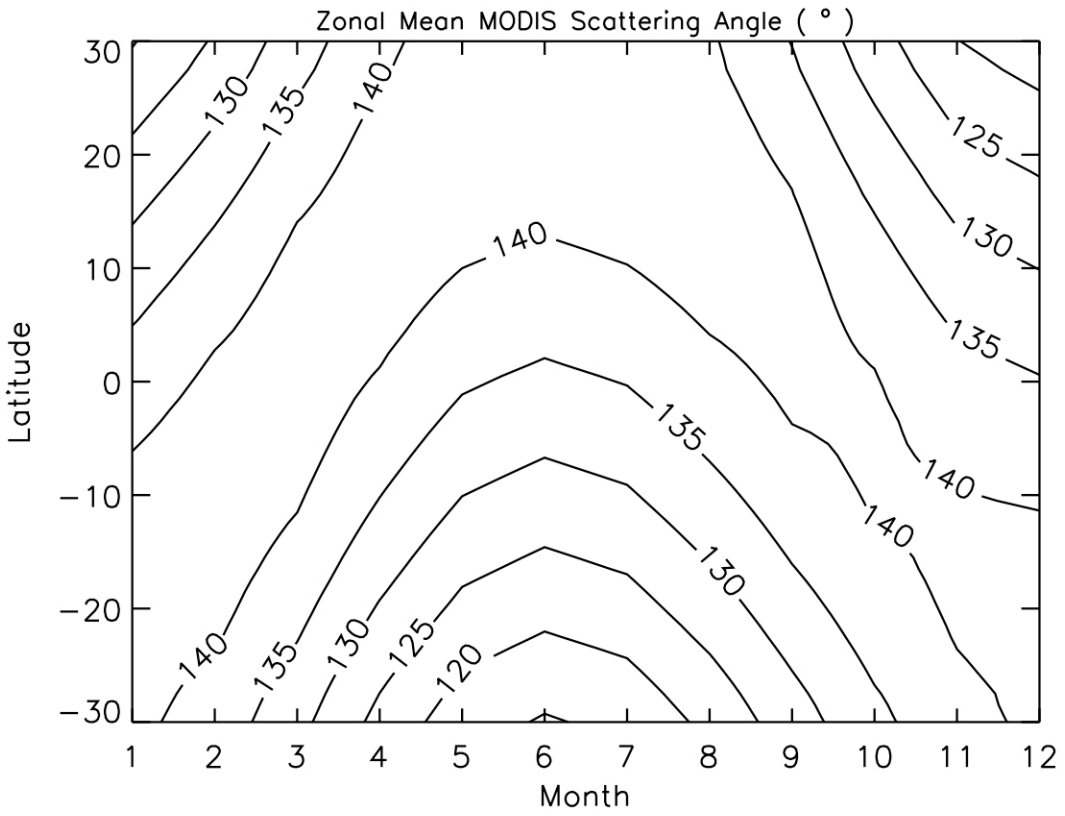

Figure 4.21 Zonal mean MODIS scattering angle as a function of month.

The dependence of $\tau_c^{\mathrm{IHM}} / \tau_c^{\mathrm{Baum05}}$ on θ_s shown Fig. 4.19 together with the seasonal variation of MODIS scattering angle shown in Fig. 4.21 have an interesting and important implication for deriving seasonal variation of cirrus optical thickness from MODIS and the future VIIRS measurements. This implication is illustrated in the following example. Assume that cirrus cloud at the latitude of 10^o N has a constant optical thickness equal to 7.0, which is close to the annual area-averaged POLDER τ_c retrieval in the region 30^o N to 30^o S (see Table 4.3). Let's further assume that the bulk scattering properties of cirrus clouds at this latitude follow the IHM model. In other words, if the MODIS retrieval algorithm were based on the IHM model, the retrieved optical thickness from

MODIS would be close to the real value, i.e., 7.0. However, because of the use of the Baum05 model in the retrieval, the MODIS τ_c actually follows the solid line in Fig. 4.22a.

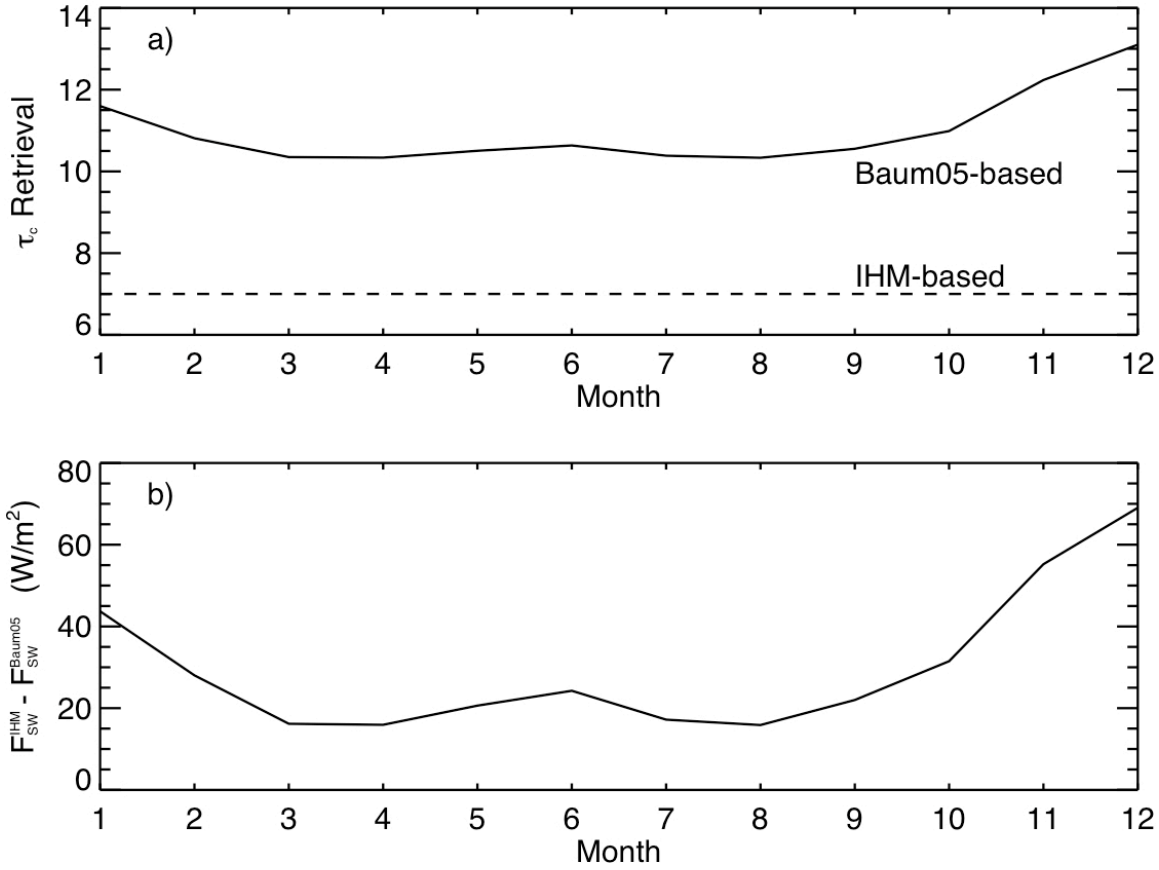

Figure 4.22 This figure illustrates schematically an example of the uncertainty caused by the use of an incorrect cirrus bulk scattering properties in deriving the seasonal variations of cirrus optical thickness and shortwave radiative forcing from MODIS radiance observations. Assuming that cirrus clouds at 10^o N have a constant optical thickness, say 7.0, and their bulk scattering properties follow the IHM model, the dashed line in a) denotes the optical thickness retrieval based on the IHM model and soiled line denotes the retrieval based on the Baum05 model. The difference in derived shortwave radiative forcing between Baum05-based and IHM-based retrieval is shown in b).

First of all, it is obvious that optical thickness retrieval based on the Baum05 model is substantially larger than the real value. As aforementioned, this

is largely due to the difference in the asymmetry factor between the IHM and Baum05 model. Another interesting feature is that Baum05-based retrievalshows a clear seasonal variation, in spite of the fact that the real value assumed in this case is a constant with no seasonal variation. Indeed, based on the Baum05 model, the DJF mean of cirrus optical thickness retrieval is 12.3, while the JJA mean is 10.5, about 20% difference. The reason for this artificial seasonal variation is as follows. As shown in Fig. 4.21, the mean MODIS scattering angle at the latitude 10^o N changes from about 132^o to over 140^o, from winter to summer as the Sun becomes higher in the sky, and then back to smaller value as winter comes, reaching the minimum value of about 130^o in December. If Fig. 4.19 is put in this context, it is not difficult to find that, as a result of this seasonal variation of MODIS scattering angle, the difference between Baum05-based and IHM-based cirrus optical thickness retrievals, i.e., $\tau_c^{\mathrm{IHM}} / \tau_c^{\mathrm{Baum05}}$, also varies with season. That is, the difference is larger (i.e., $\tau_c^{\mathrm{IHM}} / \tau_c^{\mathrm{Baum05}}$ is more smaller than unity) in winter than in summer. Because a constant value is assumed in this case for the IHM-based retrieval, the above seasonal cycle of $\tau_c^{\mathrm{IHM}} / \tau_c^{\mathrm{Baum05}}$ becomes a shift of τ_c^{Baum05}, which is clearly seen in Fig. 4.22a.

The above example has shed a light on a potential uncertainty, which has been largely overlooked in previous studies, in deriving the seasonal variation of cirrus optical thickness from MODIS observation. That is, the use of an unrealistic cirrus bulk scattering model may lead to artificial seasonal variation in MODIS cirrus cloud optical thickness retrieval. Moreover, and more importantly, this unrealistic seasonal variation in τ_c retrieval may lead to unrealistic seasonal

variation of cirrus radiative forcing, too. Fig. 4.22b shows the difference between the IHM-based (F_{SW}^{IHM}) and Baum05-based (F_{SW}^{Baum05}) cirrus shortwave radiative forcing. It is evident that the difference shows clearly a seasonal variation correlated to the difference between τ_c^{IHM} and τ_c^{Baum05}.

Now, it is worth going back to Fig. 4.19 again to explain physics behind this artificial seasonal variation in cirrus optical thickness retrieval. As aforementioned, τ_c^{IHM} and τ_c^{Baum05} are different in two respects: Firstly, τ_c^{IHM} is substantially smaller than τ_c^{Baum05} as the mean value of the ratio $\tau_c^{\mathrm{IHM}} / \tau_c^{\mathrm{Baum05}}$ is substantially smaller than unity (hereafter referred to as the "mean value difference"). Secondly, the difference between τ_c^{IHM} and τ_c^{Baum05} depends sensitively on scattering angle (hereafter referred to as the "θ_s-dependent difference"), which is the reason for the artificial seasonal variation in τ_c retrieval. It is shown in section 4.3 that the "mean value difference" between τ_c^{IHM} and τ_c^{Baum05} (i.e. the mean value of $\tau_c^{\mathrm{IHM}} / \tau_c^{\mathrm{Baum05}}$) is mainly attributed to the difference in the asymmetry factor, i.e., the first moment of scattering phase function, between the IHM and Baum05 model. On the other hand, the "θ_s-dependent difference" is the result of the difference between the IHM and Baum05 model in high-order moments of scattering phase function. Note that, in cloud radiative forcing computation, only the first, i.e., the asymmetry factor, or, at most, the second order moment of the scattering phase function is involved, depending on whether the two-stream or four-stream radiative transfer scheme is employed for the computation. For this reason, as long as the "right" asymmetry factor is used

(i.e., Baum05 asymmetry factor for Baum05-based retrieval and IHM asymmetry factor for IHM-based retrieval) the annual area-averaged F_{SW} derived from the Baum05-based retrieval is largely in agreement with that from the IHM-based retrieval. However, the "θ_s-dependent difference" remains and leads to the unrealistic seasonal variation of shortwave radiative forcing of cirrus clouds seen in Fig. 4.22b, even if the "right" asymmetry factor is used, because it is associated with the uncertainty in high-order moment of scattering phase function.

Finally, we would like to point out that cares should be taken not to over-interpret the above findings for the following reasons.

1) Because our objective here is to bring attention to a potential uncertainty in the estimation of, rather than assessing the actual, seasonal variation of cirrus radiative forcing, computations in this study are done in a relatively simple scenario. Further detailed investigations are needed to understand the true importance of this uncertainty.

2) Due to the lack of ice-absorbing bands of POLDER, the effects of cloud effective radius on cirrus optical thickness retrieval and cloud radiative forcing have been largely neglected in this study. It is the reason that a constant effective radius, 30 μm, has been assumed in Fig. 4.19 and 4.22. Note that the effective radius has a significant influence on the asymmetry factor (see Fig. 4.13), which in turn significantly affects cirrus optical thickness retrieval. Therefore, the uncertainty caused by the use of constant effective radius in optical thickness retrieval, i.e., Fig. 4.22a, may be significant. However, it must

be kept in mind that the use of constant effective radius also causes uncertainty in asymmetry factor in radiative forcing computations. And, as analyzed previously, the two uncertainties, one associated with optical thickness retrieval and the other with asymmetry factor, tend to cancel each other in radiative forcing computations. For this reason, the uncertainty caused by the use of constant effective radius in radiative forcing computations may not be as important as in optical thickness retrieval. Nevertheless, further investigations are needed to understand the robustness of the finding shown in Fig. 4.22.

3) It is worth stressing again that our intention is not to argue which bulk scattering model, the Baum05 or the IHM model, represents the nature of cirrus clouds better. The results only suggest that the use of different bulk scattering models in cirrus retrieval may lead to substantially different understandings of seasonal variations of cirrus optical thickness and radiative forcing. This uncertainty should be taken into consideration in the selection of bulk scattering model for the development of future cirrus retrieval algorithms and therefore necessitates further investigations to improve our understanding of the microphysics and bulk scattering properties of cirrus clouds.

4.5. Conclusions and summary

We have collocated and compared the POLDER and MODIS cirrus cloud products for a selected MODIS granule. The comparison indicates that the optical thickness retrieval from POLDER is substantially smaller than that from MODIS. Specifically, the comparison shows that the ratio of POLDER to MODIS

cirrus optical thickness retrieval ($\tau_c^{POLDER} / \tau_c^{MODIS}$) follows the log-normal distribution and it is found that for more than 80% of the collocated pixels τ_c^{POLDER} is smaller than τ_c^{MODIS} and for half of the collocated pixels τ_c^{POLDER} is smaller than τ_c^{MODIS} by at least 30%.

Several potential reasons for the substantial difference between τ_c^{POLDER} and τ_c^{MODIS} were investigated. Through an intercomparison of a set of experiments, it is found that neither the "plane-parallel albedo bias" nor the uncertainty caused by the use of constant effective radius for cirrus clouds in POLDER retrieval contributes to the difference significantly. Instead, the results suggest that the difference between τ_c^{POLDER} and τ_c^{MODIS} is largely attributable to the difference of cirrus bulk scattering model used in MODIS and POLDER retrieval algorithms, i.e., the difference between the Baum05 and the IHM cirrus bulk scattering model.

Based on the MODIS level-3 monthly mean cloud product, we also calculated the zonal mean shortwave cirrus radiative forcing, F_{SW}^{MODIS}, in the year 2006 and in the region 30^o N and 30^o S. Comparison of F_{SW}^{MODIS} with its POLDER counterpart F_{SW}^{POLDER} indicates that the two are in reasonable agreement in spite of the substantial difference between τ_c^{POLDER} and τ_c^{MODIS}. The annual area-avenged values are different by only 9%. It is shown that this agreement is the result of the cancellation of the difference in optical thickness retrieval by the difference in asymmetry factor between the Baum05 and IHM model. Finally, we show that an unrealistic cirrus bulk scattering model might introduce artificial seasonal

variation of cirrus optical thickness and shortwave radiative forcing into the retrieval.

V. SUMMARY

In section II, based on the advantages of CHARTS, FIRTM1 and FIRTM2, we have developed a fast IR RT model based on the well-known adding-doubling principle for applications to the forward RT simulations involved in the hyperspectral remote sensing applications under cloudy-sky conditions. Because of the use of the pre-computed LUT, the computational burden associated with the doubling process is substantially alleviated in FIRTM-AD. In comparison with FIRTM1 and FIRTM2, FIRTM-AD is much more flexible and accurate. FIRTM-AD is applicable to multilayered, inhomogeneous and non-isothermal clouds. In addition, FIRTM-AD can be applied to computations at both TOA and the surface, and therefore applicable to both satellite and ground-based hyperspectral sensors. The comparisons have shown that FIRTM-AD is about 250 times faster than DISORT in the computations of BT spectra at TOA and the surface for a single-layered thin ($\tau_{vis} < 1$) cirrus cloud. The RMS BT errors of FIRTM-AD in this type of application are generally smaller than 0.05 K. For two or three-layered thick ($\tau_{vis} > 1$) cloud conditions, FIRTM-AD is still about two orders of magnitude more efficient than DISORT and the error is on the order of 0.1 K.

To obtain a better understanding of the uncertainty in FSSP ice particle measurement caused by the sphericity assumption for small ice particles, we have first computed the scattering properties of Platonic solids in section III,. Then, the single-scattering properties of the Platonic solids are compared with

those of four types of spherical equivalences that are defined in terms of (1) equal maximum dimension, (2) equal surface area, (3) equal volume, and (4) equal volume-to surface area ratio for size parameters in the geometric optics regime. The comparisons are made at two wavelengths, 0.66 μm and 11 μm, corresponding to weak and strong absorption, respectively. The comparisons show that the equal-surface-area spherical equivalence has the smallest errors in terms of the extinction cross-section for both the cases for weak and strong absorption. All spherical approximations substantially overestimate the asymmetry factor of the Platonic solids at 0.66 μm. In the case of strong absorption, spherical approximations underestimate the single-scattering albedo. The scattering phase functions of the Platonic solids at a wavelength of 0.66 μm are substantially different from that of the equivalent spheres because of the sensitivity of the phase function to particle morphological details. The phase functions of both the Platonic solids and spheres at 11 μm are quite featureless and similar because diffraction and external reflection dominate the scattered energy.

Based on the above results, we have also simulated the response of FSSP to Platonic solids and their equivalent spheres. It is found that the response of FSSP to Platonic solid is much smaller than its response to equivalent spheres. For Icosahedron and Dodecahedron, which have relatively lower asphericities (more like sphere) and probably represent the nature of small ice particles better, a-factor-of-2.5 difference is found. Therefore, our result is in support of the argument by Garrett (Garrett 2007) that the sphericity assumption

for small ice particles may lead to a-factor-of-2-to-2.5 underestimation of their extinction cross-section. It is also found that the underestimation is largely due to the difference in scattering phase function between Platonic solids and their equivalent spheres. That is, a Platonic solid tends to scatter less light, in comparison with equivalent spheres, into the directions within the FSSP collecting angles, which leads to a smaller FSSP response and consequently underestimation of its extinction cross-section.

In section IV, We have collocated and compared the POLDER and MODIS cirrus cloud products for a selected MODIS granule. The comparison indicates that the optical thickness retrieval from POLDER is substantially smaller than that from MODIS. Specifically, the comparison shows that the ratio of POLDER to MODIS cirrus optical thickness retrieval ($\tau_c^{POLDER} / \tau_c^{MODIS}$) follows the log-normal distribution and it is found that for more than 80% of the collocated pixels τ_c^{POLDER} is smaller than τ_c^{MODIS} and for half of the collocated pixels τ_c^{POLDER} is smaller than τ_c^{MODIS} by at least 30%.

Several potential reasons for the substantial difference between τ_c^{POLDER} and τ_c^{MODIS} were investigated. Through an intercomparison of a set of experiments, it is found that neither the “plane-parallel albedo bias” nor the uncertainty caused by the use of constant effective radius for cirrus clouds in POLDER retrieval contributes to the difference significantly. Instead, the results suggest that the difference between τ_c^{POLDER} and τ_c^{MODIS} is largely attributable to the difference of cirrus bulk scattering model used in MODIS and POLDER

retrieval algorithms, i.e., the difference between the Baum05 and the IHM cirrus bulk scattering model.

Based on the MODIS level-3 monthly mean cloud product, we also calculated the zonal mean shortwave cirrus radiative forcing, F_{SW}^{MODIS}, in the year 2006 and in the region 30^o N and 30^o S. Comparison of F_{SW}^{MODIS} with its POLDER counterpart F_{SW}^{POLDER} indicates that the two are in reasonable agreement in spite of the substantial difference between τ_c^{POLDER} and τ_c^{MODIS}. The annual area-avenged values are different by only 9%. It is shown that this agreement is the result of the cancellation of the difference in optical thickness retrieval by the difference in asymmetry factor between the Baum05 and IHM model. Finally, we show that an unrealistic cirrus bulk scattering model might introduce artificial seasonal variation of cirrus optical thickness and shortwave radiative forcing into the retrieval.

REFERENCES

Ackerman, T. P., K.-N. Liou, F. P. J. Valero, and L. Pfister, 1988: Heating Rates in Tropical Anvils. *J. Atmos. Sci.*, **45,** 1606-1623.

Anderson, T. L., R. J. Charlson, N. Bellouin, O. Boucher, M. Chin, S. A. Christopher, J. Haywood, Y. J. Kaufman, S. Kinne, and J. A. Ogren, 2005: An "a-Train" Strategy for Quantifying Direct Climate Forcing by Anthropogenic Aerosols. *Bull. Amer. Meteor. Soc.*, **86,** 1795-1809.

Auer, A. H. and D. L. Veal, 1970: The Dimension of Ice Crystals in Natural Clouds. *J. Atmos. Sci.*, **6,** 919–926.

Aumann, H. H., M. T. Chahine, C. Gautier, M. D. Goldberg, E. Kalnay, L. M. McMillin, H. Revercomb, P. W. Rosenkranz, W. L. Smith, and D. H. Staelin, 2003: Airs/Amsu/Hsb on the Aqua Mission: Design, Science Objectives, Data Products, and Processing Systems. *IEEE Trans. Geosci. Remote Sens.*, **41,** 253-264.

Baran, A. J. and L. C. Labonnote, 2006: On the Reflection and Polarisation Properties of Ice Cloud. *JQSRT*, **100,** 41-54.

Baum, B. A., K. I. Strabala, S. A. Ackerman, M. D. King, W. P. Menzel, P. F. Soulen, and P. Yang, 2000: Remote Sensing of Cloud Properties Using Modis Airborne Simulator Imagery During Success. Ii- Cloud Thermodynamic Phase. *J. Geophys. Res.*, **105,** 11781-11792.

Baum, B., P. Yang, A. Heymsfield, and S. Thomas, 2005a: Bulk Scattering Properties for the Remote Sensing of Ice Clouds. Part I: Microphysical Data and Models. *Journal of Appl. Meteor.*, **44,** 1885-1895.

Baum, B. A., P. Yang, A. J. Heymsfield, S. Platnick, M. D. King, Y. X. Hu, and S. T. Bedka, 2005b: Bulk Scattering Properties for the Remote Sensing of Ice Clouds. Part Ii: Narrowband Models. *Journal of Appl. Meteor.*, **44,** 1896-1911.

Baum, B. A., P. Yang, S. Nasiri, A. K. Heidinger, A. Heymsfield, and J. Li, 2007: Bulk Scattering Properties for the Remote Sensing of Ice Clouds. Part III: High-Resolution Spectral Models from 100 to 3250 Cm-1. *Journal of Applied Meteorology and Climatology*, **46,** 423-434.

Baumgardner, D., 1986: A New Technique for the Study of Cloud Microstructure. *J. Atmos. Oceanic Technol.*, **3,** 340-343.

Bloom, H. J., 2001: The Cross-Track Infrared Sounder (Cris): A Sensor for Operationalmeteorological Remote Sensing. *Geoscience and Remote Sensing Symposium, 2001. IGARSS'01. IEEE 2001 International*, **3,** 50-54.

Blumstein, D., G. Chalon, T. Carlier, C. Buil, P. Hebert, T. Maciaszek, G. Ponce, T. Phulpin, B. Tournier, and D. Simeoni, 2004: Iasi Instrument: Technical Overview and Measured Performances. *Proc. SPIE*, **5543,** 196-207.

Bohren, C. F. and D. R. Huffman, 1983: *Absorption and Scattering of Light by Small Particles.* WILEY.

Boville, B. A., P. J. Rasch, J. J. Hack, and J. R. McCaa, 2006: Representation of Clouds and Precipitation Processes in the Community Atmosphere Model Version 3 (Cam3). *J. Climate*, **19,** 2184-2198.

Buriez, J. C., F. Parol, C. Cornet, and M. Doutriaux-Boucher, 2005: An Improved Derivation of the Top-of-Atmosphere Albedo from Polder/Adeos-2: Narrowband Albedos. *J. Geophys. Res.*, **110,** D05202, doi:10.1029/2004JD005243.

C.-Labonnote, L., G. Brogniez, M. Doutriaux-Boucher, J. C. Buriez, J. F. Gayet, and H. Chepfer, 2000: Modeling of Light Scattering in Cirrus Clouds with Inhomogeneous Hexagonal Monocrystals. Comparison with in-situ and Adeos-Polder Measurements. *Geophys. Res. Lett.*, **27,** 113-116.

C.-Labonnote, L., G. Brogniez, J. C. Buriez, M. Doutriaux-Boucher, J. F. Gayet, and A. Macke, 2001: Polarized Light Scattering by Inhomogeneous Hexagonal Monocrystals: Validation with Adeos-Polder Measurements. *J Geophys Res*, **106,** 12139-12155.

Cahalan, R. F., W. Ridgway, W. J. Wiscombe, T. L. Bell, and J. B. Snider, 1994: The Albedo of Fractal Stratocumulus Clouds. *J. Atmos. Sci.*, **51,** 2434-2455.

Chandrasekhar, S., 1960: *Radiative Transfer*. Courier Dover Publications.

Chepfer, H., G. Brogniez, and Y. Fouquart, 1998: Cirrus Clouds Microphysical Properties Deduced from Polder Observations. *J. Quant. Spectrosc. Radiat. Transfer*, **60,** 375–390.

Chou, M. D., 1992: A Solar Radiation Model for Use in Climate Studies. *J. Atmos. Sci.*, **49,** 762-772.

Clough, S., M. Iacono, and J. L. Moncet, 1992: Line-by-Line Calculations of Atmospheric Fluxes and Cooling Rates- Application to Water Vapor. *J. Geophys. Res.*, **97,** 15761-15785.

Collins, D. G., W. G. Blattner, M. B. Wells, and H. G. Horak, 1972: Backward Monte Carlo Calculations of the Polarization Characteristics of the Radiation Emerging from Spherical-Shell Atmospheres. *Appl. Opt.*, **11,** 2684-2696.

Cromwell, P. R., 1997: *Polyhedra* Cambridge University Press.

Cziczo, D. J., D. M. Murphy, P. K. Hudson, and D. S. Thomson, 2004: Single Particle Measurements of the Chemical Composition of Cirrus Ice Residue During Crystal-Face. *J. Geophys. Res.*, **109,** D04201, doi:10.1029/2003JD004032.

de Haan, J. F., P. B. Bosma, and J. W. Hovenier, 1987: The Adding Method for Multiple Scattering Calculations of Polarized Light. *Astron. Astrophys*, **183,** 371–391.

DeMott, P. J., D. C. Rogers, S. M. Kreidenweis, Y. Chen, C. H. Twohy, D. Baumgardner, A. J. Heymsfield, and K. R. Chan, 1998: The Role of Heterogeneous Freezing Nucleation in Upper Tropospheric Clouds: Inferences from Success. *Geophys. Res. Lett.*, **25,** 1387-1390.

Deschamps, P. Y., F. M. Breon, M. Leroy, A. Podaire, A. Bricaud, J. C. Buriez, and G. Seze, 1994: The Polder Mission: Instrument Characteristics and Scientific Objectives. *IEEE Trans. Geosci. Remote Sens.*, **32,** 598-615.

Dessler, A. E. and P. Yang, 2003: The Distribution of Tropical Thin Cirrus Clouds Inferred from Terra Modis Data. *J. Climate*, **16,** 1241-1247.

Dowling, D. R. and L. F. Radke, 1990: A Summary of the Physical Properties of Cirrus Clouds. *Journal of Appl. Meteor.*, **29,** 970-978.

Draine, B. T. and P. J. Flatau, 1994: Discrete-Dipole Approximation for Scattering Calculations. *J. Opt. Soc. Am. A*, **11,** 1491–1499.

Dye, J. E. and D. Baumgardner, 1984: Evaluation of the Forward Scattering Spectrometer Probe. Part I: Electronic and Optical Studies. *J. Atmos. Oceanic Technol.*, **1,** 329-344.

Ebert, E. and J. Curry, 1992: A Parameterization of Ice Cloud Optical Properties for Climate Models *J. Geophys. Res.*, **97,** 3831–3836.

Errico, R. M., 1997: What Is an Adjoint Model? *Bull. Amer. Meteor. Soc.*, **78,** 2577-2591.

Evans, K. F., 1998: The Spherical Harmonics Discrete Ordinate Method for Three-Dimensional Atmospheric Radiative Transfer. *J. Atmos. Sci.*, **55,** 429–446.

Field, P. R., R. Wood, P. R. A. Brown, P. H. Kaye, E. Hirst, R. Greenaway, and J. A. Smith, 2003: Ice Particle Interarrival Times Measured with a Fast Fssp. *J. Atmos. Oceanic Technol.*, **20,** 249-261.

Field, P. R., A. J. Heymsfield, and A. Bansemer, 2006: Shattering and Particle Interarrival Times Measured by Optical Array Probes in Ice Clouds. *J. Atmos. Oceanic Technol.*, **23,** 1357-1371.

Foot, J. S., 1988: Some Observations of the Optical Properties of Clouds. Part II: Cirrus. *Quarterly Journal of the Royal Meteorological Society*, **114,** 145-164.

Fry, E. S., J. Musser, G. W. Kattawar, and P. W. Zhai, 2006: Integrating Cavities: Temporal Response. *Appl. Opt.*, **45,** 9053-9065.

Gaiser, S. L., H. H. Aumann, L. L. Strow, S. E. Hannon, and M. Weiler, 2003: In-Flight Spectral Calibration of the Atmospheric Infrared Sounder. *IEEE Trans. Geosci. Remote Sens.*, **41,** 287-297.

Gardiner, B. A. and J. Hallett, 1985: Degradation of in-Cloud Forward Scattering Spectrometer Probe Measurements in the Presence of Ice Particles. *J. Atmos. Oceanic Technol.*, **2,** 171-180.

Garrett, T. J., H. Gerber, D. G. Baumgardner, C. H. Twohy, and E. M. Weinstock, 2003: Small, Highly Reflective Ice Crystals in Low-Latitude Cirrus. *Geophys. Res. Lett*, **30,** 2132, doi:10.1029/2003GL018153.

Garrett, T. J., 2007: Comments On "Effective Radius of Ice Cloud Particle Populations Derived from Aircraft Probes". *J. Atmos. Oceanic Technol.*, **24,** 1495-1503.

Gayet, J.-F., G. Febvre, and H. Larsen, 1996a: The Reliability of the PMS FSSP in the Presence of Small Ice Crystals. *J. Atmos. Oceanic Technol.*, **13,** 1300-1310.

Gayet, J.-F., G. Febvre, G. Brogniez, H. Chepfer, W. Renger, and P. Wendling, 1996b: Microphysical and Optical Properties of Cirrus and Contrails: Cloud Field Study on 13 October 1989. *J. Atmos. Sci.*, **53,** 126-138.

Gerber, H., Y. Takano, T. J. Garrett, and P. V. Hobbs, 2000: Nephelometer Measurements of the Asymmetry Parameter, Volume Extinction Coefficient, and Backscatter Ratio in Arctic Clouds. *J. Atmos. Sci.*, **57,** 3021-3034.

Goldberg, M. D., Y. Qu, L. M. McMillin, W. Wolf, L. Zhou, and M. Divakarla, 2003: Airs near-Real-Time Products and Algorithms in Support of Operational Numerical Weather Prediction. *IEEE Transactions on Geoscience and Remote Sensing*, **41,** 379-389.

Hansen, J. E. and J. W. Hovenier, 1971: The Doubling Method Applied to Multiple Scattering of Polarized Light. *J. Quant. Spectrosc. Radiat. Transfer*, **11,** 809-812.

Hansen, J. E., 1971: Multiple Scattering of Polarized Light in Planetary Atmospheres Part II. Sunlight Reflected by Terrestrial Water Clouds. *J. Atmos. Sci.*, **28,** 1400-1426.

Hansen, J. E. and L. D. Travis, 1974: Light Scattering in Planetary Atmospheres. *Space Science Reviews*, **16,** 527-610.

Hartmann, D. L., M. E. Ockert-Bell, and M. L. Michelsen, 1992: The Effect of Cloud Type on Earth's Energy Balance: Global Analysis. *J. Climate*, **5,** 1281–1304.

Hartmann, D. L., J. R. Holton, and Q. Fu, 2001: The Heat Balance of the Tropical Tropopause, Cirrus, and Stratospheric Dehydration. *Geophys. Res. Lett*, **28,** 1969–1972.

Heymsfield, A., 1972: Ice Crystal Terminal Velocities. *J. Atmos. Sci.*, **29,** 1348-1357.

Heymsfield, A. J. and L. M. Miloshevich, 1993: Homogeneous Ice Nucleation and Supercooled Liquid Water in Orographic Wave Clouds. *J. Atmos. Sci.*, **50,** 2335-2353.

——, 1995: Relative Humidity and Temperature Influences on Cirrus Formation and Evolution: Observations from Wave Clouds and Fire Ii. *J. Atmos. Sci.*, **52,** 4302-4326.

Heymsfield, A. J. and G. M. McFarquhar, 1996: High Albedos of Cirrus in the Tropical Pacific Warm Pool: Microphysical Interpretations from Cepex and from Kwajalein, Marshall Islands. *J. Atmos. Sci.*, **53,** 2424-2451.

Heymsfield, A. J., G. M. McFarquhar, W. D. Collins, J. A. Goldstein, F. P. J. Valero, J. Spinhirne, W. Hart, and P. Pilewskie, 1998: Cloud Properties Leading to Highly Reflective Tropical Cirrus: Interpretations from Cepex, Toga Coare, and Kwajalein, Marshall Islands. *J. Geophys. Res.*, **103,** 8805-8812.

Heymsfield, A. J., 2003: Properties of Tropical and Midlatitude Ice Cloud Particle Ensembles. Part I: Median Mass Diameters and Terminal Velocities. *J. Atmos. Sci.*, **60,** 2573–2591.

Heymsfield, A. J., C. Schmitt, A. Bansemer, G.-J. van Zadelhoff, M. J. McGill, C. Twohy, and D. Baumgardner, 2006: Effective Radius of Ice Cloud Particle Populations Derived from Aircraft Probes. *J. Atmos. Oceanic Technol.*, **23,** 361-380.

——, 2007: Reply. *J. Atmos. Oceanic Technol.*, **24,** 1511-1518.

Holton, J. R. and A. Gettelman, 2001: Horizontal Transport and the Dehydration of the Stratosphere. *Geophys. Res. Lett.*, **28,** 2799–2802.

Hong, G., P. Yang, B. C. Gao, B. A. Baum, Y. X. Hu, M. D. King, and S. Platnick, 2007: High Cloud Properties from Three Years of Modis Terra and Aqua Collection 4 Data over the Tropics. *J. Appl. Meteor. Climatol*, **In press**.

Houghton, J. T., Y. Ding, D. J. Griggs, M. Noguer, P. J. v. d. Linden, K. M. X. Dai, and C. A. Johnson, 2001: *Climate Change 2001: The Scientific Basis*. Cambridge University Press.

Hovenier, J. W., C. Van Der Mee, and H. Domke, 2004: *Transfer of Polarized Light in Planetary Atmospheres: Basic Concepts and Practical Methods*. Kluwer Academic Publishers.

Hu, Y., 1994: *A Study of the Link between Cloud Microphysics and Climate Change*, Atmospheric Science, University of Alaska.

Huang, H. L., P. Yang, H. Wei, B. A. Baum, Y. Hu, P. Antonelli, and S. A. Ackerman, 2004: Inference of Ice Cloud Properties from High Spectral Resolution Infrared Observations. *IEEE Transactions on Geoscience and Remote Sensing*, **42,** 842-853.

Inoue, T., 1985: On the Temperature and Effective Emissivity Determination of Semi-Transparent Cirrus Clouds by Bi-Spectral Measurements in the 10 Micron Window Region. *Meteorological Society of Japan, Journal(0026-1165)*, **63,** 88-99.

——, 1987: A Cloud Type Classification with Noaa 7 Split-Window Measurements. *J. Geophys. Res.*, **92,** 3991-4000.

Irvine, W. M., 1968: Diffuse Reflection and Transmission by Cloud and Dust Layers. *JQSRT*, **8,** 471-485.

Jensen, E. J., S. Kinne, and O. B. Toon, 1994: Tropical Cirrus Cloud Radiative Forcing- Sensitivity Studies. *Geophys. Res. Lett.*, **21,** 2023-2026.

Jensen, E. J., O. B. Toon, H. B. Selkirk, J. D. Spinhirne, and M. R. Schoeberl, 1996: On the Formation and Persistence of Subvisible Cirrus Clouds near the Tropical Tropopause. *J. Geophys. Res.*, **101,** 21361-21376.

Jensen, E. and L. Pfister, 2004: Transport and Freeze-Drying in the Tropical Tropopause Layer. *J. Geophys. Res.*, **109,** D02207, doi:10.1029/2003JD004022.

Jensen, E., D. Starr, and O. B. Toon, 2004: Mission Investigates Tropical Cirrus Clouds. *EOS*, **85,** 45–50.

Jin, Z., T. P. Charlock, W. L. Smith Jr, and K. Rutledge, 2004: A Parameterization of Ocean Surface Albedo. *Geophys. Res. Lett*, **31,** doi:10.1029/2004GL021180.

Kahnert, F. M., 2003: Numerical Methods in Electromagnetic Scattering Theory. *JQSRT*, **79,** 775-824.

King, M. D., 1987: Determination of the Scaled Optical Thickness of Clouds from Reflected Solar Radiation Measurements. *J. Atmos. Sci.*, **44,** 1734-1751.

King, M. D., S. C. Tsay, S. E. Platnick, M. Wang, and K. N. Liou, 1997: Cloud Retrieval Algorithms for Modis: Optical Thickness, Effective Particle Radius, and Thermodynamic Phase. *MODIS Algorithm Theoretical Basis Document*, **ATBD-MOD-05,** 78 pp.

Knap, W. H., L. C.-Labonnote, G. Brogniez, and P. Stammes, 2005: Modeling Total and Polarized Reflectances of Ice Clouds: Evaluation by Means of Polder and Atsr-2 Measurements. *Appl. Opt.*, **44,** 4060-4073.

Knollenberg, R. G., 1981: Techniques for probing cloud microstructure. *Clouds-Their Formation, Optical Properties, and Effects*, P. V. Hobbs and A. Deepak, Eds., Academic Press.,15-93.

Knollenberg, R. G., A. J. Dascher, and D. Huffman, 1982: Measurements of the Aerosol and Ice Crystal Populations in Tropical Stratospheric Cumulonimbus Anvils. *Geophys. Res. Lett.*, **9,** 613-616.

Knollenberg, R. G., K. Kelly, and J. C. Wilson, 1993: Measurements of High Number Densities of Ice Crystals in the Tops of Tropical Cumulonimbus. *J. Geophys. Res.*, **98,** 8639-8664.

Knuteson, R. O., H. E. Revercomb, F. A. Best, N. C. Ciganovich, R. G. Dedecker, T. P. Dirkx, S. C. Ellington, W. F. Feltz, R. K. Garcia, H. B. Howell, W. L. Smith, J. F. Short, and D. C. Tobin, 2004a: Atmospheric Emitted Radiance Interferometer. Part II: Instrument Performance. *J. Atmos. Oceanic Technol.*, **21,** 1777-1789.

Knuteson, R. O., H. E. Revercomb, F. A. Best, N. C. Ciganovich, R. G. Dedecker, T. P. Dirkx, S. C. Ellington, W. F. Feltz, R. K. Garcia, and H. B. Howell, 2004b: Atmospheric Emitted Radiance Interferometer. Part I: Instrument Design. *J. Atmos. Oceanic Technol.*, **21,** 1763-1776.

Kratz, D. P., 1995: The Correlated K-Distribution Technique as Applied to the Avhrr Channels. *J. Quant. Spectrosc. Radiat. Transfer*, **53,** 501-517.

Lacis, A. A. and J. Hansen, 1974: A Parameterization for the Absorption of Solar Radiation in the Earth's Atmosphere. *J. Atmos. Sci.*, **31,** 118-133.

Landgraf, J., O. P. Hasekamp, M. A. Box, and T. Trautmann, 2001: A Linearized Radiative Transfer Model for Ozone Profile Retrieval Using the Analytical Forward-Adjoint Perturbation Theory Approach. *Journal of Geophysical Research*, **106,** 27291-27306.

Landgraf, J., O. P. Hasekamp, and T. Trautmann, 2002: Linearization of Radiative Transfer with Respect to Surface Properties. *JQSRT*, **72,** 327-339.

Laurent, C. L., G. Brogniez, M. Doutriaux-Boucher, J. C. Buriez, J. F. Gayet, and H. Chepfer, 2000: Modeling of Light Scattering in Cirrus Clouds with Inhomogeneous Hexagonal Monocrystals. Comparison with in-situ and Adeos-Polder Measurements. *Geophys. Res. Lett.*, **27,** 113-116.

Li, J., H.-L. Huang, C.-Y. Liu, P. Yang, T. J. Schmit, H. Wei, E. Weisz, L. Guan, and W. P. Menzel, 2005a: Retrieval of Cloud Microphysical Properties from Modis and Airs. *Journal of Appl. Meteor.*, **44,** 1526-1543.

Li, J., C. Y. Liu, H. L. Huang, T. J. Schmit, X. Wu, W. P. Menzel, and J. J. Gurka, 2005b: Optimal Cloud-Clearing for Airs Radiances Using Modis. *IEEE Trans. Geosci. Remote Sens.*, **43,** 1266-1278.

Liou, K.-N., 1973: A Numerical Experiment on Chandrasekhar's Discrete-Ordinate Method for Radiative Transfer: Applications to Cloudy and Hazy Atmospheres. *J. Atmos. Sci.*, **30,** 1303-1326.

——, 1986: Influence of Cirrus Clouds on Weather and Climate Processes: A Global Perspective. *Mon. Wea. Rev.*, **114,** 1167–1199.

Liou, K. N., 2002: *An Introduction to Atmospheric Radiation*. Academic Press.

Liu, X., W. L. Smith, D. K. Zhou, and A. Larar, 2006: Principal Component-Based Radiative Transfer Model for Hyperspectral Sensors: Theoretical Concept. *Appl. Opt.*, **45,** 201-209.

Luo, Z. and W. B. Rossow, 2004: Characterizing Tropical Cirrus Life Cycle, Evolution, and Interaction with Upper-Tropospheric Water Vapor Using Lagrangian Trajectory Analysis of Satellite Observations. *J. Climate*, **17,** 4541-4563.

Lynch, D. K., 2002: *Cirrus*. Oxford University Press US.

Macke, A., M. I. Mishchenko, K. Muinonen, and B. E. Carlson, 1995: Scattering of Light by Large Nonspherical Particles: Ray-Tracing Approximation Versus T-Matrix Method. *Opt. Lett*, **20,** 1934-1936.

Macke, A., J. Mueller, and E. Raschke, 1996: Single Scattering Properties of Atmospheric Ice Crystals. *J. Atmos. Sci.*, **53,** 2813-2825.

Marchuk, G. I., 1964: Equation for the Value of Information from Weather Satellites and Formulation of Inverse Problems. *Cosmic Res.*, **2,** 394–408.

McFarquhar, G. M. and A. J. Heymsfield, 1996: Microphysical Characteristics of Three Anvils Sampled During the Central Equatorial Pacific Experiment. *J. Atmos. Sci.*, **53,** 2401-2423.

——, 1997: Parameterization of Tropical Cirrus Ice Crystal Size Distributions and Implications for Radiative Transfer: Results from Cepex. *J. Atmos. Sci.*, **54,** 2187-2200.

McFarquhar, G. M., A. J. Heymsfield, J. Spinhirne, and B. Hart, 2000: Thin and Subvisual Tropopause Tropical Cirrus: Observations and Radiative Impacts. *J. Atmos. Sci.*, **57,** 1841-1853.

McFarquhar, G. M., J. Um, M. Freer, D. Baumgardner, G. L. Kok, and G. Mace, 2007: Importance of Small Ice Crystals to Cirrus Properties: Observations from the Tropical Warm Pool International Cloud Experiment (Twp-Ice). *Geophys. Res. Lett.*, **34,** doi:10.1029/2007GL029865.

McMillan, W. W., C. Barnet, L. Strow, M. T. Chahine, M. L. McCourt, J. X. Warner, P. C. Novelli, S. Korontzi, E. S. Maddy, and S. Datta, 2005: Daily Global Maps of Carbon Monoxide from NASA's Atmospheric Infrared Sounder. *Geophys. Res. Lett*, **32,** doi:10.1029/2004GL021821.

McMillin, L. M., L. J. Crone, and T. J. Kleespies, 1995: Atmospheric Transmittance of an Absorbing Gas. 5. Improvements to the Optran Approach. *Appl. Opt*, **34,** 8396-8399.

Miller, S. D., J. D. Hawkins, J. Kent, F. J. Turk, T. F. Lee, A. P. Kuciauskas, K. Richardson, R. Wade, and C. Hoffman, 2006: Nexsat: Previewing Npoess/Viirs Imagery Capabilities. *Bull. Amer. Meteor. Soc.*, **87,** 433-446.

Minnis, P., K. N. Liou, and Y. Takano, 1993: Inference of Cirrus Cloud Properties Using Satellite-Observed Visible and Infrared Radiances. Part I: Parameterization of Radiance Fields. *J. Atmos. Sci.*, **50,** 1279-1304.

Minnis, P., D. P. Garber, D. F. Young, R. F. Arduini, and Y. Takano, 1998: Parameterizations of Reflectance and Effective Emittance for Satellite Remote Sensing of Cloud Properties. *J. Atmos. Sci.*, **55,** 3313-3339.

Mishchenko, M. I., L. D. Travis, and D. W. Mackowski, 1996: T-Matrix Computations of Light Scattering by Nonspherical Particles: A Review. *J. Quant. Spectrosc. Radiat. Transfer*, **55,** 535-575.

Mishchenko, M. I., L. D. Travis, and J. W. Hovenier, 2000: *Light Scattering by Nonspherical Particles: Theory, Measurements, and Applications*. Academic Press.

Mishchenko, M. I., B. Cairns, G. Kopp, C. F. Schueler, B. A. Fafaul, J. E. Hansen, R. J. Hooker, T. Itchkawich, H. B. Maring, and L. D. Travis, 2007: Accurate Monitoring of Terrestrial Aerosols and Total Solar Irradiance: Introducing the Glory Mission. *Bull. Amer. Meteor. Soc.*, **88,** 677-691.

Moncet, J.-L., G. Uymin, and H. E. Snell, 2004: Atmospheric Radiance Modeling Using the Optimal Spectral Sampling (OSS) Method. *Proc. SPIE*, **SPIE-5425,** 368-374.

Moncet, J. L. and S. A. Clough, 1997: Accelerated Monochromatic Radiative Transfer for Scattering Atmospheres: Application of a New Model to Spectral Radiance Observations. *J. Geophys. Res*, **102,** 853–21.

Muinonen, K., T. Nousiainen, P. Fast, K. Lumme, and J. Peltoneimi, 1996: Light Scattering by Gaussian Random Particles: Ray Optics Approximation. *J. Quant. Spectrosc. Radiat. Transfer*, **55,** 577-601.

Nakajima, T. and M. D. King, 1990: Determination of the Optical Thickness and Effective Particle Radius of Clouds from Reflected Solar Radiation Measurements. Part I: Theory. *J. Atmos. Sci.*, **47,** 1878–1893.

Newell, R. E., Y. Zhu, E. V. Browell, S. Ismail, W. G. Read, J. W. Waters, K. K. Kelly, and S. C. Liu, 1996: Upper Tropospheric Water Vapor and Cirrus: Comparison of Dc-8 Observations, Preliminary Uars Microwave Limb Sounder Measurements and Meteorological Analyses. *J. Geophys. Res.*, **101,** 1931-1942.

Niu, J., P. Yang, H. L. Huang, J. E. Davies, J. Li, B. A. Baum, and Y. X. Hu, 2007: A Fast Infrared Radiative Transfer Model for Overlapping Clouds. *JQSRT*, **103,** 447-459.

Nousiainen, T. and G. M. McFarquhar, 2004: Light Scattering by Quasi-Spherical Ice Crystals. *J. Atmos. Sci.*, **61,** 2229-2248.

Oreopoulos, L. and R. Davies, 1998: Plane Parallel Albedo Biases from Satellite Observations. Part I: Dependence on Resolution and Other Factors. *J. Climate*, **11,** 919-932.

Ou, S. C., K. N. Liou, W. M. Gooch, and Y. Takano, 1993: Remote Sensing of Cirrus Cloud Properties Using Avhrr 3.7 and 10.9 Pm Channels. *Appl. Opt*, **32,** 2171-2180.

Parol, F., J. C. Buriez, G. Brogniez, and Y. Fouquart, 1991: Information Content of Avhrr Channels 4 and 5 with Respect to the Effective Radius of Cirrus Cloud Particles. *Journal of Appl. Meteor.*, **30,** 973-984.

Plass, G. N. and G. W. Kattawar, 1968: Monte Carlo Calculations of Light Scattering from Clouds. *Appl. Opt*, **7,** 415-419.

Platnick, S., M. D. King, S. A. Ackerman, W. P. Menzel, B. A. Baum, J. C. Riedi, and R. A. Frey, 2003: The Modis Cloud Products: Algorithms and Examples from Terra. *IEEE Trans. Geosci. Remote Sens.*, **41,** 459-473.

Prabhakara, C., R. S. Fraser, G. Dalu, M.-L. C. Wu, R. J. Curran, and T. Styles, 1988: Thin Cirrus Clouds: Seasonal Distribution over Oceans Deduced from Nimbus-4 Iris. *Journal of Appl. Meteor.*, **27,** 379-399.

Pruppacher, H. and J. Klett, 1997: *Microphysics of Clouds and Precipitation*. Kluwer Academic Pub.

Ramanathan, V., R. D. Cess, E. F. Harrison, P. Minnis, B. R. Barkstrom, E. Ahmad, and D. Hartmann, 1989: Cloud-Radiative Forcing and Climate: Results from the Earth Radiation Budget Experiment. *Science*, **243,** 57 - 63.

Randall, D. A., M. E. Schlesinger, V. Galin, V. Meleshko, J. J. Morcrette, and R. Wetherald, 2006: Cloud Feedbacks. *Frontiers in the Science of Climate Modeling*, J. T. Kiehl and V. Ramanathan, Eds., Cambridge University Press, 217-250.

Riedi, J., B. Marchant, S. Platnick, B. Baum, F. Thieuleux, C. Oudard, F. Parol, J. M. Nicolas, and P. Dubuisson, 2007: Cloud Thermodynamic Phase Inferred from Merged Polder and Modis Data. *Atmos. Chem. Phys. Discuss*, **7,** 14103-14137.

Rodgers, C. D., 2000: *Inverse Methods for Atmospheric Sounding: Theory and Practice*. World Scientific.

Rolland, P., K. N. Liou, M. D. King, S. C. Tsay, and G. M. McFarquhar, 2000: Remote Sensing of Optical and Microphysical Properties of Cirrus Clouds Using Moderate-Resolution Imaging Spectrometer (Modis) Channels: Methodology and Sensitivity to Physical Assumptions. *J. Geophys. Res.*, **105,** 11721-11738.

Salomonson, V. V., W. L. Barnes, P. W. Maymon, H. E. Montgomery, and H. Ostrow, 1989: Modis: Advanced Facility Instrument for Studies of the Earth as Asystem. *IEEE Trans. Geosci. Remote Sens.*, **27,** 145-153.

Sassen, K. and J. R. Campbell, 2001: A Midlatitude Cirrus Cloud Climatology from the Facility for Atmospheric Remote Sensing. Part I: Macrophysical and Synoptic Properties. *J. Atmos. Sci.*, **58,** 481-496.

Saunders, R., M. Matricardi, and P. Brunel, 1999: An Improved Fast Radiative Transfer Model for Assimilation of Satellite Radiance Observations. *Quarterly Journal of the Royal Meteorological Society*, **125,** 1407-1425.

Saunders, R., 2000: A Global Comparison of Hirs and Avhrr Radiances. *Proc. 11th Int. ATOVS Study Conf***,** 345.

Siméoni, D., C. Singer, and G. Chalon, 1997: Infrared Atmospheric Sounding Interferometer. *Acta Astronautica*, **40,** 113-118.

Slingo, A., 1989: A Gcm Parameterization for the Shortwave Radiative Properties of Water Clouds. *J. Atmos. Sci.*, **46,** 1419-1427.

Stamnes, K., S. C. Tsay, K. Jayaweera, and W. Wiscombe, 1988: Numerically Stable Algorithm for Discrete-Ordinate-Method Radiative Transfer in Multiple Scattering and Emitting Layered Media. *Appl. Opt.*, **27,** 2502-2509.

Stephens, G. L., 2002: Cirrus, climate and global change. *Cirrus*, D. K. Lynch, Ed., Oxford University Press, 433–448.

Stephens, G. L., D. G. Vane, R. J. Boain, G. G. Mace, K. Sassen, Z. Wang, A. J. Illingworth, E. J. Connor, W. B. Rossow, S. L. Durden, S. D. Miller, R. T. Austin, A. Benedetti, C. Mitrescu, and T. CloudSat Science Team, 2002: The Cloudsat Mission and the a-Train. *Bull. Amer. Meteor. Soc.*, **83,** 1771-1790.

Stephens, G. L., 2005: Cloud Feedbacks in the Climate System: A Critical Review. *J. Climate*, **18,** 237-273.

Strow, L. L., S. E. Hannon, S. De Souza-Machado, H. E. Motteler, and D. Tobin, 2003: An Overview of the Airs Radiative Transfer Model. *IEEE Trans. Geosci. Remote Sens.*, **41,** 303-313.

Taflove, A. and S. C. Hagness, 2000: *Computational Electrodynamics: The Finite-Difference Time-Domain Method*. Artech House.

Takano, Y. and K.-N. Liou, 1989a: Solar Radiative Transfer in Cirrus Clouds. Part Ii: Theory and Computation of Multiple Scattering in an Anisotropic Medium. *J. Atmos. Sci.*, **46,** 20-36.

——, 1989b: Solar Radiative Transfer in Cirrus Clouds. Part I: Single-Scattering and Optical Properties of Hexagonal Ice Crystals. *J. Atmos. Sci.*, **46,** 3-19.

Tian, B., D. E. Waliser, E. J. Fetzer, B. H. Lambrigtsen, Y. L. Yung, and B. Wang, 2006: Vertical Moist Thermodynamic Structure and Spatial–Temporal Evolution of the MJO in Airs Observations. *J. Atmos. Sci.*, **63,** 2462-2485.

Twomey, S., H. Jacobowitz, and H. B. Howell, 1966: Matrix Methods for Multiple-Scattering Problems. *J. Atmos. Sci.*, **23,** 289-298.

van de Hulst, H. C., 1957: *Light Scattering by Small Particles.* John Wiley & Sons.

——, 1980: *Multiple Light Scattering. Tables, Formulas and Applications*. Academic Press.

Vouk, V., 1948: Projected Area of Convex Bodies. *Nature*, **162,** 330-331.

Wang, P.-H., P. Minnis, M. P. McCormick, G. S. Kent, and K. M. Skeens, 1996: A 6-Year Climatology of Cloud Occurrence Frequency from Stratospheric Aerosol and Gas Experiment II Observations (1985–1990). *J. Geophys. Res.*, **101,** 29407–29429.

Wang, P. I. H., M. P. McCormick, L. R. Poole, W. P. Chu, G. K. Yue, G. S. Kent, and K. M. Skeens, 1994: Tropical High Cloud Characteristics Derived from Sage II Extinction Measurements. *Atmospheric research*, **34,** 53-83.

Warren, S. G., 1984: Optical Constants of Ice from the Ultraviolet to the Microwave. *Appl. Opt.*, **23,** 1206–1225.

Wei, H., P. Yang, J. Li, B. A. Baum, H. L. Huang, S. Platnick, Y. Hu, and L. Strow, 2004: Retrieval of Semitransparent Ice Cloud Optical Thickness from Atmospheric Infrared Sounder (Airs) Measurements. *IEEE Trans. Geosci. Remote Sens.*, **42,** 2254-2267.

Winker, D. M., J. Pelon, and M. P. McCormick, 2003: The Calipso Mission: Spaceborne Lidar for Observation of Aerosols and Clouds. *Proc. SPIE*, **4893,** 1-11.

Wiscombe, W. J., 1976a: Extension of the Doubling Method to Inhomogeneous Sources. *JQSRT*, **16,** 477-489.

——, 1976b: On Initialization, Error and Flux Conservation in the Doubling Method. *JQSRT*, **16,** 637-658.

——, 1977a: Doubling Initialization Revised. *JQSRT*, **18,** 245-248.

——, 1977b: The Delta–M Method: Rapid yet Accurate Radiative Flux Calculations for Strongly Asymmetric Phase Functions. *J. Atmos. Sci.*, **34,** 1408-1422.

——, 1979: Mie Scattering Calculations, Advances in Technique and Fast, Vector-Shaped Computer Codes. *NCAR Tech. Note* **TN-140+STR,** 66.

Wriedt, T., 1998: A Review of Elastic Light Scattering Theories. *Particle & Particle Systems Characterization*, **15,** 67-74.

Wu, M. L. C., 1987: A Method for Remote Sensing the Emissivity, Fractional Cloud Cover and Cloud Top Temperature of High-Level, Thin Clouds. *Journal of Appl. Meteor.*, **26,** 225-233.

Wylie, D. P., W. P. Menzel, H. M. Woolf, and K. I. Strabala, 1994: Four Years of Global Cirrus Cloud Statistics Using Hirs. *J. Climate*, **7,** 1972–1986.

Wylie, D. P. and W. P. Menzel, 1999: Eight Years of High Cloud Statistics Using Hirs. *J. Climate*, **12,** 170–184.

Yang, P. and K. N. Liou, 1996a: Finite-Difference Time Domain Method for Light Scattering by Small Ice Crystals in Three-Dimensional Space. *J. Opt. Soc. Am. A*, **13,** 2072-2085.

——, 1996b: Geometric-Optics-Integral-Equation Method for Light Scattering by Nonspherical Ice Crystals. *Appl. Opt*, **35,** 6568–6584.

——, 1998: Single-Scattering Properties of Complex Ice Crystals in Terrestrial Atmosphere. *Contrib. Atmos. Phys.*, **71,** 223-248.

Yang, P., K. N. Liou, K. Wyser, and D. Mitchell, 2000: Parameterization of the Scattering and Absorption Properties of Individual Ice Crystals. *J. Geophys. Res.*, **105,** 4699-4718.

Yang, P., G. W. Kattawar, and W. J. Wiscombe, 2004: Effect of Particle Asphericity on Single-Scattering Parameters: Comparison between Platonic Solids and Spheres. *Appl. Opt.*, **43,** 4427-4435.

Yang, P., H. Wei, H.-L. Huang, B. A. Baum, Y. X. Hu, G. W. Kattawar, M. I. Mishchenko, and Q. Fu, 2005: Scattering and Absorption Property Database for Nonspherical Ice Particles in the near- through Far-Infrared Spectral Region *Appl. Opt.*, **44,** 5512-5523.

Yang, P., L. Zhang, G. Hong, S. L. Nasiri, B. A. Baum, H.-L. Huang, M. D. King, and S. Platnick, 2007: Differences between Collection 4 and 5 Modis Ice Cloud Optical/Microphysical Products and Their Impact on Radiative Forcing Simulations. *IEEE Trans. Geosci. Remote Sens.*, **45,** 2886-2899.

Zender, C. S. and J. T. Kiehl, 1994: Radiative Sensitivities of Tropical Anvils to Small Ice Crystals. *J. Geophys. Res*, **99,** 25869-25880.

Zhang, M. H., W. Y. Lin, S. A. Klein, J. T. Bacmeister, S. Bony, R. T. Cederwall, A. D. Del Genio, J. J. Hack, N. G. Loeb, and U. Lohmann, 2005: Comparing

Clouds and Their Seasonal Variations in 10 Atmospheric General Circulation Models with Satellite Measurements. *J. Geophys. Res*, **110,** doi:10.1029/2004JD005021.

Zhang, Z., P. Yang, G. W. Kattawar, S.-C. Tsay, B. A. Baum, Y. Hu, A. J. Heymsfiel, and J. Reichardt, 2004: Geometrical-Optics Solution to Light Scattering by Droxtal Ice Crystals. *Appl. Opt.*, **43,** 2490-2499.

Zhang, Z., P. Yang, G. W. Kattawar, and W. J. Wiscombe, 2007: Single-Scattering Properties of Platonic Solids in Geometrical-Optics Regime. *JQSRT*, **106,** 595-603.

Zhou, D. K., W. L. Smith, X. Liu, A. M. Larar, S. A. Mango, and H.-L. Huang, 2007: Physically Retrieving Cloud and Thermodynamic Parameters from Ultraspectral IR Measurements. *J. Atmos. Sci.*, **64,** 969-982.

APPENDIX A

APPLICATION OF THE ADDING-DOUBLING METHOD TO THERMAL INFRARED RADIATIVE TRANSFER

The adding-doubling method is a rigorous method that has been extensively used to deal with the radiative transfer problems in the plane-parallel atmospheres. The basic concepts and derivations of the adding-doubling method can be found in some classic books. In this Appendix, we show the application of the adding-doubling method to the thermal infrared radiative transfers.

In the adding-doubling method, the bidirectional reflection (R) and transmission (T) function are two fundamental and important quantities. Consider a cloud with an optical thickness of τ and an effective size of D_e illuminated from above. The layer is homogenous in terms of scattering albedo ($\langle \varpi \rangle$) and phase function ($\langle P \rangle$). The intensity of incident radiation is $I_{top}^{\downarrow}(\mu', \phi')$, where μ' is the cosine of zenith angle and ϕ' is the azimuthal angle. According to the definitions of R and T, the reflected and transmitted intensity may be expressed as in terms of incident intensity as follows

$$I_{top}^{\uparrow}(\mu,\phi) = \frac{1}{\pi}\int_0^{2\pi}\int_0^1 R(\mu,\phi,\mu',\phi-\phi')I_{top}^{\downarrow}(\mu',\phi')\mu' d\mu' d\phi', \qquad \text{(A1a)}$$

$$I_{bottom}^{\downarrow}(\mu,\phi) = \frac{1}{\pi}\int_0^{2\pi}\int_0^1 T(\mu,\phi;\mu',\phi-\phi')I_{top}^{\downarrow}(\mu',\phi')\mu' d\mu' d\phi', \qquad \text{(A1b)}$$

where $I_{top}^{\uparrow}(\mu,\phi)$ and $I_{bottom}^{\downarrow}(\mu,\phi)$ are reflected and transmitted intensity at cloud top and bottom, respectively. In general cases, R and T are usually decomposed into Fourier series in terms of the relative azimuthal angle $\phi-\phi'$ for the sake of

numerical implementation, and each term in the series is treated independently in the adding-doubling process. However, because the thermal emission under plane-parallel conditions are azimuthally independent, and the azimuthally dependent solar contribution is usually neglected in the spectral region considered in this work, i.e., 800- to 1300 cm^{-1}, only the zero order moment of the Fourier expansion is needed in the present study. In other words, we can use the azimuthally averaged reflection and transmission functions defined as follows:

$$\bar{R}(\mu,\mu') = \frac{1}{2\pi}\int_0^{2\pi} R(\mu,\phi,\mu',\phi-\phi')d(\phi-\phi'), \tag{A2a}$$

$$\bar{T}(\mu,\mu') = \frac{1}{2\pi}\int_0^{2\pi} T(\mu,\phi,\mu',\phi-\phi')d(\phi-\phi'). \tag{A2b}$$

Subsequently, Eq. (A1) reduces to

$$I_{top}^{\uparrow}(\mu) = 2\int_0^1 \bar{R}(\mu,\mu')I_{top}^{\downarrow}(\mu')\mu' d\mu', \tag{A3a}$$

$$I_{botttom}^{\downarrow}(\mu) = 2\int_0^1 \bar{T}(\mu,\mu')I_{top}^{\downarrow}(\mu')\mu' d\mu'. \tag{A3b}$$

Note that $\bar{T}$ consists of two parts, the direct ($\bar{T}_{dirct}$) and diffuse ($\bar{T}_{diffuse}$) transmission. T_{direct} can be found in the form:

$$\bar{T}_{direct}(\mu,\mu') = \frac{1}{2\mu'}\exp(-\tau/\mu')\delta(\mu-\mu'), \tag{A4}$$

where δ is the Dirac delta function. Eqs (A1) to (A4) are defined with respect to incidence from above. Likewise, the azimuthally averaged bidirectional reflection and transmission for incident radiation coming from below, $I_{bottom}^{\uparrow}(\mu')$, are given by

$$I_{bottom}^{\downarrow}(\mu) = 2\int_0^1 \bar{R}^*(\mu,\mu')I_{bottom}^{\uparrow}(\mu')\mu' d\mu', \tag{A5a}$$

$$I_{top}^{\uparrow}(\mu) = 2\int_0^1 \bar{T}^*(\mu,\mu')I_{bottom}^{\uparrow}(\mu')\mu' d\mu', \tag{A5b}$$

where the superscript * denotes that the incident radiation comes from below.

The adding principle states that the bidirectional functions of the combined layer of two adjacent layers, one on top the other, can be obtained through the following adding process:

$$Q = \bar{R}_1^* \bar{R}_2 , \tag{A6a}$$

$$S = \sum_{n=1}^{\infty} Q^n , \tag{A6b}$$

$$D = \bar{T}_1 + S\bar{T}_1 , \tag{A6c}$$

$$U = \bar{R}_2 D , \tag{A6d}$$

$$\bar{R}_{12} = \bar{R}_1 + \bar{T}_1^* U , \tag{A6e}$$

$$\bar{T}_{12} = \bar{T}_2 D , \tag{A6f}$$

where the subscript 1 and 2 refer to the upper and lower layer, respectively. Note that the product of two bidirectional functions in the above equations implies integration over the adjoining solid angle to account for the multiple-scattering effects. For example, an arbitrary $Z = XY$ in above equations is defined as

$$Z(\mu,\mu') = 2\int_0^1 X(\mu,\mu'')Y(\mu'',\mu')\mu'' d\mu'' . \tag{A7}$$

Similar to Eq. (A6), the solution for bidirectional functions of the combined layer for radiation from below may be written as follows:

$$Q^* = \bar{R}_2 \bar{R}_1^* , \tag{A8a}$$

$$S^* = \sum_{n=1}^{\infty} (Q^*)^n , \tag{A8b}$$

$$U^* = \bar{T}_2^* + S^* \bar{T}_2^* , \tag{A8c}$$

$$D^* = \bar{R}_1^* U^* , \tag{A8d}$$

$$\bar{R}_{12}^* = \bar{R}_2^* + \bar{T}_2 D^* , \tag{A8e}$$

$$\bar{T}_{12}^* = \bar{T}_1^* U^* . \tag{A8f}$$

The adding method may also be applied to account for the thermal emission. The thermal emission of the combined layer contributed by the upper layer can be obtained using the adding equations as follows:

$$D_{E1} = E_1^* + SE_1^* , \tag{A9a}$$

$$U_{E1} = \bar{R}_2 D_{E1}, \tag{A9b}$$

$$E_{12} = E_1 + \bar{T}_1^* U_{E1}, \tag{A9c}$$

$$E_{12}^* = \bar{T}_2 D_{E1}, \tag{A9d}$$

where E_1 and E_1^* are, respectively, the upward and downward thermal emission from the upper layer, S is defined in Eq. (A6b). Similarly, the contributions of the bottom layer to the thermal emission of the combined layer are in the forms:

$$U_{E2} = E_2 + S^* E_2, \tag{A10a}$$

$$D_{E2} = \bar{R}_1^* U_{E2}, \tag{A10b}$$

$$E_{12} = \bar{T}_1^* U_{E2}, \tag{A10c}$$

$$E_{12}^* = E_2^* + \bar{T}_2 D_{E2}, \tag{A10d}$$

where E_2 and E_2^* are, respectively, the upward and downward thermal emission from the bottom layer, S^* is defined in Eq. (A8b). The thermal emission of combined layer in a matrix format can be obtained by mathematical manipulation of Eqs (A9) and (A10):

$$\begin{vmatrix} E_{12} \\ E_{12}^* \end{vmatrix} = \mathbf{A} \begin{vmatrix} E_1 \\ E_2 \\ E_1^* \\ E_2^* \end{vmatrix}, \tag{A11a}$$

where

$$\mathbf{A} = \begin{vmatrix} 1 & \bar{T}_1^* + \bar{T}_1^* S^* & \bar{T}_1^* \bar{R}_2 + \bar{T}_1^* \bar{R}_2 S & 0 \\ 0 & \bar{T}_2 \bar{R}_1^* + \bar{T}_2 \bar{R}_1^* S^* & \bar{T}_2 + \bar{T}_2 S & 1 \end{vmatrix}. \tag{A11b}$$

Note that because $\mathbf{A}$ is temperature independent, the thermal emission of a non-isothermal cloud can be obtained using the doubling method as long as it is homogenous in terms of bulk scattering properties.

For the sake of numerical implementation of integral in Eq (A7), the discrete-ordinate approximation is usually used in the adding-doubling method. Under the approximation, the integral in Eq. (A7) becomes:

$$Z(\mu_i,\mu_j)=2\sum_k^N X(\mu_i,\mu_k)Y(\mu_k,\mu_j)\mu_k w_k \tag{A12}$$

where μ_k and w_k are quadrature points and corresponding weights determined by the discretization scheme. One of the most widely used quadratures for ordinate discretization is the so-called double Gaussian quadrature, in which the abscissas $\mu_i(\mu_j)$ are distributed symmetrically around 0.5 and clustered toward 0 and 1. Under the discrete-ordinate approximation, $\bar{R}$ and $\bar{T}$ become matrices, whereas E becomes a vector as follows:

$$\bar{\mathbf{R}}_{i,j}=\bar{R}(\mu_i,\mu_j), \tag{A13a}$$

$$\bar{\mathbf{T}}_{i,j}=\bar{T}(\mu_i,\mu_j),\ i,j=1,2,3...,N, \tag{A13b}$$

$$\mathbf{E}_i=E(\mu_i), \tag{A13c}$$

where μ_i is the cosine of the zenith angle of, respectively, reflected, transmitted and emitted radiation in the case for $\bar{\mathbf{R}}$, $\bar{\mathbf{T}}$ and $\mathbf{E}$. μ_j is the cosine of the zenith angle of incident radiation. N is the number of the points that the hemisphere $0<\mu\le 1$ is discretized into. Note that $2N$ is the so-called "number of streams". Eq. (A12) can be further simplified by defining a matrix operator as follows:

$$\mathbf{Z}=\mathbf{X}\otimes\mathbf{Y}=2\sum_{k=1}^N \mathbf{X}_{i,k}\mathbf{Y}_{k,j}\mu_k w_k,\ i,j=1,2,3...,N. \tag{A14}$$

The last obstacle in the way of numerical implementation of the adding method is the infinite series in Eqs. (6b) and (8b). It has been shown that the infinite series can be efficiently treated as follows:

$$\mathbf{S}=\mathbf{Q}\otimes(\mathbf{1}-\mathbf{Q})^{-1}, \tag{A15}$$

where $\mathbf{1}$ is the identity matrix in the sense that $\mathbf{1}\otimes\mathbf{1}=\mathbf{1}$, and $(\cdot)^{-1}$ is the inverse operator such that $\mathbf{X}\otimes\mathbf{X}^{-1}=\mathbf{1}$. By substiting Eq. (A14) and (A15) into the adding equations in Eqs. (A6), (A8) and (A11), the adding process becomes a series of matrix operations and therefore can be easily implemented with the matrix manipulation subroutines from numerical linear algebra packages like LAPACK.

The adding method described above requires that the $\bar{\mathbf{R}}$, $\bar{\mathbf{T}}$ and $\mathbf{E}$ be known for the layers to be added. To obtain the $\bar{\mathbf{R}}$, $\bar{\mathbf{T}}$ and $\mathbf{E}$ of a cloud, homogenous in terms of bulk scattering properties, the doubling method can be used. In the method, the cloud is divided in to a large amount of identical sub-layers. The sub-layers are optically thin ($\tau\sim 2^{-10}$) so that their $\bar{\mathbf{R}}$, $\bar{\mathbf{T}}$ and $\mathbf{E}$ can be obtained analytically. The properties of the whole cloud are obtained through a process in which two identical sub-layers are added at each step, i.e. the doubling process.

APPENDIX B

INTERPOLATION SCHEME FOR FIRTM-AD TO OBTAIN RADIANCES AT THE USER-SPECIFIED ANGLES FROM MODEL OUTPUTS

To obtain the radiances at the user-specified viewing angles from the model outputs at the quadrature points, an angular interpolation scheme is needed. There are numerous other schemes for the angular interpolation. In the current FIRTM-AD, the following scheme is used. The radiances at model angles are first expanded as a series of the "shifted" Legendre polynomial:

$$I(\tau;\mu) = \sum_{l=1}^{M} (2l+1)\chi_l(\tau)\overline{P}_l(\mu), \tag{B1a}$$

and

$$\chi_l(\tau) = \int_0^1 I(\tau;\mu)\overline{P}_l(\mu)d\mu, \tag{B1b}$$

where χ_l is the expansion coefficient of the l^{th} moment and $\overline{P}_l$ is the "shifted" Legendre polynomial analogous to the Legendre polynomials, but defined on the interval [0,1] and obeying the orthogonality relationship:

$$\int_0^1 \overline{P}_m(\mu)\overline{P}_n(\mu)d\mu = \frac{1}{2n+1}\delta_{mn}, \tag{B2}$$

where δ_{mn} is the Kronecker delta. The expansion coefficient χ_l can be found by substituting the radiances at the quadrature points into Eq. (B1b). And then the radiances at the user-specified angles are estimated using Eq. (B1a).

APPENDIX C

ADJOINT MODEL AND RADIATIVE PERTURBATION THEORY

1. Forward Radiative Transfer Equation (RTE)

Consider a general absorbing and scattering, plane-parallel atmosphere bounded by a reflecting surface. The equation for the transfer of unpolarized radiation in this system can be written in the operator form as follows:

$$LI = Q, \tag{C1}$$

where I is the radiance; Q is the source term that will be discussed later; and L is the forward transport operator in the formation of (Landgraf et al. 2001, Landgraf et al. 2002):

$$L = \int_{4\pi} d\mathbf{\Omega}' \left\{ \left(\mu \frac{\partial}{\partial \tau} - 1 \right) \delta(\mathbf{\Omega}' - \mathbf{\Omega}) + \frac{\varpi(\tau)}{4\pi} P_{11}(\tau, \mathbf{\Omega}' \to \mathbf{\Omega}) + \delta(\tau - \tau^*) H(\mu) |\mu| R_s(\mathbf{\Omega}, \mathbf{\Omega}') H(-\mu') |\mu'| \right\} \circ . \tag{C2}$$

In Eq (C2), τ is the optical depth; the direction $\mathbf{\Omega}$ is specified by (μ, ϕ), where $\mu = \cos\theta, \theta$ is the zenith angle and ϕ is the azimuth angle (Note that $\mu > 0$ indicates upward directions and $\mu' < 0$ downward directions); ϖ is the single-scattering albedo of the atmosphere; P_{11} is the first element of the scattering-matrix; $\mathbf{\Omega}' \to \mathbf{\Omega}$ denotes the scattering angle between incident direction $\mathbf{\Omega}'$ and scattering direction $\mathbf{\Omega}$; τ^* is total optical thickness of the atmosphere (i.e., the optical depth at the surface); $R_s(\mathbf{\Omega}, \mathbf{\Omega}')$ is the bidirectional reflection distribution function (BDRF) of the surface. Furthermore, δ represents the Dirac-delta function and H represents the Heaviside step function:

$$H(\mu)=\begin{cases}0, & x\le 0\\ 1, & x>0\end{cases}. \tag{C3}$$

The source term, Q, is independent of I and can be, generally speaking, in any form. However, in most cases of "forward" computations, Q is either a beam source corresponding to the sunlight that illumines the top of the atmosphere or the thermal emission of the atmosphere and the surface. The beam source is given by:

$$Q^{beam}=-\mu_0 F_0\delta(\tau)\delta(\mathbf{\Omega}-\mathbf{\Omega}_0), \tag{C4}$$

where F_0 is the solar flux per unit area perpendicular to the direction of sunlight specified by $\mathbf{\Omega}_0=(-\mu_0,\phi_0)$. And, the thermal source is as follows:

$$Q^{thermal}=-[1-\varpi(\tau)]B[T_a(\tau)]-\delta(\tau-\tau^*)H(\mu)|\mu|\varepsilon_s(\mathbf{\Omega})B(T_s), \tag{C5}$$

where B is the Planck function; T_a and T_s are the temperature of atmosphere and surface, respectively.

Because the incoming sunlight, the reflection and emission of the surface have all been explicitly included in the RTE, the boundary conditions (BC) are simply:

$$I(\tau=0,\mathbf{\Omega})=0 \quad \text{for } \mu<0, \tag{C6}$$

$$I(\tau=\tau^*,\mathbf{\Omega})=0 \quad \text{for } \mu>0. \tag{C7}$$

It may seem odd to include the surface reflection explicitly in the RTE. It is rather a boundary condition in most literature. The purpose is to obtain simple, namely the "vacuum", boundary conditions, as in Eqs. (C6) and (C7), so that the derivation of adjoint operator later is relatively simple. Nonetheless, it is important

to note that the underlying physics remains the same no matter how the RTE and BC are formed.

2. The adjoint operator

Numerous analytical and numerical models have been developed to solve the radiative transfer problem stated in the last subsection. Most of these models are developed based on the "forward" concept, i.e., to describe the propagation of radiation field forward in time and space. The adjoint model, on the other hand, describes the sensitivity of the output "backward" in time and space to different parameters of the system (Errico 1997, Hu 1994).

For a linear operator L, its adjoint operator, L^*, is a linear operator that satisfies the following equation:

$$\left\langle I^*, LI \right\rangle = \left\langle L^* I^*, I \right\rangle, \tag{C8}$$

where I and I^* are two arbitrary functions defined in a bounded space, the angular brackets $\langle\ \rangle$ denotes the inner product. Note that the form of the adjoint operator depends on the boundary conditions imposed on I and I^*. For example, if I and I^* are two functions defined in the space $[a \le x \le b]$ (the inner product in this case is $\left\langle I, I^* \right\rangle = \int_a^b I(x) \cdot I^*(x) dx$) with the boundary conditions $\left\langle I, I^* \right\rangle\Big|_a = 0$ and $\left\langle I, I^* \right\rangle\Big|_b = 0$, it is straightforward to prove (see Eq.(C9)) that the adjoint operator for $L = \dfrac{\partial}{\partial x}$ is $L^* = -\dfrac{\partial}{\partial x}$.

$$\begin{aligned}\left\langle I^*, LI\right\rangle &= \int_a^b I^* \frac{\partial I}{\partial x} dx = \int_a^b \frac{\partial (I^* I)}{\partial x} dx - \int_a^b I \frac{\partial I^*}{\partial x} dx \\ &= \left\langle I^*, I\right\rangle\Big|_a^b - \int_a^b I \frac{\partial I^*}{\partial x} dx \\ &= \int_a^b I(-\frac{\partial I^*}{\partial x}) dx\end{aligned} \quad . \tag{C9}$$

In the radiative transfer, both I and I^* are in the space of $[0 \le \tau \le \tau^*]$ and $[-1 \le \mu \le 1; 0 \le \phi \le 2\pi]$. The inner product in this case is:

$$\left\langle I_1, I_2\right\rangle = \int_0^{\tau^*} d\tau \int_{4\pi} d\Omega I_1(\tau, \mathbf{\Omega}) I_2(\tau, \mathbf{\Omega}) . \tag{C10}$$

If the following boundary conditions are imposed on I^*:

$$I^*(\tau = 0, \mathbf{\Omega}) = 0 \quad \text{for } \mu > 0 , \tag{C11}$$

$$I^*(\tau = \tau^*, \mathbf{\Omega}) = 0 \quad \text{for } \mu < 0 , \tag{C12}$$

the adjoint operator, L^*, for the forward radiative transport operator, L, in Eq.(C2), is as follows (the derivation is given in the Appendix A):

$$\begin{aligned}L^* = \int_{4\pi} d\mathbf{\Omega}' \Bigg\{ &\left(-\mu \frac{\partial}{\partial \tau} - 1 \right) \delta(\mathbf{\Omega}' - \mathbf{\Omega}) + \\ &\frac{\varpi(\tau)}{4\pi} P_{11}(\tau, -\mathbf{\Omega}' \to -\mathbf{\Omega}) + \delta(\tau - \tau^*) H(-\mu) |\mu| R_s(-\mathbf{\Omega}, -\mathbf{\Omega}') H(\mu') |\mu'| \Bigg\} \circ\end{aligned} \quad . \tag{C13}$$

With the adjoint operator given in Eq.(C13), the adjoint transport equation can be written in the following form:

$$L^* I^* = Q^* , \tag{C14}$$

where Q^* is an arbitrary source.

It may seem that solving the above adjoint transport equation requires the development of a new model, as L^* is apparently different from L. However, this is not the case. By comparing the formulation of forward and adjoint operator,

one may note an interesting and extremely useful relationship between forward and adjoint operator:

$$L^*(\tau,\mathbf{\Omega},\mathbf{\Omega}') = L(\tau,-\mathbf{\Omega},-\mathbf{\Omega}') . \tag{C15}$$

It implies that the same model solving forward radiative transfer problem can also be used to solve the adjoint problem by introducing a new variable:

$$I'(\tau,-\mathbf{\Omega}) = I'(\tau,-\mu,\pi+\phi) = I^*(\tau,\mathbf{\Omega}) . \tag{C16}$$

With the relationship in Eq.(C15), it is straightforward to prove that:

$$L(\tau,\mathbf{\Omega},\mathbf{\Omega}') \circ I'(\mathbf{\Omega}') = L^*(\tau,-\mathbf{\Omega},-\mathbf{\Omega}') \circ I^*(-\mathbf{\Omega}') = Q^*(\tau,-\mathbf{\Omega}) . \tag{C17}$$

Eqs. (C15), (C16) and (C17) have clearly shown that, to solve the adjoint transport problem for a given source $Q^*(\tau,\mathbf{\Omega})$ (i.e., Eq.(C14))one only needs to solve the forward transport problem for an angle-reversed source $Q^*(\tau,-\mathbf{\Omega})$ (i.e., Eq.(C17)), and then reverses all directions in the solution $I'(\tau,\mathbf{\Omega})$ to obtain $I^*(\tau,\mathbf{\Omega})$ (i.e., Eq.(C16)). Note that $I^*(\tau,\mathbf{\Omega})$ and $Q^*(\tau,\mathbf{\Omega})$ are, so far, two arbitrary functions. In the rest of this subsection, the construction of $Q^*(\tau,\mathbf{\Omega})$ and the physical meaning of $I^*(\tau,\mathbf{\Omega})$ will be discussed.

Although the complete radiance field $I(\tau,\mathbf{\Omega})$ can be obtained from the radiative transfer model, only a subset of this information are interested in most applications. For example, only the radiance at the top of the atmosphere (TOA) in the satellite viewing direction $\mathbf{\Omega}_{obs}$ is needed for the satellite remote sensing. To put it mathematically, we introduce the "radiative effects" E and the "response function" R:

$$E = \langle R, I \rangle . \tag{C18}$$

If E refers to the radiance at TOA, the corresponding R is:

$$R = \delta(\tau)\delta(\mathbf{\Omega} - \mathbf{\Omega}_{obs}). \tag{C19}$$

The response function for the upward flux at TOA is:

$$R = H(\mu)|\mu|\delta(\tau) \tag{C20}$$

Shown in Eq.(C18) is the "forward" way to obtain the interest radiative effects. An alternative way to obtain E is through the adjoint method. If the response function, R, is used as the adjoint source Q^*

$$L^* I^* = R, \tag{C21}$$

according to the definition of the adjoint operator in Eq.(C8)), the solution I^* satisfies the following equation:

$$\begin{aligned} E &= \langle R, I \rangle = \langle L^* I^*, I \rangle \\ &= \langle I^*, LI \rangle = \langle I^*, Q \rangle \end{aligned}. \tag{C22}$$

It is now clear from the above analysis that there are the following two methods to obtain an interested radiative effect:

$$LI = Q \rightarrow E = \langle R, I \rangle, \tag{C23}$$

$$L^* I^* = R \rightarrow E = \langle I^*, Q \rangle. \tag{C24}$$

In the "forward" method, the normal (forward) radiative transfer equation with the source function Q is first solved to obtain the radiance field, I, and then the interested radiative effect is extracted from the inner product of I and the response function R. In contrast, The "adjoint" method starts with solving the adjoint transport equation with the pseudo source function R to obtain the adjoint radiance field, I^*, and then the radiative effect is extracted from the inner product

of I^* and the real source function Q. The two ways are equivalent in terms of complexity and computational time, if one seeks only a single radiative effect under a single source say, the radiance observed by a MODIS channel for a given sun-satellite geometry. However, it is clear from Eqs.(C23) and (C24) that the "forward" method is more efficient when multiple effects from a single source are interested, whereas the "adjoint" method is more efficient when a single effect from multiple sources is interested.

Eq.(C24) also reveals that the physical meaning of adjoint radiance I^* is somehow similar to the concept of "weighting function" used in the atmospheric sounding. That is to say, for a given response function, I^* tells us contribution of a unit source at different optical depths and directions contribute to the response

3. The radiative perturbation theory

In practices of remote sensing, climate sensitivity study, data assimilation and many other disciplines, it is often the case that not only the radiative effect is necessary; the changing rates of the effect (i.e., the Jacobian) with respect to different system parameters are also very helpful and thus highly desired. A straightforward way to compute the Jacobian is through the method of finite difference (FD):

$$\frac{\partial E}{\partial x_k} = \lim_{x_k \to 0} \frac{E(x_k + \Delta x_k) - E(x_k)}{\Delta x_k}, \tag{C25}$$

where x_k is a parameter of the system, Δx_k is a perturbation in x_k, $\frac{\partial E}{\partial x_k}$ is the interested Jacobian, $E(x_k + \Delta x_k)$ and $E(x_k)$ are the radiative effect of the

perturbed and unperturbed system, respectively. The FD method is conceptually simple, but not computationally efficient, because the radiative transfer computation must be performed each time when the system is perturbed with different kinds of perturbations.

The adjoint method provides a very efficient way for the computation of Jacobians. Consider the following perturbed problem:

$$L'I' = Q', \tag{C26}$$

where

$$\begin{aligned} L' &= L + \Delta L \\ Q' &= Q + \Delta Q \end{aligned}. \tag{C27}$$

It is straightforward to prove that the change of the radiative effect due to the above perturbation is (Marchuk 1964):

$$\Delta E = \left\langle I^*, \Delta Q \right\rangle - \left\langle I^*, \Delta L I' \right\rangle. \tag{C28}$$

For Jacobian computations, the perturbation is usually very small. As a result, I' can be closely approximated by I' (i.e., $I' \approx I$) and Eq. (C28) becomes:

$$\Delta E \approx \left\langle I^*, \Delta Q \right\rangle - \left\langle I^*, \Delta L I \right\rangle. \tag{C29}$$

The first term in Eq.(C29) corresponds to the contribution of the perturbation to ΔE through its impact on the source, while the second term corresponds to the contribution of the change in transport operator that can be categorized into four parts:

$$\Delta L_\tau = -\Delta\tau(\tau)\circ, \tag{C30}$$

$$\Delta L_\varpi = \int_{4\pi} d\mathbf{\Omega}' \frac{\Delta\varpi(\tau)}{4\pi} P_{11}(\tau, \mathbf{\Omega}' \to \mathbf{\Omega})\circ, \tag{C31}$$

$$\Delta L_{P_{11}} = \int_{4\pi} d\mathbf{\Omega}' \frac{\varpi(\tau)}{4\pi} \Delta P_{11}(\tau, \mathbf{\Omega}' \to \mathbf{\Omega}) \circ , \tag{C32}$$

$$\Delta L_{R_s} = \int_{4\pi} d\mathbf{\Omega}' \delta(\tau - \tau^*) H(\mu) |\mu| \Delta R_s(\mathbf{\Omega}, \mathbf{\Omega}') H(-\mu') |\mu'| \circ , \tag{C33}$$

where ΔL_τ, ΔL_ϖ, $\Delta L_{P_{11}}$ and ΔL_{R_s} corresponds to the change of L caused by the change of optical thickness ($\Delta\tau$), single-scattering albedo ($\Delta\varpi$), scattering phase function (ΔP_{11}) and surface BDRF (ΔR_s), respectively. Taking Eq. (C29) one step further, if the perturbation is due to the small change of an atmosphere parameter x_k (e.g., the size of cloud droplets, the shape of the ice crystals, or the concentration of water vapor), one can obtain the Jacobian of the radiative effect with respect to x_k easily by:

$$\frac{\partial E}{\partial x_k} = \left\langle I^*, \frac{\partial Q}{\partial x_k} \right\rangle - \left\langle I^*, \frac{\partial L}{\partial x_k} I \right\rangle , \tag{C34}$$

where

$$\begin{aligned} \frac{\partial L}{\partial x_k} = & -\frac{\partial \tau}{\partial x_k} \circ + \frac{1}{4\pi} \int_{4\pi} d\mathbf{\Omega}' \frac{\partial \varpi(\tau)}{\partial x_k} P_{11}(\tau, \mathbf{\Omega}' \to \mathbf{\Omega}) \circ + \int_{4\pi} d\mathbf{\Omega}' \frac{\varpi(\tau)}{4\pi} \frac{\partial P_{11}(\tau, \mathbf{\Omega}' \to \mathbf{\Omega})}{\partial x_k} \circ + \\ & \int_{4\pi} d\mathbf{\Omega}' \delta(\tau - \tau^*) H(\mu) |\mu| \frac{\partial R_s(\mathbf{\Omega}, \mathbf{\Omega}')}{\partial x_k} H(-\mu') |\mu'| \circ \end{aligned} \tag{C35}$$

In terms of Jacobian computations, the adjoint method in Eq.(C34) is usually more efficient that the FD method in Eq.(C25) This is because the adjoint method does not require additional radiative transfer computations for various kinds of perturbations. In adjoint method, all perturbations are transformed into the changes in the source and forward operator. Therefore, once the forward and adjoint radiance fields are known, the Jacobian can be readily obtained from Eq.(C34).

As discussed before, in order to obtain $I^*(\tau,\mathbf{\Omega})$, one needs only to solve the Eq.(C17) with the same model used for forward computations. Less straightforward is the implementation of the inner product, which will be discussed in the rest of this section. In most numerical models, for the sake of numerical efficiency, the scattering phase function (P_{11}) and the surface BDRF (R_s) are usually expanded into Legendre polynomials, in which case Eq.(C35) shall become:

$$\begin{aligned}\frac{\partial L}{\partial x_k} = &-\frac{\partial \tau}{\partial x_k}\circ + \frac{1}{4\pi}\int_{-1}^{1} d\mu' \int_0^{2\pi} d\phi' \left\{ \sum_{m=0}^{2N-1} (2-\delta_{m0}) \cos m(\phi-\phi') \right. \\ &\times \sum_{l=m}^{2N-1} \left[g_l(\tau)\frac{\partial \varpi(\tau)}{\partial x_k} + \varpi(\tau)\frac{\partial g_l(\tau)}{\partial x_k} + \delta(\tau-\tau^*)H(\mu)|\mu|\frac{\partial h_l}{\partial x_k}H(-\mu')|\mu'| \right], \\ &\left. \times (2l+1)\frac{(l-m)!}{(l+m)!}P_l^m(\mu)P_l^m(\mu') \right\}\circ\end{aligned} \tag{C36}$$

where $2N$, corresponding to the length of the series, is the so called “number of stream”; P_l is the Legendre polynomial, P_l^m is the associated Legendre polynomial. g_l and h_l are the expansion coefficients of the scattering phase function and surface BDRF, respectively, given by:

$$g_l(\tau) = \frac{1}{2}\int_{-1}^{1} P_{11}(\tau,\mu_s)P_l(\mu_s)d\mu_s \tag{C37}$$

$$h_l = \frac{1}{2}\int_{-1}^{1} R_s(\mu_s)P_l(\mu_s)d\mu_s \tag{C38}$$

where μ_s is the cosine of scattering (or reflection) angle. Radiance fields are usually divided into two parts, the direct and diffuse radiance:

$$I(\tau,\mathbf{\Omega}') = I^{dif}(\tau,\mathbf{\Omega}') + I^{dir}(\tau,\mathbf{\Omega}'), \tag{C39}$$

$$I^*(\tau,\mathbf{\Omega}) = I^{*,dif}(\tau,\mathbf{\Omega}) + I^{*,dir}(\tau,\mathbf{\Omega}). \tag{C40}$$

It is straightforward to compute the direct radiances, as they follow the Lamber-Beer law. The direct part of the forward and adjoint radiances are given by:

$$I^{dir}(\tau,\mathbf{\Omega}') = F_0 e^{\tau/\mu}\delta(\mu'+\mu_0)\delta(\phi'-\phi_0)\,, \tag{C41}$$

$$I^{*,dir}(\tau,\mathbf{\Omega}) = F_0^* e^{-\tau/\mu}\delta(\mu-\mu_{obs})\delta(\phi-\phi_{obs})\,, \tag{C42}$$

where F_0^* is the strength (i.e., the flux per unit area perpendicular to the direction of the beam) of the adjoint source Q^* if it is an beam source. Furthermore, in numerical models, the diffuse radiance is usually expanded into Fourier series of relative azimuthal angles:

$$I^{dif}(\tau,\mathbf{\Omega}') = \sum_{m=0}^{2N-1} I_m(\tau,\mu')\cos m(\phi'-\phi_0)\,, \tag{C43}$$

$$I^{*,dif}(\tau,\mathbf{\Omega}) = \sum_{m=0}^{2N-1} I_m^*(\tau,\mu)\cos m(\phi-\phi_{obs})\,, \tag{C44}$$

where ϕ_0 and ϕ_{obs} are the azimuthal angle of the sun and satellite, respectively. From the relationship in Eq. (C16), one can easily find:

$$I_m^*(\tau,\mu) = -I'_m(\tau,-\mu)\,, \tag{C45}$$

where I'_m is the coefficients of the Fourier expansion of the diffuse part of the solution to Eq. (C17). By substituting Eqs.(C36), (C39) and (C40) into Eq.(C34) and taking Eqs. (C41), (C42), (C43) and (C44) into account, one can rewrite the inner product, for example the second term in RHS of Eq.(C34), into a numerically-friendly form as follows:

$$\left\langle I^*, \frac{\partial L}{\partial x_k} I \right\rangle = D_\tau + D_{\varpi P_{11}} + D_{surface} \tag{C46}$$

where

$$D_\tau = -\int_0^{\tau^*} d\tau \frac{\partial \tau}{\partial x_k} F_0 e^{-\tau/\mu_0} I^{*,dif}(\tau, -\mu_0, \phi_o) -$$
$$\int_0^{\tau^*} d\tau \frac{\partial \tau}{\partial x_k} F_0^* e^{-\tau/\mu_{obs}} I^{dif}(\tau, \mu_{obs}, \phi_{obs}) - \quad , \tag{C47}$$
$$\int_0^{\tau^*} d\tau \frac{\partial \tau}{\partial x_k} \sum_{m=0}^{2N-1} \frac{2\pi}{2-\delta_{m0}} \cos m(\phi_{obs} - \phi_0) \int_{-1}^{1} d\mu I_m(\tau, \mu) I_m^*(\tau, \mu)$$

and

$$D_{\varpi P_{11}} = \frac{F_0^* F_0}{4\pi} \int_0^{\tau^*} d\tau \frac{\partial \left[\varpi(\tau) P_{11}(\tau, \mathbf{\Omega}_{obs} \to \mathbf{\Omega}_0)\right]}{\partial x_k} e^{-\tau/\mu_{obs}} e^{-\tau/\mu_0} +$$
$$\int_0^{\tau^*} d\tau \sum_{m=0}^{2N-1} \cos m(\phi_{obs} - \phi_0) \sum_{l=m}^{2N-1} k_l^m \frac{\partial \left[\varpi(\tau) g_l(\tau)\right]}{\partial x_k} \left[FD_{\varpi P_{11}}(\tau) + DF_{\varpi P_{11}}(\tau) + FF_{\varpi P_{11}}(\tau) \right] , \tag{C48}$$

and

$$D_{surface} = \frac{F_0^* F_0}{4\pi} e^{-\tau^*/\mu_{obs}} e^{-\tau^*/\mu_0} \mu_{obs} \mu_0 \frac{\partial R_s(\mathbf{\Omega}_{obs} \to \mathbf{\Omega}_0)}{\partial x_x} +$$
$$\sum_{m=0}^{2N-1} \cos m(\phi_{obs} - \phi_0) \sum_{l=m}^{2N-1} k_l^m \frac{\partial h_l(\tau)}{\partial x_k} \left[FD_{surface} + DF_{surface} + FF_{surface} \right] . \tag{C49}$$

In above equations:

$$k_l^m = \frac{(2l+1)}{2} \frac{(l-m)!}{(l+m)!} . \tag{C50}$$

$$FD_{\varpi P_{11}}(\tau) = \int_{-1}^{1} d\mu I_m^*(\tau, \mu) P_l^m(\mu) \times F_0 e^{-\tau/\mu_0} P_l^m(-\mu_0) \tag{C51}$$

$$DF_{\varpi P_{11}}(\tau) = F_0^* e^{-\tau/\mu_{obs}} P_l^m(\mu_{obs}) \times \int_{-1}^{1} d\mu' I_m(\tau, \mu') P_l^m(\mu') \tag{C52}$$

$$FF_{\varpi P_{11}}(\tau) = \int_{-1}^{1} d\mu I_m^*(\tau, \mu) P_l^m(\mu) \times \int_{-1}^{1} d\mu' I_m(\tau, \mu') P_l^m(\mu') \tag{C53}$$

$$FD_{surface} = \int_{-1}^{1} d\mu H(\mu) |\mu| I_m^*(\tau^*, \mu) P_l^m(\mu) \times \mu_0 F_0 e^{-\tau^*/\mu_0} P_l^m(-\mu_0) \tag{C54}$$

$$DF_{surface} = F_0^* e^{-\tau^*/\mu_{obs}} P_l^m(\mu_{obs}) \times \int_{-1}^{1} d\mu H(-\mu') |\mu'| I_m(\tau^*, \mu') P_l^m(\mu') \tag{C55}$$

$$FF_{surface} = \int_{-1}^{1} d\mu H(\mu) |\mu| I_m^*(\tau^*, \mu) P_l^m(\mu) \times \int_{-1}^{1} d\mu' H(-\mu') |\mu'| I_m(\tau^*, \mu') P_l^m(\mu') \tag{C56}$$

VITA

Name: Zhibo Zhang

Address: Department of Atmospheric Sciences
Texas A&M University
3150 TAMU
College Station, TX, 77843-3150

Email Address: zhibo_zhang@tamu.edu

Education: B.S., Atmospheric Sciences, Nanjing University, China, 2001
M.S., Atmospheric Sciences, Texas A&M University, 2004
Ph.D., Atmospheric Sciences, Texas A&M University, 2008